OUKA
The University of Osaka
Institutional Knowledge Archive

Title	Understanding and Control of Single-Photon Emitters at SiO2/SiC Interfaces for Quantum Applications
Author(s)	中沼, 貴澄
Citation	大阪大学, 2026, 博士論文
Version Type	VoR
URL	https://doi.org/10.18910/105428
rights	
Note	

The University of Osaka Institutional Knowledge Archive : OUKA

https://ir.library.osaka-u.ac.jp/

The University of Osaka

Doctoral Dissertation

Understanding and Control of Single-Photon Emitters at SiO_2/SiC Interfaces for Quantum Applications

Takato Nakanuma

January, 2026

Graduate School of Engineering
The University of Osaka

Abstract

Single-photon emitters (SPEs) in silicon carbide (SiC) have attracted considerable attention as building blocks for quantum information technologies and quantum sensing, owing to their compatibility with semiconductor device fabrication processes, and their promising optical properties. In particular, SPEs located at the silicon dioxide (SiO_2)/SiC interface, which is the core of metal-oxide-semiconductor field-effect transistors (MOSFETs), exhibit bright and stable emission even at room temperature and can be formed through low-cost oxidation processes. However, the microscopic origin and controllability of the interface color centers remain poorly understood, hindering their reliable integration into scalable quantum photonic devices.

This dissertation aims to clarify the origin and controllability of SPEs at the SiO_2/SiC interface through a comprehensive study combining optical and electrical characterizations. To this end, systematic oxidation and post-oxidation annealing were performed in pure argon (Ar) or carbon dioxide (CO_2) atmosphere at high temperatures. Confocal photoluminescence (PL) mapping and Hanbury Brown and Twiss (HBT) measurements were employed to evaluate the spatial distribution, density, and single photon characteristics of the color centers, while capacitance-voltage (C–V) analyses were used to examine the densities of electrically active defects at the interface.

The results demonstrated that high-temperature oxidation and subsequent CO_2 annealing effectively suppress the density of both electrically active interface traps and color centers. The color center density could be continuously tuned over two orders of magnitude by adjusting the oxidation and CO_2 annealing temperatures. PL mapping images revealed that CO_2 annealing reduces background luminescence and isolates diffraction-limited bright spots exhibit single-photon characteristics. Electrical measurements showed that the effective fixed-charge density and density of charges that cause C–V hysteresis (N_{Eff} and N_{Hys}, respectively) could be reduced significantly by CO_2 annealing, consistent with the passivation of oxygen vacancies (V_{O}) and the removal of carbon-related interface

defects.

Through quantitative comparison between oxidation, and Ar or CO_2 annealing, this study establishes that CO_2 annealing removes the defects, which act as SPEs, without introducing extrinsic species. The proposed model suggests that interface SPEs originate from carbon-related complexes at the SiO_2/SiC interface and that high-temperature CO_2 annealing effectively suppresses their formation by promoting carbon oxidation and oxygen incorporation through the oxide film.

These findings provide a unified understanding of the correlation between the optical and the structural properties of defects present at the SiO_2/SiC interface, bridging the fields of quantum optics and semiconductor device engineering. The insights gained here pave the way for controllable fabrication of room-temperature SPEs integrated on SiC platforms and lay the foundation for electrically driven, complementary-MOS (CMOS)-compatible quantum light sources suitable for next-generation quantum information and sensing technologies.

Contents

Abstract **i**

1 Introduction **1**

1.1 Quantum Technologies and Applications 1

1.1.1 Quantum Computing 2

1.1.2 Quantum Cryptography and Communication 8

1.1.3 Quantum Sensing and Metrology 9

1.2 General Background of Defect-Based Single Photon Emitters 11

1.2.1 Host Materials for Defect-Based SPEs 19

1.3 Single-Photon Emitters in Silicon Carbide 21

1.3.1 SPEs in Bulk SiC 22

1.3.2 SPEs at SiO_2/SiC Interfaces 26

1.4 Overview of This Dissertation 29

2 Principles of Confocal Laser Scanning Microscope and Measurements **33**

2.1 Introduction 33

2.2 Setup of Confocal Laser Scanning Microscope 34

2.2.1 Confocal PL Mapping 36

2.2.2 PL Spectroscopy 38

2.2.3 HBT Measurements 40

3 Density Control on Color Centers at SiO_2/SiC Interface by Oxidation and Annealing **45**

3.1 Introduction 45

3.2 Experiment 47

3.2.1 Sample Fabrication 47

3.2.2 Experimental Setup of Confocal Laser Scanning Microscopy 48
3.2.3 Analysis of Electrically Active Defects 49
3.3 Density Control of Interface SPEs 52
3.4 Optical Properties of Interface SPEs 54
3.5 Electrical Properties of MOS Capacitors 57
3.6 Correlation Between Optical and Electrical Metrics 60
3.7 Summary 61

4 Design of Annealing Conditions for the Formation of Spatially Separated Single Photon Emitters at SiO_2/SiC Interfaces 63
4.1 Introduction 63
4.2 Experiments 64
4.2.1 Flow of Sample Preparation and Measurements 64
4.2.2 Experimental Setup of Confocal Laser Scanning Microscopy 65
4.3 Confocal Mapping Images of Interface SPEs 66
4.4 Electrical Characteristics of MOS Capacitors 68
4.5 Correlation Between Color Centers and Electrically Active Defects 70
4.6 Relationship Between SPE Ratio and Background luminescence 72
4.7 Summary 74

5 Discussions 77
5.1 Mechanisms of Defect Reduction 77
5.2 Strategy for Reliable Formation of Interface SPEs 79
5.3 Discrepancy Between Electrical Charge and Color Center Densities 80
5.4 Possible Origin of Interface SPEs 83

6 Conclusion 85
6.1 Summary of This Dissertation 85
6.2 Future Prospects 87

References 89

Acknowledgements 99

List of Publications 101

Chapter 1

Introduction

1.1 Quantum Technologies and Applications

Since the advent of modern electronics, advances in semiconductor technology have dramatically improved the standard of living. However, as device miniaturization approaches its physical limits, the development of alternative device principles beyond conventional electronics has become increasingly important. Among these emerging paradigms, quantum devices based on the principles of quantum mechanics have attracted significant attention for their potential applications in computing, secure communication, sensing, and simulation.

In particular, the demand for quantum computers has been rapidly increasing. According to Quantum Economic Development Consortium (QED-C)'s 2025 State of the Global Quantum Industry Report, the global quantum-technology market is projected to reach approximately USD 1.88 billion in 2025, representing a nearly 27% year-on-year increase [1]. In parallel with this industrial momentum, research milestones and news releases have demonstrated quantum supremacy, most notably [2]. On the other hand, the realization of quantum computing also poses potential threats to conventional cryptographic systems. For instance, it has been suggested that quantum algorithms could efficiently decrypt Rivest-Shamir-Adleman (RSA) encryption, which is widely used in current secure communication. However, it is estimated that approximately one million quantum bits (qubits) would be required to factorize standard 2048-bit RSA encryption within a practical time frame [3]. Considering that today's leading platforms, such as superconducting quantum processors, provide only on the order of 100–1000 qubits, this

goal remains far beyond current hardware capabilities. Moreover, the quality of qubits, such as coherence time, gate fidelity, and readout accuracy, is also crucial for practical implementation.

Nevertheless, intensive research has been conducted to explore practical computations even with noisy intermediate-scale quantum (NISQ) devices. At the same time, other quantum technologies are also gaining importance alongside quantum computing, such as quantum key distribution (QKD) for theoretically unbreakable communication [4], quantum sensing for ultrahigh sensitivity and spatial resolution [5], and quantum simulation for solving intractable physical systems [6].

All these quantum applications exploit unique quantum-mechanical phenomena or properties, namely the manipulation of quantum states. The choice of physical systems in which these quantum states are formed and controlled is of fundamental importance. Indeed, various platforms have been reported to realize quantum states, each with its own strengths and limitations depending on the target application. In the following sections, representative quantum technologies—quantum computing, quantum cryptography, and quantum sensing—are introduced to provide an overview of their principles, current progress, and challenges.

1.1.1 Quantum Computing

Since the invention of the MOSFET, the computational power of *von Neumann-type computers* has steadily improved with device miniaturization. However, as device dimensions approach the regime where quantum mechanical effects become dominant, further scaling no longer follows a straightforward path. Researchers have tackled these challenges not only by exploring new semiconductor and gate-oxide materials, but also by introducing novel device architectures, such as gate-all-around (GAA) or nanosheet structures.

Amid these developments, an alternative paradigm—quantum computing—has attracted increasing attention as a fundamentally new approach to computation that departs from conventional electronics-based design. Classical computers process information in binary form (0 or 1) using logic gates such as NAND gate. In contrast, quantum computing replaces the classical bit with a qubit, which can exist in a superposition of $|0\rangle$ and $|1\rangle$ states, as depicted in Fig. 1.1. Quantum gate operations manipulate these superposed states according to the principles of quantum mechanics [7].

In quantum computing, single-qubit gates manipulate the state of a qubit through

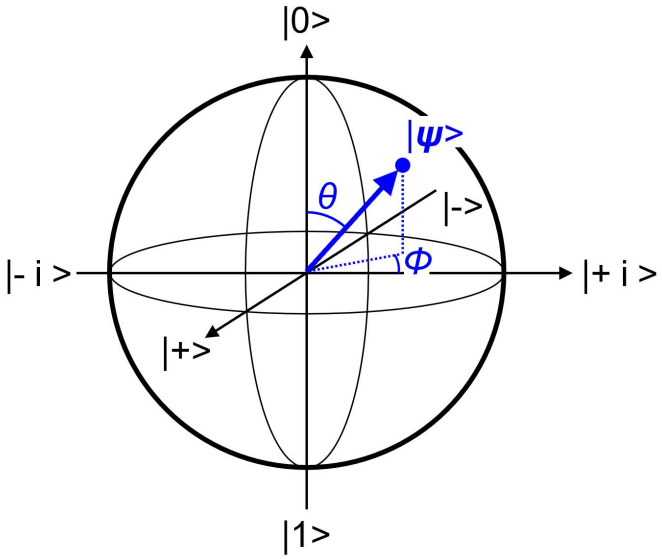

$$|\psi\rangle = e^{i\delta}\left(\cos\frac{\theta}{2}|0\rangle + \sin\frac{\theta}{2}e^{i\phi}|1\rangle\right)$$

Figure 1.1. Illustration of a quantum state of single-qubit.

unitary rotations on the Bloch sphere. As shown in Fig. 1.2 (a), the Pauli X-gate corresponds to a π rotation about the x axis of the Bloch sphere, which transforms $|0\rangle$ into $|1\rangle$ and $|1\rangle$ into $|0\rangle$, realizing a bit-flip operation. In addition, the Hadamard (H) gate creates a balanced superposition state from an initialized basis state, as illustrated in Fig. 1.2 (b). These elementary operations allow full control over arbitrary single-qubit states through sequences of rotations. When extending to multi-qubit systems, quantum gate operations can generate correlations that have no classical analogue. A representative example is the controlled-NOT (CNOT) gate, which flips the target qubit conditional on the state of the control qubit. This conditional action correlates the Bloch-sphere trajectories of the individual qubits, as depicted in Fig. 1.2 (c), and produces quantum entanglement when applied to superposed states. Such entangling gates constitute the essential building blocks for multi-qubit quantum logic. By combining single-qubit rotations with entangling two-qubit gates, one can implement any unitary operation on a quantum register. In contrast to classical computation—where a single gate, such as NAND, is universal—quantum computation does not possess a single universal gate. Instead, universality arises from a finite universal gate set, typically comprising all single-qubit rotations together with an entangling gate such as CNOT. Algorithms constructed from such gates, including Shor's prime-factorization algorithm and Grover's search algorithm, highlight the computational

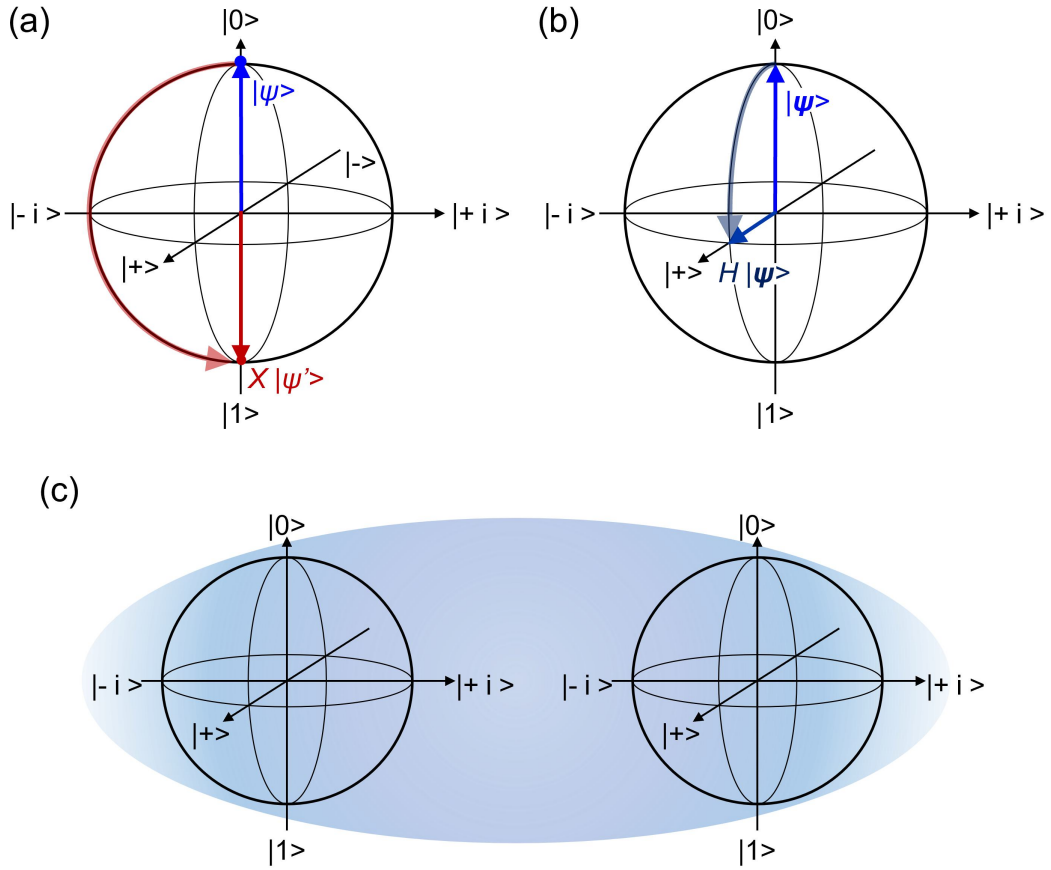

Figure 1.2. (a) Action of the Pauli X-gate on a general qubit $|\psi\rangle$ shown on the Bloch sphere. (b) Action of H gate on $|\psi\rangle$. (c) Two-qubit controlled operations couple the states of individual qubits and can generate quantum entanglement when acting on superposition states.

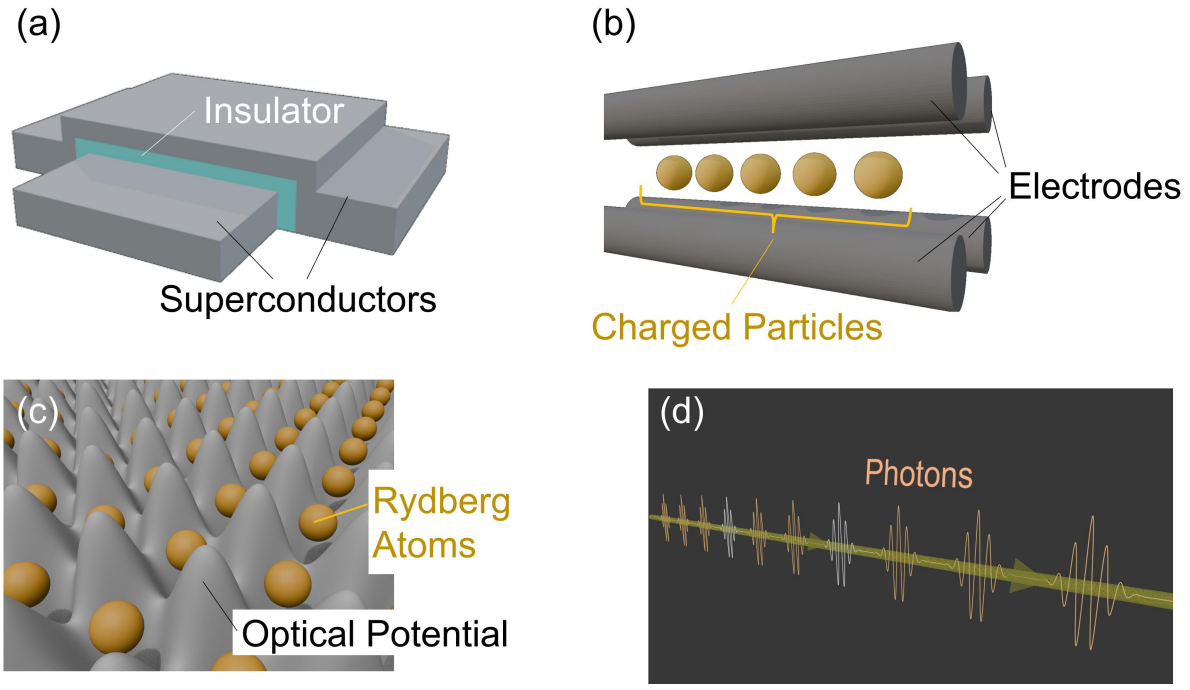

Figure 1.3. Illustration of representative quantum computing platforms, including (a) superconducting quantum processors, (b) ion traps, (c) cold-atom systems, and (d) photonic systems.

advantages that motivate the development of large-scale quantum processors [7].

While these gate operations define the abstract model of quantum computation, their physical realization has been demonstrated across a variety of experimental platforms. Each system exhibits distinct strengths and limitations, leading to different technological strategies for implementing high-fidelity quantum control. Representative examples of such hardware platforms are illustrated in Fig. 1.3.

Superconducting quantum processors, as shown in Fig. 1.3 (a), utilize Josephson junctions to form anharmonic energy levels corresponding to a cosine-like potential. The two lowest eigenstates are used as the qubit basis $|0\rangle$ and $|1\rangle$. Recent advances have positioned superconducting circuits among the most rapidly developing quantum computing platforms, and their progress was recognized by the 2025 Nobel Prize in Physics. Experimental implementations have also demonstrated quantum advantage [2]. Single-qubit gates are realized by applying resonant microwave (MW) pulses that coherently drive Bloch-sphere rotations, routinely achieving fidelities exceeding 99.9% in state-of-the-art transmon devices [8, 9]. Two-qubit entangling gates are implemented either through tunable couplers or through cross-resonance interactions operating via shared circuit modes,

and recent experiments have reported fidelities of 99.6–99.7% [10]. A major practical limitation is that superconducting circuits must be cooled to approximately 4 mK in order to suppress thermal decoherence.

Trapped-ion systems, illustrated in Fig. 1.3 (b), confine charged atomic ions in electromagnetic potentials, with qubits encoded in hyperfine or electronic states that can exhibit coherence times longer than 10 minutes under optimized conditions [11]. Single-qubit gates are driven by tightly focused laser beams or global Raman transitions, achieving fidelities exceeding 99.999% [12]. Entangling gates are implemented using collective motional modes, representing quantized vibrations of the ion chain that couple the internal spin states through shared motion. These interactions support deterministic two-qubit gates, and fidelities approaching 99.9% have been reported using Mølmer–Sørensen and geometric-phase operations [13]. However, these systems require ultra-high vacuum conditions, typically below 1×10^{-11} Torr (at the nanopascal level), to maintain stable confinement and suppress collisions [11].

Cold-atom platforms, depicted in Fig. 1.3 (c), trap neutral atoms (such as rubidium) in optical lattices or optical tweezers. Qubits are encoded in hyperfine ground states, enabling coherence times ranging from several seconds to several minutes depending on the trapping environment and magnetic shielding [6]. Single-qubit gates are driven using MW or Raman transitions and routinely achieve fidelities above 99.5% [14]. Strong, tunable interactions arise when atoms are excited to Rydberg states, supporting fast entangling gates with fidelities approaching 99% in scalable atomic arrays [15]. As a result, Rydberg-atom arrays are widely regarded as promising architectures for programmable quantum processors.

Photonic computing, as illustrated in Fig. 1.3 (d), is also promising. Photons offer appealing advantages such as ultrafast propagation, robustness against environmental noise, room-temperature operation, and compatibility with existing optical communication technologies. Several methods for encoding quantum information in photonic states have been developed, and representative implementations based on single-photon protocols are illustrated in Fig. 1.4. Quantum information can be encoded either in continuous variables [16] or in discrete photonic qubits [17], and hybrid architectures that combine these modalities have also been demonstrated [16, 18].

Discrete photonic qubits commonly utilize polarization, path, time-bin, or orbital angular momentum degrees of freedom. In polarization encoding, as shown in Fig. 1.4 (a),

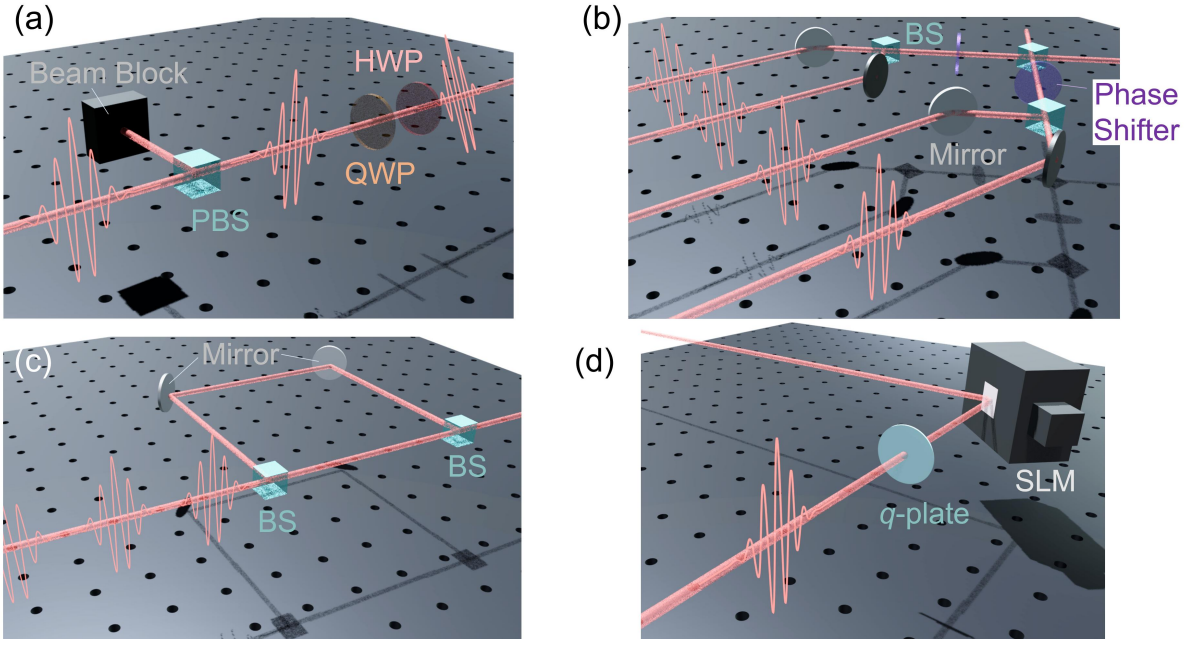

Figure 1.4. Representative encoding methods for photonic quantum information. (a) Polarization, (b) path, (c) time-bin, and (d) orbital angular momentum encodings. In this figure, BS, PBS, QWP, HWP, and SLM denote beam splitter, polarizing beam splitter, quarter-wave plate, half-wave plate, and spatial light modulator, respectively.

the horizontal and vertical polarization states define the qubit basis. Wave plates and polarizing beam splitters enable arbitrary single-qubit rotations and projective measurements. Path encoding, as illustrated in Fig. 1.4 (b), represents logical states by routing photons into spatially separated optical paths. Beam splitters and mirrors manipulate the relative amplitudes and phases of the optical fields, which allows the implementation of unitary gate operations. Time-bin encoding, as shown in Fig. 1.4 (c), uses early and late temporal modes generated by unbalanced interferometers. This approach exhibits enhanced robustness in fiber-based systems because the two time bins experience similar phase noise. Orbital angular momentum encoding, as illustrated in Fig. 1.4 (d), exploits helical phase structures of light. Devices, such as q-plates, convert between spin and orbital angular momentum states and enable access to high-dimensional Hilbert spaces through orthogonal angular momentum modes.

Single-qubit operations in these encoding schemes are realized using linear optical components, including wave plates, beam splitters, phase shifters, and mode converters. Photonic entanglement is typically generated probabilistically through multi-photon interference and post-selection, which require high indistinguishability among photons

produced by independent sources.

1.1.2 Quantum Cryptography and Communication

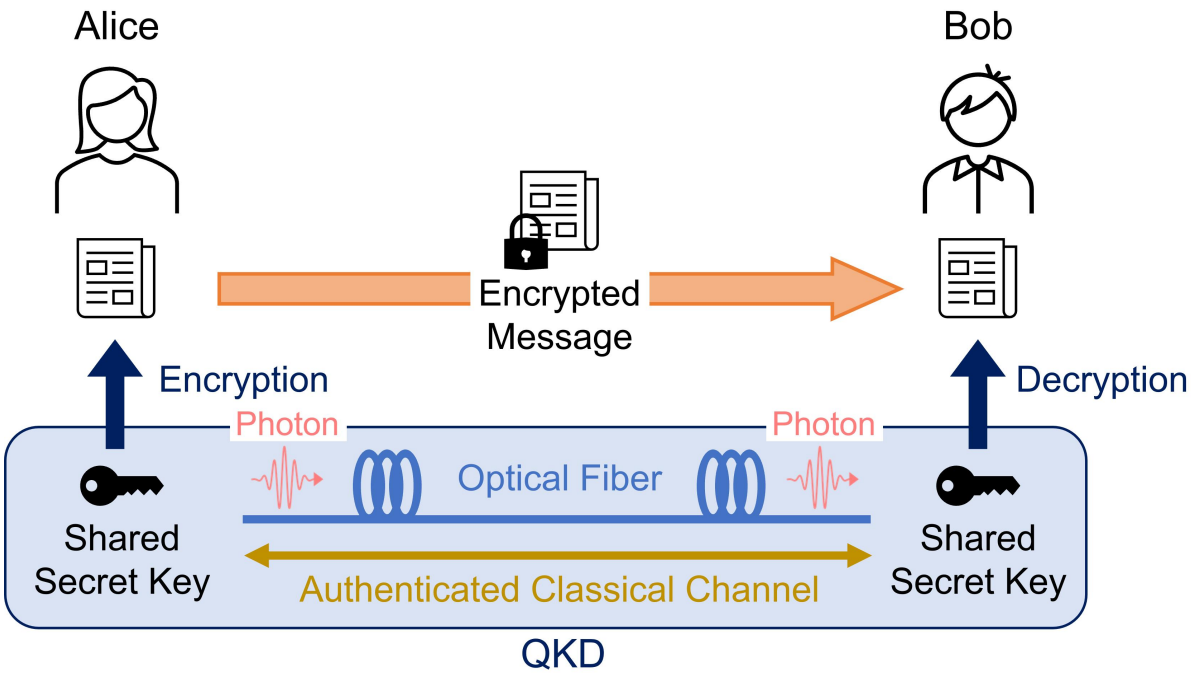

Figure 1.5. A schematic of typical QKD process between Alice and Bob.

Quantum cryptography enables theoretically unbreakable secure communication by combining classical symmetric-key encryption with QKD [7, 19]. A schematic of QKD is illustrated in Fig. 1.5. In this framework, communication begins by using QKD to establish a shared secret key between the sender (Alice) and the receiver (Bob), as shown in the lower panel of the figure. The shared secret key is generated based on quantum randomness. QKD transmits information using the quantum states of single photons and ensures confidentiality through fundamental quantum mechanical principles—namely, that the number of photons cannot be arbitrarily increased or decreased, and that any measurement on part of a quantum state irreversibly disturbs the information it carries. An authenticated classical channel is used in parallel to reconcile the key and to guarantee its integrity.

Once the shared secret key has been generated via QKD, it is employed for classical symmetric-key encryption and decryption, as depicted in the upper panel of Fig. 1.5. Because symmetric-key encryption is theoretically impossible to break without the secret

key, combining it with a QKD-generated key enables a communication channel that is, in principle, immune to eavesdropping.

Among the various QKD schemes, the most representative is the BB84 protocol [20]. This protocol encodes information in non-orthogonal polarization bases of single photons. The use of non-orthogonal states ensures unconditional security against any measurement attempt by an eavesdropper [4]. However, optical signals attenuate with distance, and therefore long-distance quantum communication requires quantum repeaters. Realizing such repeaters necessitates the generation and preservation of quantum entanglement, which remains a major technological challenge.

1.1.3 Quantum Sensing and Metrology

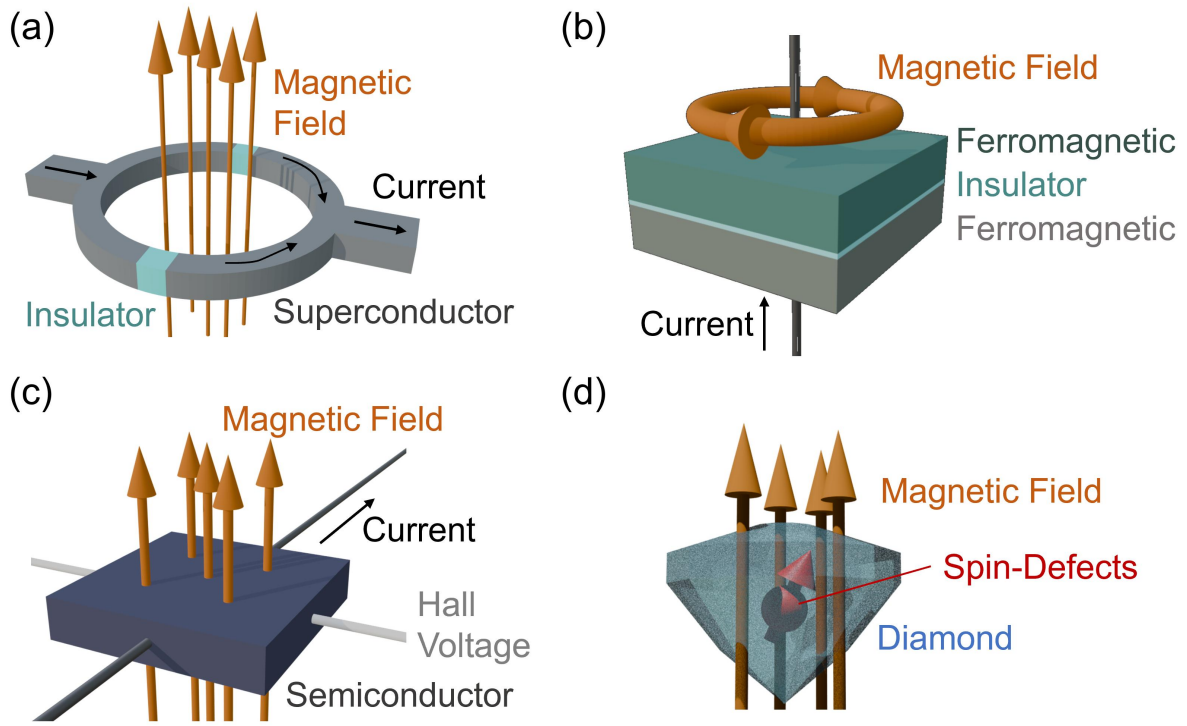

Figure 1.6. Representative systems which are promising as magnetic sensing applications, indicating (a) SQUID, (b) TMR, (c) Hall-effect sensor, and (d) Spin-defect.

For practical sensing applications, solid-state sensors are particularly attractive due to their compactness, robustness, and ease of integration. The demands for sensing span a wide range of physical quantities, including electric fields, magnetic fields, temperature, and pressure. Consequently, various sensing schemes have been developed using different

physical platforms. Representative examples of magnetic sensing are shown in Fig. 1.6, including high-sensitivity magnetic sensors such as superconducting quantum interference devices (SQUIDs), tunneling magnetoresistance (TMR) sensors, Hall-effect sensors, and spin-defect-based sensors [5, 21].

SQUID sensors, illustrated in Fig. 1.6 (a), operate by detecting magnetic-flux-dependent phase shifts in superconducting loops. Although they offer extremely high sensitivity, reaching values below 1 fT/$\sqrt{\text{Hz}}$, they require cryogenic operation to maintain superconductivity, are limited to a single detection axis, and typically exhibit limited spatial resolution due to the size of their pickup coils [22].

TMR sensors (Fig. 1.6 (b)) exploit spin-dependent tunneling through magnetic multilayers. They provide room-temperature operation, compact integration, and sub-nanotesla sensitivity, making them suitable for portable or on-chip devices, although their spatial resolution is limited to several hundred micrometers and they are restricted to a single detection axis [23].

Hall-effect sensors (Fig. 1.6 (c)) measure magnetic fields through the Lorentz-force-induced Hall voltage in semiconductors. They operate over a wide temperature range and are easy to fabricate, offering micrometer-scale spatial resolution, though their sensitivity is typically lower than that of SQUIDs or TMR sensors [24].

Spin defects (Fig. 1.6 (d)), such as nitrogen-vacancy (NV) centers in diamond, are a class of point defects in solids whose electron spins are optically or electrically addressable and show shifts in the spin transition frequency in response to magnetic fields [5, 25]. These sensors operate at room temperature and provide nanoscale spatial resolution due to their angstrom-scale size. In addition, their sensitivities can be tuned by varying the defect density, ranging from tens of nT/$\sqrt{\text{Hz}}$ for single NV centers [26–28] to sub-pT/$\sqrt{\text{Hz}}$ for ensemble configurations [29–31].

The localized electron spin associated with an NV center can detect variations in external perturbations, such as magnetic and electric fields as well as temperature, through its spin-resonance response. Moreover, NV centers can also serve as SPEs.

1.2 General Background of Defect-Based Single Photon Emitters

As mentioned above, various physical platforms have been explored as quantum systems. Among these, photonic quantum systems play a central role because photons serve as robust information carriers. They propagate at the speed of light, exhibit weak coupling to the environment even at room temperature and under ambient conditions, and are naturally compatible with existing optical communication infrastructure. This section focuses on SPEs based on point defects in semiconductors, which represent a key class of photonic quantum systems. This overview provides the context and motivation for developing solid-state SPEs that can be integrated into semiconductor platforms.

The realization of photonic quantum technologies requires stable and efficient SPEs. SPEs produce exactly one photon per excitation cycle, which is essential for quantum communication, computation, and sensing. The earliest demonstration of single photon emission was achieved using sodium (Na) atoms [32]. More recently, semiconductor quantum dots have been extensively studied as solid-state SPEs [33, 34]. However, these systems generally require cryogenic operation, mitigation of fluorescence blinking, and complex microfabrication processes, which limit their scalability, and practical implementation.

In wide-bandgap (WBG) semiconductors, such point defects form localized electronic states inside the bandgap, giving rise to well-defined ground-state (GS) and excited-state (ES) manifolds, as illustrated in Fig. 1.7. Upon optical excitation from the GS to the ES, the defect relaxes radiatively and emits a single photon per excitation cycle. This closed optical cycle underlies the deterministic generation of single photons. When the defect hosts an electronic spin, the GS and ES manifolds split under external magnetic or electric fields. These Zeeman- or Stark-induced splittings differ between the GS and ES, resulting in spin-dependent optical transition energies. Because optical transitions follow spin-conserving selection rules, the relaxation pathway preserves the spin state, and the emitted fluorescence exhibits a slight spin-dependent spectral shift, as schematically shown in Fig. 1.7. Consequently, the emission encodes information about the spin state, enabling these defects to function as spin-photon interfaces.

A prototypical and leading example is the NV center in diamond [35]. The NV center, known as a color center responsible for red luminescence in diamond [36], was the first

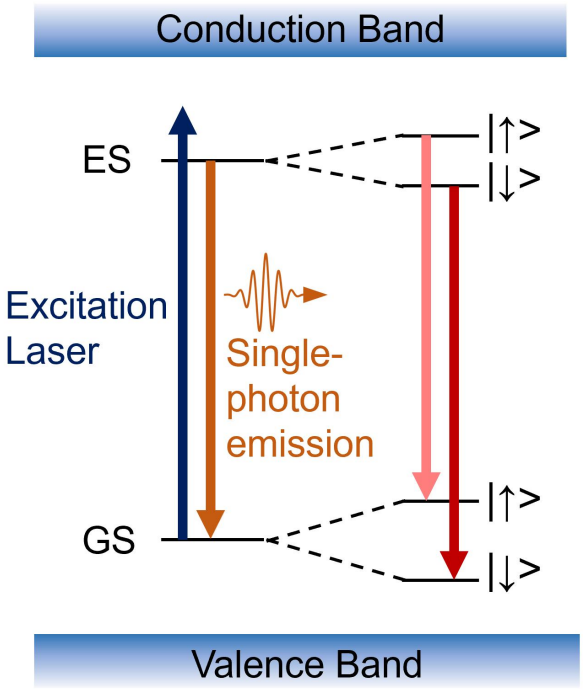

Figure 1.7. Schematic energy-level diagram of a color center. An excitation laser promotes the system from the GS to ES, followed by radiative relaxation that generates single-photon emission. In the presence of an external field, the degeneracy of the ground and excited states is lifted, causing the spin sublevels to split as indicated by the dashed lines.

defect whose single electron spin was observed via optically detected magnetic resonance (ODMR) by Gruber *et al.* [35]. A few years later, coherent spin manipulation in a single NV center was demonstrated [37, 38], paving the way for its use as a solid-state spin qubit. Moreover, highly sensitive magnetic sensing using NV centers was theoretically proposed [39, 40] and experimentally realized [41, 42], leading to applications in quantum metrology. Owing to these properties, NV centers have enabled diverse demonstrations, such as quantum entanglement between remote nodes [43, 44], high sensitive magnetometer [27], and bio-magnetic sensing [45].

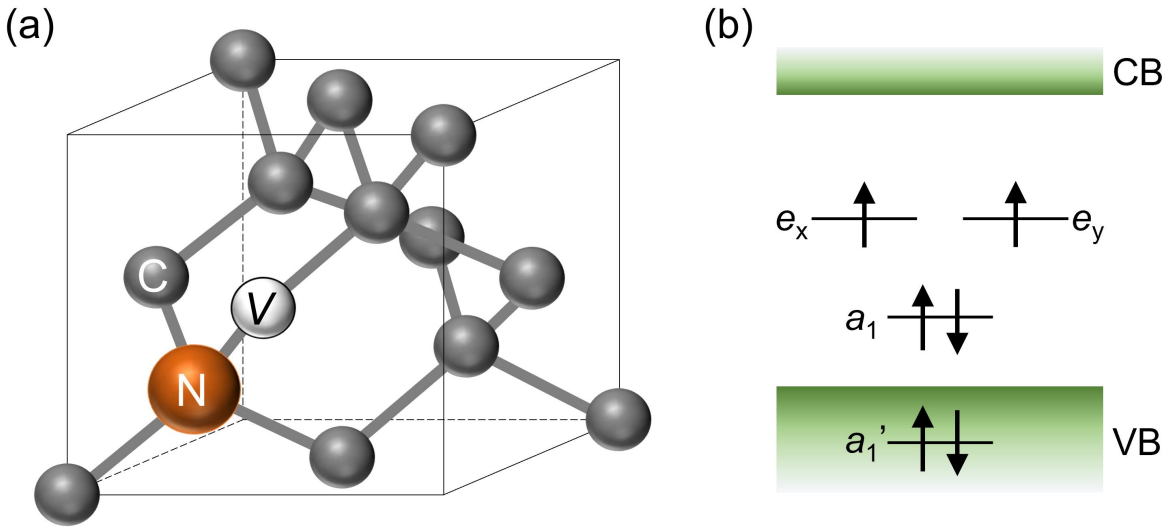

Figure 1.8. (a) Illustration of NV center in diamond. (b) A schematic energy level structure of GS of the NV center without extrinsic fields [46].

The negatively charged NV center in diamond consists of a substitutional nitrogen atom adjacent to a carbon vacancy, as illustrated in Fig. 1.8 (a). A total of six electrons are localized around the defect: three originating from the nearest-neighbor carbon atoms surrounding the vacancy, two from the nitrogen atom, and one additional electron. The three carbon atoms and the nitrogen contribute four sp^3-hybridized dangling bonds, which combine to form four defect orbitals that transform according to the C_{3v} symmetry of the NV center. These symmetry-adapted orbitals of the GS are conventionally labeled a_1, a_1', and e_x, e_y, as illustrated in Fig. 1.8 (b). The six electrons occupy these levels according to Hund's rules, yielding the electronic configuration in which the two electrons in the doubly degenerate e orbitals align their spins. This results in a spin-triplet GS with total spin $S = 1$ and symmetry term $^3A_2$. Although the $^3A_2$ GS is subject to a dynamic Jahn-Teller effect, its orbital non-degeneracy ensures that the spin-triplet structure remains

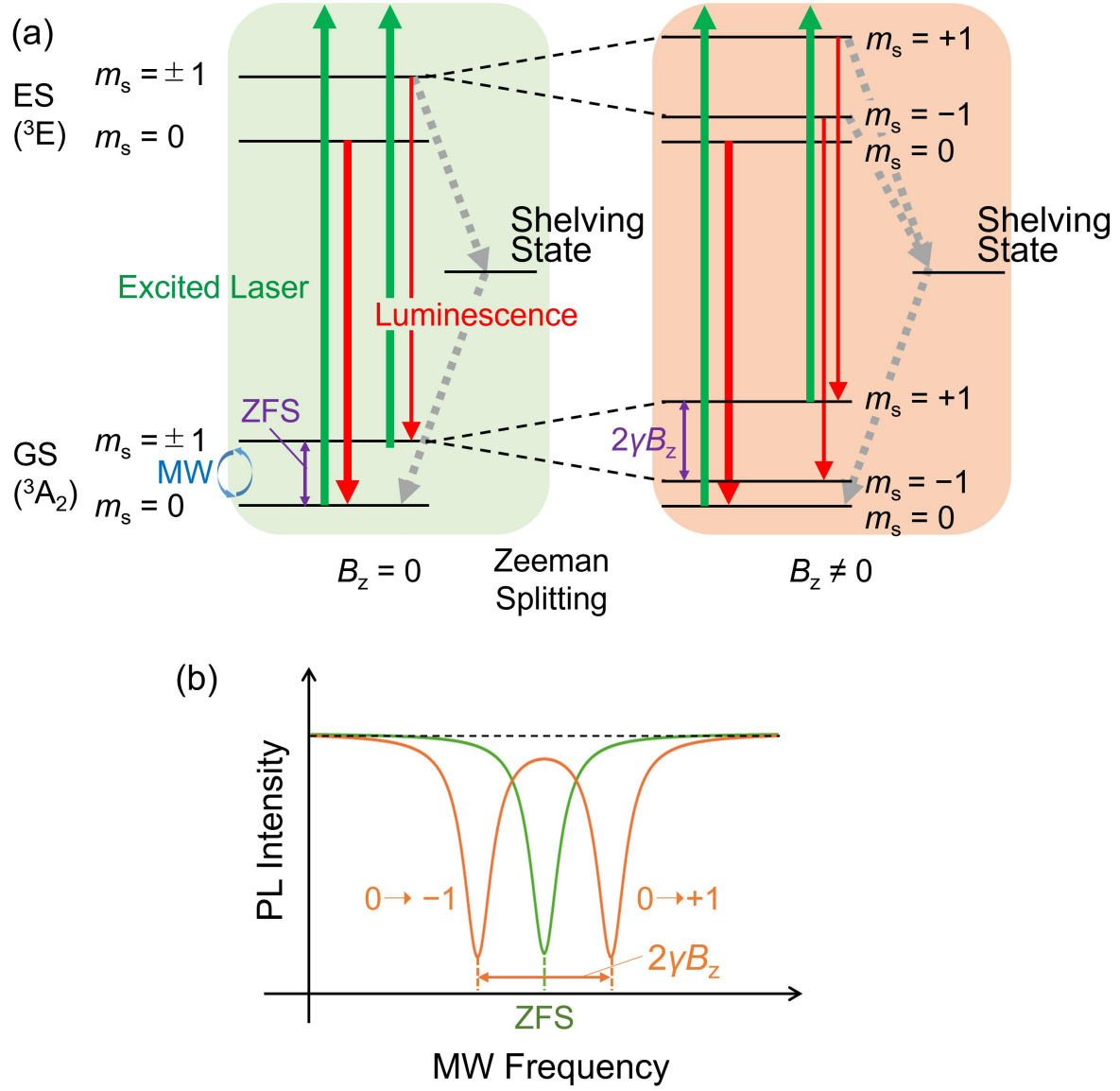

Figure 1.9. (a) Energy-level structure of the NV center illustrating the GS and ES spin triplets, optical excitation, spin-dependent ISC pathways, and the effect of an external magnetic field B_z that lifts the degeneracy between the $m_s = \pm 1$ sublevels. (b) Corresponding ODMR spectra showing a single resonance dip at the ZFS when $B_z = 0$, and two Zeeman-split resonances separated by $2\gamma_e B_z$ under a finite magnetic field.

well defined, and the state is widely treated as an isolated single-spin system in the solid state [47–49].

The resulting GS spin triplet is composed of the three sublevels $m_s = 0$ and $m_s = \pm 1$, as shown in Fig. 1.9 (a). In the absence of external fields, the $m_s = \pm 1$ states are degenerate, while the $m_s = 0$ level is separated from them by the GS zero-field

splitting (ZFS) of $D \approx 2.87$ GHz [25, 35], which originates from spin–spin interactions within the triplet manifold. When the defect is excited with a laser whose photon energy exceeds the GS–ES energy gap (typically a green laser at 532 nm), the NV center emits single-photon, with the zero-phonon line (ZPL) appearing at approximately 637 nm. A distinctive feature of the NV center is that the PL intensity depends on its spin state. For the $m_s = \pm 1$ sublevels, relaxation from the ES partly proceeds through a non-radiative intersystem-crossing (ISC) pathway into a shelving state, as indicated in Fig. 1.9 (a). The ISC process preferentially returns population to the $m_s = 0$ GS sublevel. Consequently, under continuous optical excitation, the spin population is pumped into $m_s = 0$, enabling efficient optical spin initialization without requiring resonant excitation, which would otherwise be necessary in a conventional two-level system. Furthermore, MW radiation that is resonant with the energy splittings between the $m_s = 0$ and $m_s = \pm 1$ levels redistributes the spin population and modulates the PL intensity. As shown in Fig. 1.9 (b), sweeping the MW frequency while monitoring the PL results in a dip in fluorescence whenever the MW frequency matches the transition energy between the spin sublevels. At zero magnetic field, this occurs at the ZFS frequency D, providing a direct measurement of the ground-state splitting. When an external magnetic field B_z is applied along the NV axis, the Zeeman interaction lifts the degeneracy between the $m_s = +1$ and $m_s = -1$ states, as shown in Fig. 1.9 (b). The corresponding transition frequencies shift to $D \pm \gamma_e B_z$, resulting in a splitting of $2\gamma_e B_z$ between the two MW resonances. By recording the PL while sweeping the MW frequency, one can directly extract this splitting and thereby determine the magnitude of the applied magnetic field. This technique, known as ODMR, forms the basis of NV center sensing.

The most basic sensing protocol is the measurement of Rabi oscillations [25, 50]. As depicted in Fig. 1.10 (a), when a resonant MW field is applied to the NV center, the spin vector undergoes a coherent rotation on the Bloch sphere around an axis in the equatorial plane. In this Bloch-sphere representation, the two GS spin sublevels that participate in the MW transition form an effective two-level system: the $m_s = 0$ state in Fig. 1.9 (a) is identified with the Bloch-sphere basis state $|0\rangle$, and either of the $m_s = \pm 1$ states serves as the corresponding $|1\rangle$. Thus, the MW-driven transition between $m_s = 0$ and $m_s = \pm 1$ can be visualized as coherent rotations between $|0\rangle$ and $|1\rangle$ on the Bloch sphere. Thus, the MW-driven transition between $m_s = 0$ and $m_s = \pm 1$ is visualized as a rotation of the spin vector between these two poles. Experimentally, this rotation is

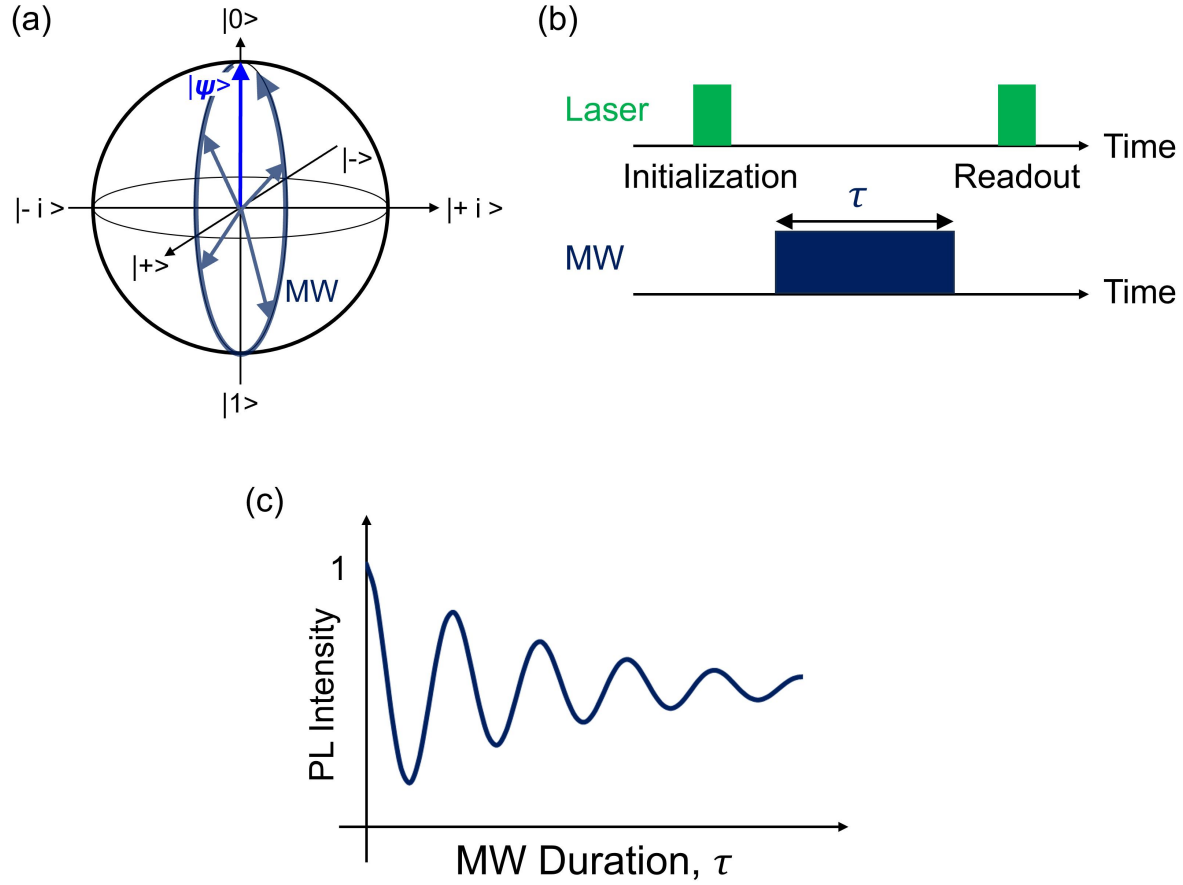

Figure 1.10. (a) Bloch-sphere representation of a driven two-level system. A resonant MW field induces coherent rotations of the qubit state around a transverse axis, leading to periodic population transfer between $|0\rangle$ and $|1\rangle$. (b) Pulse sequence used to measure Rabi oscillations. A laser pulse initializes the spin state, a MW pulse of duration τ drives coherent rotation, and a second laser pulse reads out the resulting state. (c) Typical Rabi oscillation signal. The detected PL intensity oscillates as a function of the MW pulse duration τ, reflecting sinusoidal population transfer and gradual dephasing.

driven by applying a square MW pulse whose duration (τ) is varied, as shown in the pulse sequence in Fig. 1.10 (b). By repeatedly initializing the spin with a laser pulse, applying an MW pulse of variable duration, and then reading out the PL, one observes a periodic oscillation in the PL intensity, as shown in Fig. 1.10 (c). These oscillations reflect the coherent exchange of population between the $m_s = 0$ and $m_s = \pm 1$ spin sublevels during the MW-driven rotation, where a π-pulse corresponds to full population inversion and shorter durations correspond to fractional Bloch-sphere rotations.

The oscillation amplitude gradually decays as the MW pulse duration increases, indi-

cating the loss of spin coherence. This decay arises from environmental noise sources such as magnetic fluctuations from surrounding nuclear spins, strain- and electric-field noise, and interactions with nearby paramagnetic defects. Because these noise processes degrade the phase information stored in the spin state, long coherence times (T_2) are essential for applications requiring deep quantum computing circuit depth or high-precision sensing. In high-purity diamond, millisecond-scale coherence times have been demonstrated using spin-echo and dynamical-decoupling techniques, enabling high-fidelity coherent control of the NV electronic spin [27, 51]. Such long T_2 times arise because point defect-based SPEs constitute atomically localized and highly isolated quantum systems that are inherently robust against many forms of environmental noise. Here, coherent control refers to the ability to drive deterministic rotations on the Bloch sphere while preserving the relative spin phase.

In addition to optical detection, photoelectric readout schemes such as photocurrent-detected magnetic resonance (PDMR) have recently been demonstrated [52, 53]. Here, the spin-dependent ionization dynamics of the NV center are converted into an electrical signal, enabling MW-resonance detection without PL collection. Because the spatial resolution is set by lithographically defined electrodes and only simple optical excitation is required, PDMR offers a device-compatible and scalable alternative to optical ODMR.

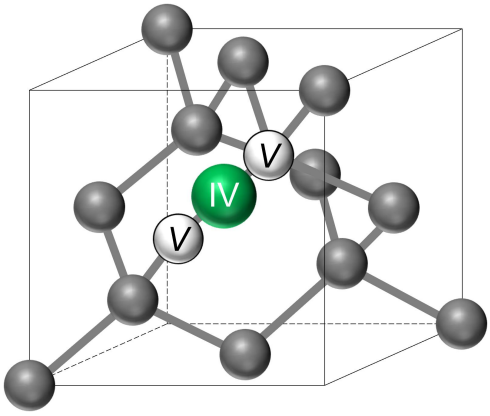

Figure 1.11. Illustration of group-IV defects in diamond, which consists of an interstitial group-IV atoms (Si, Ge, Sn) adjacent to two carbon vacancies.

Despite these advantages, the NV center is not universally suitable for all quantum applications. Its Debye-Waller (DW) factor—the fraction of ZPL emission relative to total photoluminescence—is only about 3% [60], resulting in poor photon indistinguishability and making entanglement generation challenging. To overcome this, two main approaches

Table 1.1. Properties of group-IV color centers and NV center in diamond [35, 54–59].

Defects	Wavelength	Spin (S)	DW Factor
NV^-	637 nm	1	∼3%
SiV^-	738 nm	1/2	∼70%
SiV^0	946 nm	1	∼90%
GeV^-	602 nm	1/2	∼70%
SnV^-	619 nm	1/2	∼40%

have been developed. One is exploring alternative defect systems, particularly group-IV-related color centers in diamond, which exhibit higher DW factors. The structures of these defects are illustrated in Fig. 1.11, and their properties are summarized in Table 1.1.

Focusing on the silicon-vacancy (SiV) center as a representative example, it exhibits high geometrical symmetry (D_{3d}) and a large DW factor of about 70%, as predicted by density functional theory (DFT) calculations [55]. However, the small ground-state splitting ($\Delta_{GS} \approx 50$ GHz) of the SiV^- center results in significant coupling to thermal acoustic phonons, thereby limiting its spin coherence time to about 100 ns even at 4 K [54, 61]. This coherence can be extended to 13 ms at 100 mK [62]. To improve thermal robustness, heavier group-IV atoms, such as germanium (Ge), and tin (Sn) have been introduced, increasing Δ_{GS} due to stronger spin-orbit coupling [57, 59, 63, 64]. These results demonstrate that even within the same host material, different defect species exhibit distinct optical and spin characteristics.

Another approach to improving the DW factor is to embed NV centers into photonic cavities, which enhance light-matter interaction through the Purcell effect [60, 65]. As noted above, the PL intensity of the NV center is relatively weak, mainly due to its long excited-state lifetime of about 12 ns, leading to slow optical cycling [66]. This limits the applicability of NV centers in applications that require high photon emission rates. Several approaches have been explored to enhance the emission rate of NV centers. One strategy is to integrate NV centers into nanoscale photonic cavities, such as photonic crystal (PhC) nanocavities, as shown in Fig. 1.12. This integration enhances the radiative decay rate through the Purcell effect [60, 65]. Owing to their atomic dimensions and strong wavefunction confinement, defect-based SPEs offer excellent photostability and can

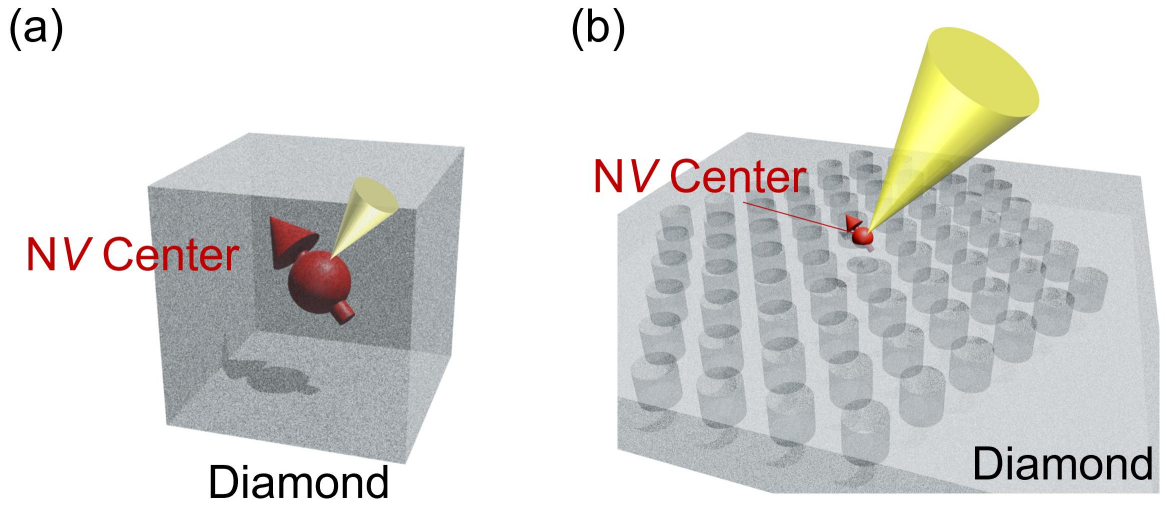

Figure 1.12. Schematics of photoluminescence from an NV center in (a) a bulk diamond crystal and (b) a PhC diamond structure, where the PhC cavity enhances the emission rate via improved light confinement.

operate even at room temperature, exhibiting intrinsic robustness against environmental perturbations. Furthermore, such color centers can, in principle, be formed directly within semiconductor device structures, enabling monolithic integration of quantum light sources with electronic and photonic circuits [60, 65].

1.2.1 Host Materials for Defect-Based SPEs

Benchmark of representative WBG semiconductors—4H-SiC, diamond, and gallium nitride (GaN)—with silicon (Si) included as a baseline reference are summarized in Table 1.2. These materials differ significantly in their electronic, thermal, and optical properties, which collectively influence their suitability as host crystals for defect-based SPEs.

Focusing on the bandgap, 4H-SiC, diamond, and GaN possess much wider bandgaps (3.26–5.47 eV) than Si (1.12 eV). The wide bandgap allows the formation of energetically well-isolated defect states with tunable energy levels across the bandgap, thereby enabling optical transitions over a wide spectral range. Thermal conductivity is another critical parameter: diamond exhibits an exceptionally high value ($\sim$ 20 W cm^{-1} K^{-1}), followed by SiC ($\sim$ 4.9 W cm^{-1} K^{-1}), both far exceeding that of Si ($\sim$ 1.5 W cm^{-1} K^{-1}). Efficient heat dissipation is advantageous for high-power optical excitation and for integration with on-chip photonic or electronic elements.

The dielectric constant and refractive index also play important roles in photon extraction and optical design. The refractive indices of SiC ($n \approx 2.7$) and diamond ($n \approx 2.4$) at visible wavelengths are significantly lower than that of Si ($n \approx 4.2$). A lower refractive index reduces total internal reflection and increases light-extraction efficiency, simplifying optical coupling to free-space or integrated photonic structures. Diamond and SiC also exhibit moderate dielectric constants compared with Si and GaN, which provides a favorable environment for stable spin and optical transitions.

In terms of chemical robustness and biocompatibility, both diamond and SiC exhibit excellent stability in harsh environment and are considered biocompatible. These properties make them attractive for sensing applications in biological, chemical, or high-temperature conditions where Si and III-V semiconductors may degrade or pose toxicity issues (e.g., elemental gallium (Ga)).

Beyond these experimentally established material properties, a generalized scaling relationship has been identified through first-principles evaluations of nuclear-spin abundance and spin-orbit coupling across a broad range of candidate host crystals [67]. The analysis reveals that spin-qubit coherence times decrease with increasing nuclear-spin concentration and stronger spin-orbit coupling. Both diamond and SiC lie in a particularly favorable region of the materials design space: they consist of relatively light elements, exhibit weak spin-orbit interaction, and possess wide bandgaps. These intrinsic factors account for their experimentally observed long spin coherence and optical stability.

Regarding device fabrication, Si and SiC have achieved wafer-scale single-crystal growth and possess highly mature micro- and nano-fabrication technologies due to their long histories in power electronics and semiconductor device engineering. In contrast, diamond currently lack comparable wafer-scale manufacturability, which limits device integration.

In summary, 4H-SiC provides an excellent balance between defect-based SPEs performance (optical stability and long spin coherence) and semiconductor manufacturability (wafer-scale growth, CMOS-compatible processing, and microfabrication). These combined advantages motivate the selection of SiC as the primary host material investigated in this dissertation.

Table 1.2. Major material properties of Si, diamond, SiC, and GaN. Data were extracted from Refs. [68–74].

	Si	4H-SiC	Diamond	GaN
Bandgap (eV)	1.12	3.26	5.47	3.39
Thermal Conductivity ($W\,cm^{-1}\,K^{-1}$)	1.5	4.9	20	2.0
Dielectric Constant	12	9.7	5.5	9.0
Reflection Index at 532 nm	4.2	2.7	2.4	2.4
Biocompatibility	Limited	Excellent	Excellent	Good (elemental Ga is toxic)

1.3 Single-Photon Emitters in Silicon Carbide

As mentioned earlier, SiC is a compound semiconductor composed of silicon and carbon atoms bonded through strong covalent interactions. Research on SiC originally began in the context of blue light-emitting diodes (LEDs) in the 1970s, when various optical and

Table 1.3. The major properties of representative SiC polytypes. Their values are referenced from [68].

Crystal type	3C-SiC	4H-SiC	6H-SiC
Crystal system	Cubic	Hexagonal	Hexagonal
Lattice constant (Å)	a: 4.36	a: 3.08, c: 10.08	a: 3.08, c: 15.12
Bandgap (eV)	2.36	3.26	3.02
Breakdown field ($MVcm^{-1}$)	1.2	2.5	2.8
Intrinsic carrier density (cm^{-3})	0.13	5×10^{-9}	1×10^{-6}
Electron mobility ($cm^2V^{-1}s^{-1}$)	750	1200	100
Hole mobility ($cm^2V^{-1}s^{-1}$)	380	100	70
Dielectric constant	3.3–9.7	3.3–9.7	3.3–9.7

electrical properties were extensively characterized [68]. Later, with the rapid advancement of GaN technology in the 1990s, SiC lost prominence as an optoelectronic material. However, owing to its high thermal conductivity, high breakdown field and wide bandgap, SiC regained attention as a key electronic material capable of stable operation under high-temperature and high-voltage conditions [75].

A major breakthrough in SiC research was achieved through the development of SiC bulk growth techniques, such as the *modified Lely method* (or *seeded sublimation method*), which enabled the fabrication of large-diameter, high-quality single-crystal wafers [76, 77]. This technological milestone was followed by the establishment of high-quality epitaxial layer growth via *step-controlled epitaxy* [78]. In recent years, SiC-based power electronics have progressed from laboratory-level demonstrations to widespread commercial implementation. High-efficiency SiC MOSFETs and diodes are now employed in traction inverters for electric vehicles in Tesla's Model 3 platform [79] as well as in power conversion systems for railway applications such as the N700S "Supreme" Shinkansen [80, 81]. These practical implementations have demonstrated substantial reductions in power loss and system size, benefiting from the intrinsically high breakdown field, low switching loss, and high-temperature capability of SiC devices. As a result, SiC has become a key enabling material for next-generation energy-efficient power electronics.

These technological advances established the foundation for modern SiC power devices and, in parallel, opened new research directions in SiC defect physics. SiC exhibits numerous polytypes with different stacking sequences, and their representative material properties are summarized in Table 1.3. Among them, 4H-SiC has become the most widely adopted polytype in power electronics due to its high electron mobility, large critical electric field, and excellent crystal stability [68].

The electronic and optical properties of SiC are strongly influenced by point defects. Defects, such as the silicon vacancy (V_{Si}), carbon vacancy (V_{C}), carbon interstitial ($\mathrm{C_i}$), divacancies ($V_{\mathrm{Si}}V_{\mathrm{C}}$), silicon antisite ($\mathrm{Si_C}$) defects, and complex forms like $\mathrm{C_{Si}}$-$\mathrm{Si_C}$ have been investigated [68]. These defects not only determine the electronic performance of devices but may also act as SPEs.

1.3.1 SPEs in Bulk SiC

Before the rise of SPEs application, the point defects in bulk SiC were extensively studied for understanding device performance and intrinsic material properties [68]. As introduced

above, many intrinsic point defects are unintentionally or intentionally generated in SiC substrates. Some of these defects can degrade electronic properties. For example, V_C acts as a lifetime killer defect, although they are known to be passivated through thermal oxidation [82, 83]. However, only a small subset of point defects can act as SPEs. Here, several criteria will be explained which must be satisfied for a defect to show PL and support a robust optical cycle.

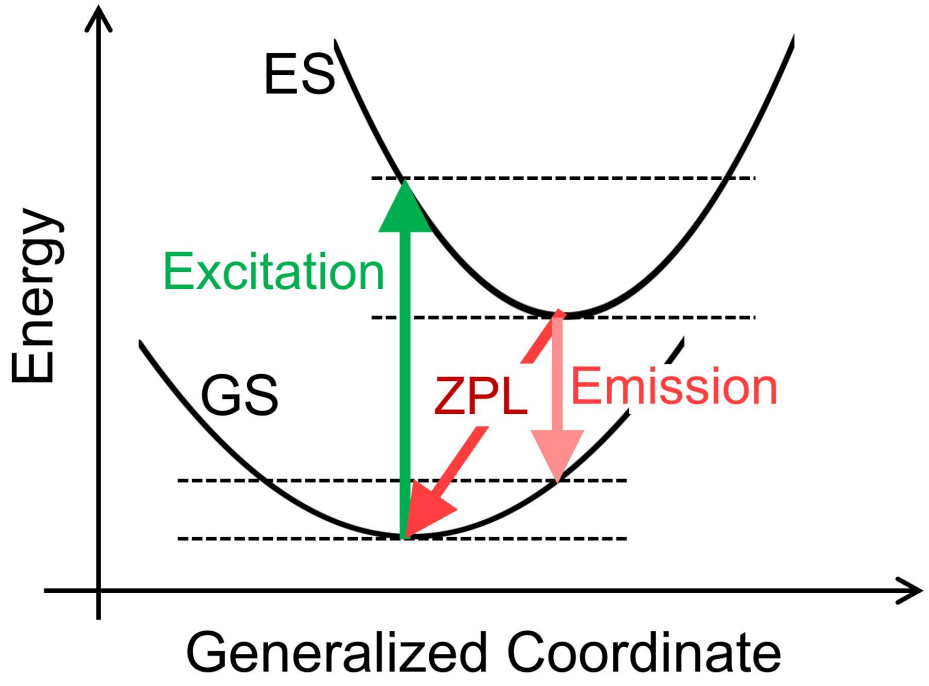

Figure 1.13. Configuration-coordinate illustration of the optical cycle of a defect. Optical excitation promotes the system from GS to ES. Radiative relaxation occurs either through the ZPL or through phonon-assisted emissions forming PSB.

Figure 1.13 illustrates a typical configuration-coordinate (CC) diagram, which describes the optical cycle of a defect. In the excitation step, indicated by the green arrow, an optical transition promotes the defect from the GS to the ES according to the Franck–Condon principle. After excitation, the system rapidly relaxes toward the ES minimum through phonon emission. From this relaxed ES minimum, radiative decay proceeds through two pathways, as indicated by the red and pink arrows in Fig. 1.13. One pathway corresponds to a purely electronic transition without phonon involvement, producing the ZPL. The other pathway involves phonons and gives rise to the phonon sideband (PSB). For defects to function as SPEs, several aspects of the CC diagram are particu-

larly important. The shape and relative configuration of the GS and ES potential-energy surfaces determine whether optical emission can compete with non-radiative relaxation. In particular, the separation between their minima and the competition between radiative and non-radiative transition rates govern the dominant recombination process. If non-radiative processes dominate, the PL becomes weak or fully quenched and the defects cannot operate as SPEs. In addition, charge-state stability during optical excitation is also necessary. In summary, only defects satisfying these requirements—including sufficient GS–ES wavefunction overlap, suppressed non-radiative relaxation, and a stable charge configuration—can exhibit bright and stable PL and thus act as SPEs in SiC [84].

The representative SPEs in 4H-SiC—V_{Si}^{-}, $V_{\mathrm{C}}V_{\mathrm{Si}}^{0}$, nitrogen-vacancy ($\mathrm{N_C}V_{\mathrm{Si}}^{0}$), carbon antisite-vacancy ($\mathrm{C_{Si}}V_{\mathrm{C}}^{0}$), vanadium center ($\mathrm{V_{Si}^{4+}}$)—and their optical properties and structures are summarized in Table 1.4 and Fig. 1.14.

In particular, a coherent control of single spin has been demonstrated for V_{Si}^{-} [85–87], $V_{\mathrm{C}}V_{\mathrm{Si}}^{0}$ [88, 89], $\mathrm{N_C}V_{\mathrm{Si}}^{-}$ [64, 90, 91], and $\mathrm{V_{Si}^{4+}}$ centers [92, 93]. Note that vacancies are denoted in italic style (e.g., V_{Si}, V_{C}), whereas vanadium is written in roman style (e.g., $\mathrm{V_{Si}}$).

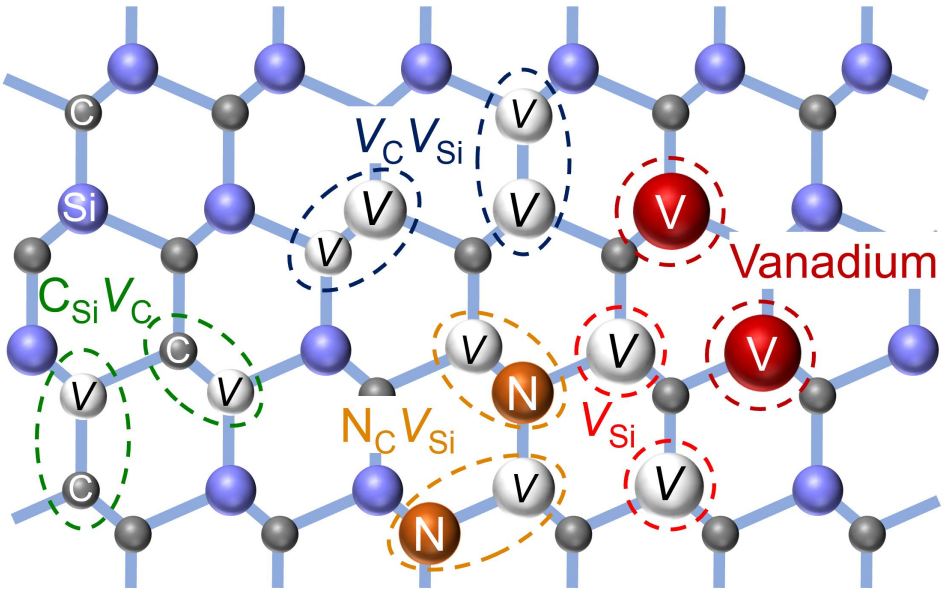

Figure 1.14. Summary of representative SPEs in 4H-SiC. In this dissertation, vacancies are denoted in italic style (e.g., V_{Si}, V_{C}), whereas vanadium is written in roman style (e.g., $\mathrm{V_{Si}}$). Data are compiled from Refs. [64, 85, 86, 88, 89, 94, 95].

These SPEs are typically formed by introducing defects through electron irradiation or ion implantation, followed by high-temperature annealing to recover crystallinity. If an-

Table 1.4. Summary of representative SPEs in 4H-SiC and their properties. Values are compiled from Refs. [64, 85, 86, 88, 89, 94–96].

Defects	Wavelength (nm)	Spin (S)
$V_{\mathrm{Si}}{}^{-}$	862, 917	3/2
$V_{\mathrm{C}}V_{\mathrm{Si}}{}^{0}$	1078–1132	1
$\mathrm{N_C}V_{\mathrm{Si}}{}^{-}$	1223–1244	1
$\mathrm{C_{Si}}V_{\mathrm{C}}{}^{0}$	648–676	N/A
$\mathrm{V_{Si}^{4+}}$	1278, 1335	1/2

nealing is insufficient, the optical properties degrade due to non-radiative recombination associated with implantation damage and residual strain. Because SiC features strong covalent bonding comparable to diamond, defect formation generally requires high implantation energies and elevated annealing temperatures (often exceeding 1000°C). Some defect species are annealed out during recovery, making defect engineering a delicate process requiring precise control of fluence and thermal budgets.

Furthermore, recent studies have integrated SPEs into photonic crystal cavities and waveguide structures, which enhance light-matter coupling, improve emission directionality, and enable high Purcell-factors [97, 98].

Utilizing these defect-based SPEs, key technologies have been developed. For example, key functions to form entangled photon pairs, indistinguishable photons has been achieved by the same V_{Si} center on the sample. In addition, temperature and magnetic field sensing have also been demonstrated [99–101]. Moreover, bias-controlled switching of PL intensity has been reported, depending on changes in their charge states, demonstrating the compatibility of SiC with CMOS-level processes [102, 103].

In summary, bulk SiC hosts a diverse range of optically active point defects that exhibit stable emission and long spin coherence. The combination of a wide bandgap, strong covalent bonding, and mature semiconductor processing makes SiC a uniquely promising platform for developing scalable solid-state SPEs.

1.3.2 SPEs at SiO_2/SiC Interfaces

In recent years, a novel type of SPE has been reported at the SiO_2/SiC interface [104, 105], hereafter referred to as the interface SPEs in this dissertation. These SPEs are readily formed during thermal oxidation, as illustrated in Fig. 1.15, which is a standard process in SiC device fabrication and requires no intentional ion implantation. This feature provides exceptionally high compatibility with established semiconductor manufacturing processes. Interestingly, post-oxidation annealing in nitric oxide (NO) [106] and Ar [107] atmospheres reduces the density of interface SPEs, and both processes are already known to suppress interface defects that degrade carrier mobility in MOSFETs, as illustrated in Fig. 1.15.

Another notable feature is their intense luminescence even at room temperature, which exceeds that of the NV center in diamond [104, 108]. Furthermore, the interface SPEs embedded in device exhibit emission that depends on applied voltage or injection current, enabling the optical signal to be electrically switched on and off [108, 109]. This property is particularly attractive for realizing electrically drivable quantum light sources. Combined with the technological maturity of SiC MOSFETs, these characteristics suggest that interface SPEs are highly compatible with CMOS technology and thus promising for integration into hybrid quantum-classical devices and on-chip photonic circuits. Moreover, given the excellent biocompatibility and chemical stability of SiC, interface SPEs could also be utilized for biosensing and quantum optoelectronic devices.

Despite these advantages, several challenges remain unresolved. One of the most critical issues is strong variation in emission wavelength and intensity, which hinders practical implementation [105, 108]. Moreover, as described earlier, luminescence of the

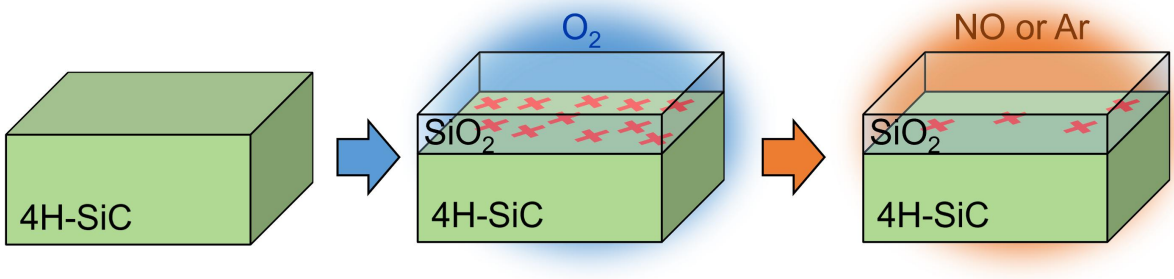

Figure 1.15. Generation and annihilation of the interface SPEs by oxidation and post-oxidation annealing. Red crosses indicate the interface SPEs.

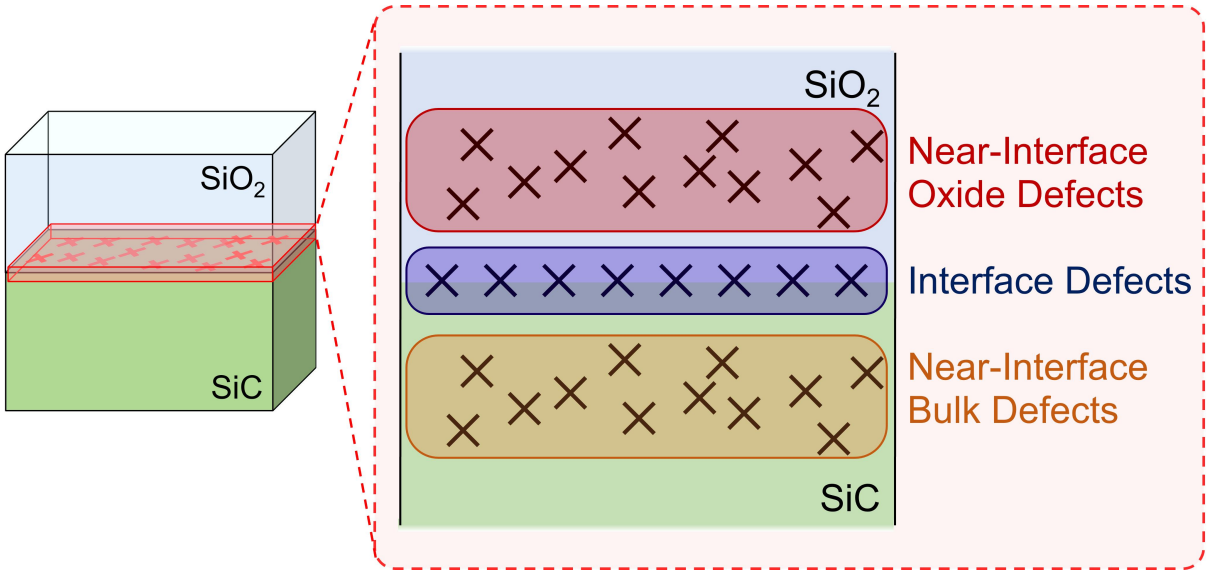

Figure 1.16. Schematic illustration of defect locations at the SiO_2/SiC interface.

interface SPEs can be electrically switched. However, the brightness from some color centers remain constant under any applied voltage [108, 109]. Controlling where the SPEs are formed is also difficult. During oxidation, they are randomly formed at the interface. In addition, the microscopic origin of the interface SPEs remains under debate because multiple defect species coexist near or exactly at the interface. Clues to their origin have been reported. The emission polarization aligns with the crystal orientation of the SiC lattice, suggesting that the defects responsible for the SPEs reside on the SiC side of the SiO_2/SiC interface [104, 110]. In contrast, removing the oxide film by hydrofluoric (HF) acid eliminates the SPEs [104], implying that some of the interface SPEs are located on the oxide side.

At the SiO_2/SiC interface, the local atomic configuration changes abruptly compared with the bulk crystal, and therefore the defect species that appear in this region are distinct from those in bulk SiC. Moreover, defects are known to exist not only exactly at the interface but also slightly both inside the oxide and the bulk SiC, as illustrated in Fig. 1.16. Representative defect candidates proposed or identified for each region are summarized in Fig. 1.17. On the SiC side, DFT calculations have predicted several configurations such as dicarbon-antisite $(C_2)_{Si}$ [111, 112] and oxygen-related complexes [107, 113]. Deep-level transient spectroscopy (DLTS) measurements have experimentally revealed oxidation-induced defects referred to as OI-1 to OI-3 [114]. Within the SiO_2 layer, theoretical studies have suggested that carbon-related defects, including carbon dimers

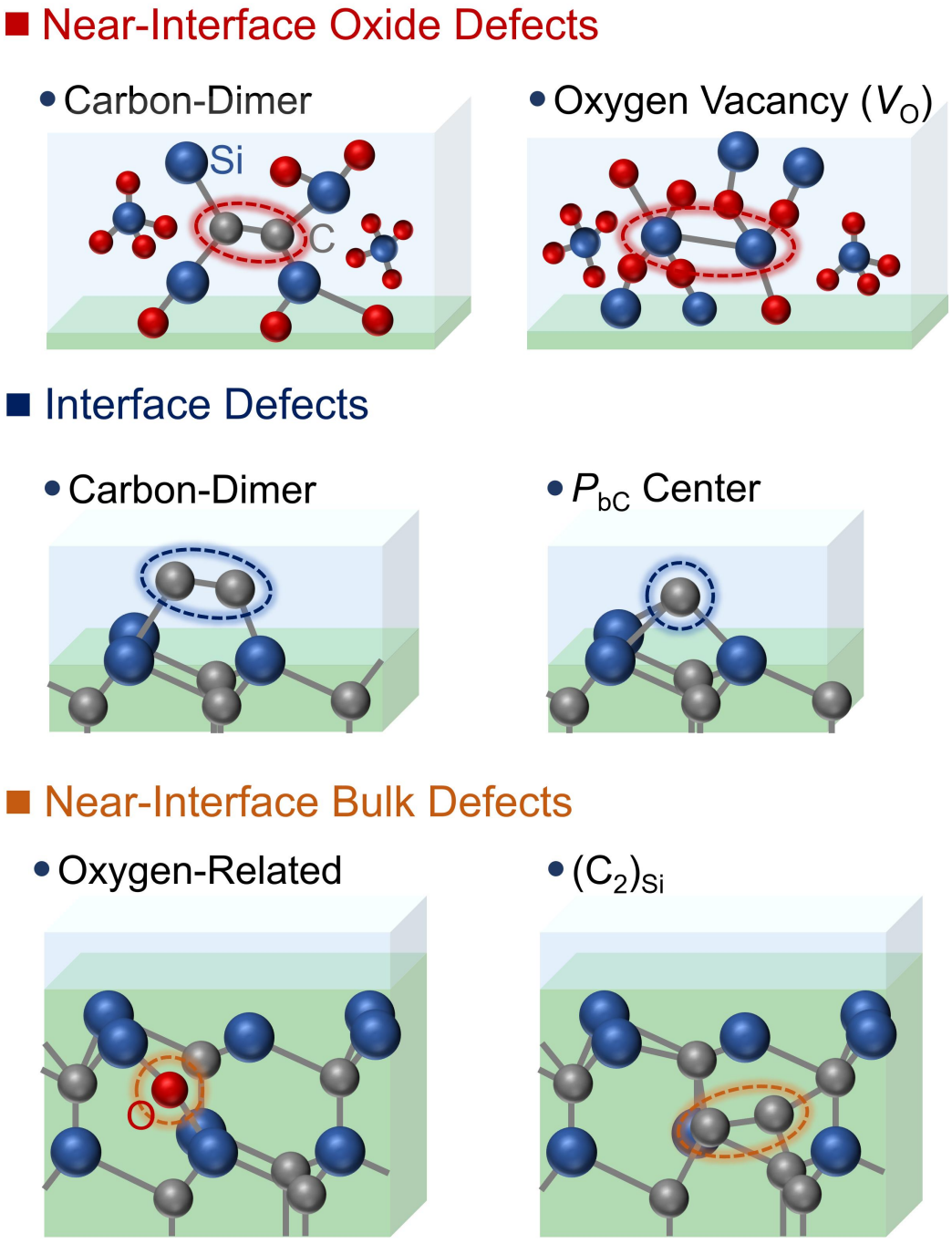

Figure 1.17. Representative point defect candidates proposed or identified near/at the SiO_2/SiC interface. The upper panel shows typical near interface oxide defects, such as carbon-dimers and V_O. The middle panel illustrates just interface defects, including carbon-dimers and P_{bC} center. The lower panel shows near-interface bulk defects in SiC, such as oxygen-related complexes and dicarbon-antisite $(C_2)_{Si}$.

incorporated into the oxide network [83, 112], as well as oxygen vacancies V_O [115], can form electrically active trap states. Exactly at the interface, a carbon dangling bond known as the P_{bC} center has been experimentally identified by electrically detected magnetic resonance (EDMR) [116], and numerous theoretical and experimental works have further suggested the presence of additional carbon-related configurations in this interface region [83, 112, 117–119].

1.4 Overview of This Dissertation

This dissertation investigates the understanding and control of SPEs located at the SiO_2/SiC interface, aiming to realize scalable and electrically controllable quantum light sources on a technologically mature semiconductor platform. Building on the general background of defect-based SPEs and the material advantages of SiC introduced in this chapter, the following chapters focus on how oxidation and post-oxidation annealing conditions govern the density as well as the optical and electrical properties of interface color centers.

Chapter 2 describes the optical setup and measurement principles of the home-built confocal laser scanning microscope (CLSM) used throughout this dissertation. Because SPEs are localized at the interface, conventional wide-field optical microscopy cannot provide sufficient sectioning capability to isolate their emission. Chapter 2 therefore introduces the configuration of the CLSM, including the excitation and detection paths, the spatial-filtering scheme, and the role of the pinhole for achieving three-dimensional optical sectioning. Furthermore, the chapter explains how confocal PL mapping enables identification and localization of individual color centers at the interface, and how HBT measurements are implemented within the same optical platform to evaluate the second-order autocorrelation function $g^{(2)}(\tau)$. The design of the detection optics, including the avalanche-photodiode (APD) arrangement and timing electronics, is also presented. In addition, the chapter describes the spectrometer configuration used for PL spectroscopy and how spectral signatures are extracted. Overall, Chapter 2 provides the experimental foundation required for the subsequent chapters, where the density control, optical properties, and microscopic origins of interface SPEs are systematically investigated.

Chapter 3 attempts to control of color-center density at the SiO_2/SiC interface through systematic variation of oxidation and annealing conditions. High-temperature oxidation

and post-oxidation annealing in a CO_2 atmosphere are employed to form SiO_2/SiC structures. Confocal PL mapping is conducted to evaluate the spatial distribution and density of the interface color centers. Subsequently, their PL spectrum and single photon characteristics were evaluated. In parallel, *C–V* measurements of SiC MOS capactirors are conducted to quantify electrically active defects, including oxide traps, effective fixed charges, and interface states below midgap energy level. By comparing optical and electrical characteristics across different processing conditions, this chapter elucidates how high-temperature oxidation and CO_2 annealing suppress both charges and color-center densities. Consequently, it is demonstrated that the density of interface SPEs can be varied over a wide range, spanning orders of magnitude from 10^5 to 10^7 cm^{-2}. In other words, CO_2 annealing has the ability to spatially isolate the interface SPEs.

Chapter 4 focuses on elucidating how post-oxidation CO_2 annealing governs the formation and evolution of color center density at the SiO_2/SiC interface. By systematically quantifying both the color center and the electrically active defect densities, this chapter demonstrates that CO_2 annealing suppresses color centers and electrically active defects more rapidly and effectively than Ar annealing. As a result, CO_2 annealing enables wide-range tunability of the color center density—from 5.6×10^5 cm^{-2} to 7.4×10^7 cm^{-2}—even when the annealing temperature is fixed at 1200°C, highlighting that annealing duration alone can serve as an effective control parameter. The chapter further reveals that the bright-spot density scales with the effective fixed charge density, predominantly associated with deep acceptor-type interface defects, and that improving the SPE ratio requires substantial suppression of background luminescence. These results collectively establish a practical and reliable strategy for forming interface SPEs through controlled CO_2 annealing.

Chapter 5 builds upon the experimental results presented in Chapters 3 and 4 and provides an integrated discussion of the interface SPEs. First, it examines the mechanisms responsible for the reduction of color centers at the interface and for the formation of spatially separated SPEs under high-temperature oxidation and post-oxidation CO_2 annealing, clarifying why CO_2 annealing is significantly more effective in reducing the density than Ar annealing. Second, it analyzes the relationship between the color center density obtained from confocal PL mapping and the electrically active defect density extracted from *C–V* measurements, and discusses the origin of the large discrepancy between color centers and electrically active defects. Third, it considers possible microscopic

origins of the interface SPEs, focusing on carbon-related candidates on the SiC side of the interface and their consistency with the observed trends in defect reduction. Through these discussions, this section outlines a strategy for designing oxidation and annealing conditions that realize spatially isolated, high-purity SPEs at the SiO_2/SiC interface.

Chapter 6 summarizes the main conclusions of this work and discusses their implications for quantum applications. The key achievements lie in controlling the density and spatial distribution of interface SPEs and in correlating color centers with electrically active interface defects. Finally, possible directions for future research are outlined, including microscopic identification of the responsible defect configurations, extension to spin-resolved measurements, and integration of interface SPEs into electrically driven and photonic-cavity structures for advanced quantum information and sensing applications.

Chapter 2

Principles of Confocal Laser Scanning Microscope and Measurements

2.1 Introduction

As introduced in Chapter 1, SPEs arise from atomic-scale point defects whose optical emission originates from an angstrom-sized region. Detecting such highly localized color centers requires an optical microscope with extremely high spatial resolution in all three dimensions. Moreover, the SPEs studied in this work are located near the SiO_2/SiC interface, typically within several tens to several hundreds of nanometers from the surface. In this depth range, conventional wide-field microscopy cannot adequately discriminate the interface-emitted PL from the background originating in the SiC epi-layer or substrate, because out-of-focus fluorescence is superimposed onto the image. Therefore, an optical system capable of suppressing out-of-focus background and isolating PL from a well-defined depth region is indispensable. For this reason, a CLSM with optical sectioning capability is essential [120]. Historically, the optical and spin properties of NV centers in diamond had been studied in ensembles containing many defects [121, 122]. The first experimental isolation and optical detection of a single NV center was achieved in 1997 using a CLSM combined with ODMR [35]. This breakthrough enabled the measurement of individual electronic spins in the solid state, and was soon followed by the demonstration of stable solid-state single-photon emission from a single NV center by HBT measure-

ments [123]. This chapter describes the principles of the confocal microscope system that is indispensable for the present study, together with the measurement techniques used to characterize individual color centers. Specifically, three types of measurements were performed: (i) confocal PL mapping to identify the spatial distribution of color centers, (ii) optical emission measurements to evaluate their photoluminescence properties, and (iii) HBT measurements to determine their single-photon characteristics.

2.2 Setup of Confocal Laser Scanning Microscope

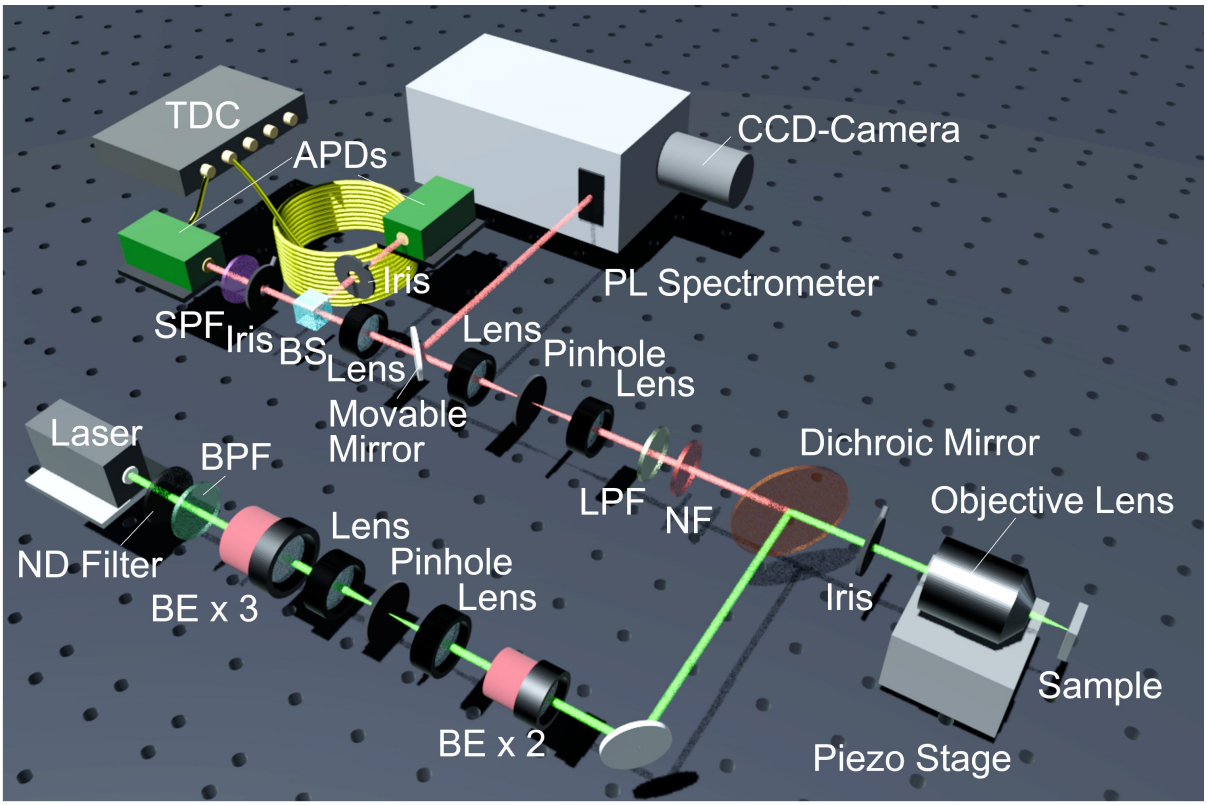

Figure 2.1. Schematic of the home-built CLSM used for single defect measurements.

Figure 2.1 shows a schematic of the home-built CLSM used in this work. A continuous-wave 532 nm laser is first attenuated with variable neutral-density (ND) filters to adjust the excitation power. The beam is then spectrally cleaned by a band-pass filter (BPF). Subsequently, the laser is expanded by a beam expander (BE) to approximately three times its original beam width. This enlargement allows the beam to fill the entrance pupil of the downstream lens–pinhole–lens configuration, which serves as a spatial filter and produces a nearly Gaussian beam profile. A second BE and iris in front of objective

adjust the beam diameter so that the beam appropriately fills the entrance aperture of the objective lens. The cleaned and size-optimized beam is then directed onto a 550 nm cut-on dichroic mirror, which reflects the excitation wavelength toward the objective lens that focuses the light onto a color center in the sample. The objective is mounted on a three-axis piezo stage. By scanning the piezo stage with a travel range of approximately 100 µm in each direction, while monitoring the PL signal, confocal PL mapping images with high spatial resolution in all three dimensions can be obtained.

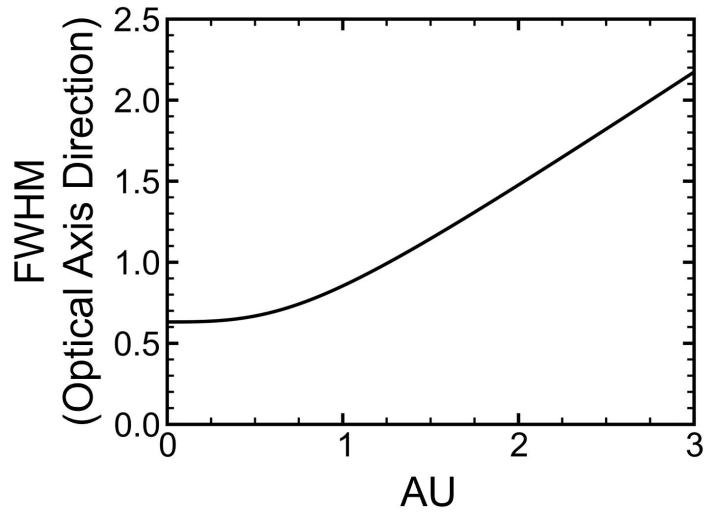

Figure 2.2. FWHM of the optical section thickness as a function of pinhole diameter, expressed in AU, calculated for an objective lens with NA = 0.9 under 532 nm [120].

The PL emitted from color centers in the sample is collected by the same objective lens and transmitted through a dichroic mirror. The collected PL first passes through a notch filter (NF) to suppress residual laser light and then through a long-pass filter (LPF) to remove unwanted background. For confocal PL mapping and HBT measurements, a 600 nm LPF is used to eliminate the Raman peaks, whereas for PL spectroscopy, a 550 nm LPF is employed. A lens subsequently focuses the PL onto a pinhole placed at the conjugate image plane of the objective, providing spatial filtering and enabling optical sectioning of the sample. The pinhole diameter is typically chosen with reference to the Airy disc. Figure 2.2 shows the dependence of the axial full width at half maximum (FWHM) along the optical axial direction on the pinhole size for an objective lens with a numerical aperture (NA) of 0.9 [120], which is used in both Chapters 3 and 4. As seen in this figure, the FWHM increases steadily and begins to rise rapidly when the pinhole

size exceeds approximately 0.5 Airy units (AU), leading to degraded spatial resolution along the z-direction. This study consistently adopted a pinhole size of 20 µm, equal to 0.43 AU. The light transmitted through the pinhole is then recollimated by another lens and directed to a movable mirror. By switching the movable mirror, the system can operate either in PL spectroscopy mode or in confocal PL mapping and HBT measurement modes.

When the movable mirror is flipped into the spectroscopy path, the PL from the color centers is directed into a Czerny–Turner spectrometer and subsequently detected by a charge-coupled device (CCD) camera, enabling PL spectroscopy measurements. When the movable mirror is flipped into the confocal PL mapping and HBT path, the PL is directed to a 50:50 non-polarizing beam splitter (BS), which divides the photons into two paths of equal length and delivers them to two APDs. Narrowed iris diaphragms are placed in front of each APD to suppress scattered light. The outputs of the APDs are connected to a time-to-digital converter (TDC), which records the arrival time of each detected photon, enabling second-order autocorrelation measurements in the HBT configuration. During HBT measurements, a short-pass filter (SPF) positioned in front of one APD is inserted into the optical path to suppress detector back-flash light emitted when the other APD detects a photon [123].

2.2.1 Confocal PL Mapping

Figure 2.3 (a) presents a focused illustration of the optical configuration around the objective. To evaluate the distribution of interface color centers, an x–z scan is first performed, as shown in Fig. 2.3 (b). A representative x–z mapping image is shown in Fig. 2.4 (a). The SiO_2 layer and the SiC epitaxial layer appear dark because they do not have color centers in the mapping area, whereas several vertically elongated bright features emerge at the SiO_2/SiC interface. These bright features correspond to individual color centers. It should be noted that, due to the high refractive index of SiC ($n \approx 2.65$), the apparent thickness of the SiC epitaxial layer in the z-direction is reduced by this factor in confocal imaging.

Once the depth (z) position of the interface is identified, the z coordinate is fixed, and an x–y raster scan is performed as illustrated in Fig. 2.3 (c). The resulting PL map, shown in Fig. 2.4 (b), clearly resolves multiple isolated circular bright spots distributed across the sample plane, each representing a single color center.

Owing to the high spatial resolution of the CLSM, individual color centers can be examined in more detail. Figure 2.5 displays representative x–z and x–y images of a single isolated color center. In the x–y image, the color center appears as a single diffraction-limited spot. The diffraction-limited spot, characterized by a nearly Gaussian profile, confirms that the signal originates from a single point defect. In contrast, in the x–z

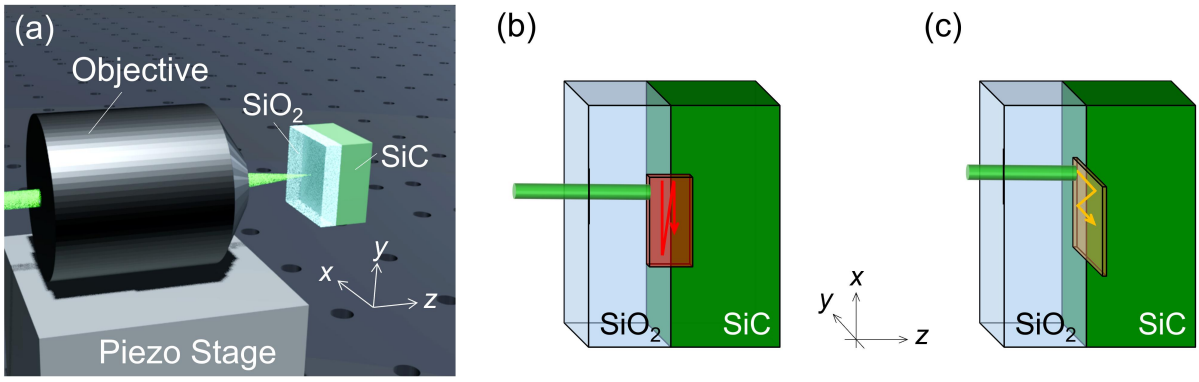

Figure 2.3. Schematic illustrations of the confocal PL mapping procedure. (a) Optical configuration around the objective lens and the sample mounted on a three-axis piezo stage. (b) An x–z scan is performed to identify the location of the interface region. (c) After selecting the appropriate depth, an x–y raster scan is carried out to obtain the distribution of the color centers.

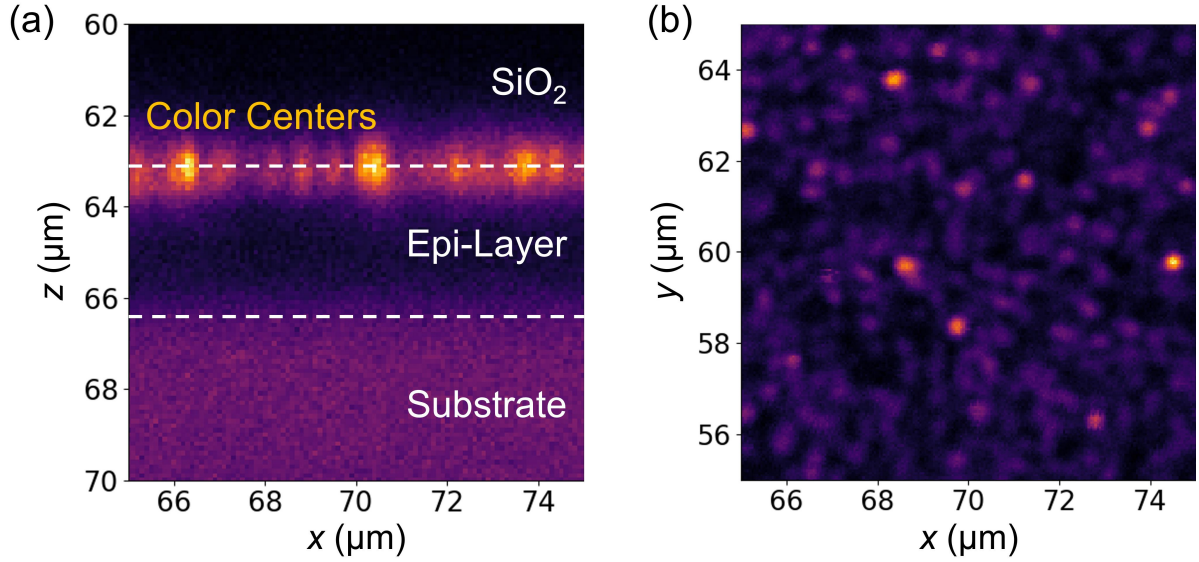

Figure 2.4. Typical confocal PL mapping images of the SiO_2/SiC sample by (a) x–z and (b) x–y scans. Multiple isolated bright spots corresponding to individual color centers are visible due to the high spatial resolution enabled by the confocal optical setup.

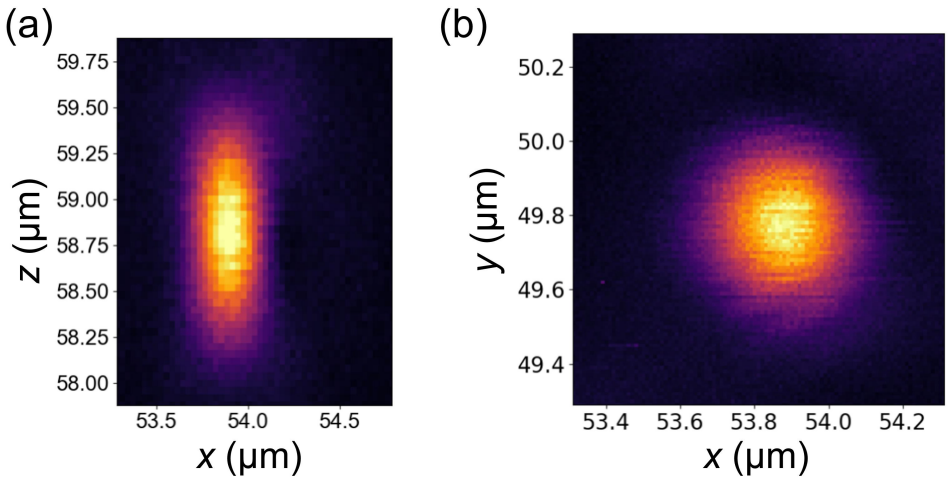

Figure 2.5. Confocal PL images of a single isolated color center by (a) x–z and (b) x–y scans.

image, the color center appears elongated along the depth (z) direction. This is a well-known characteristic of confocal microscopy: although lateral resolution is diffraction-limited, the axial resolution is inherently poorer, leading to an extended point-spread function along the optical axis.

For these isolated color centers, PL spectroscopy and HBT measurements were performed to determine their optical properties and single-photon characteristics.

2.2.2 PL Spectroscopy

PL spectra from individual color centers were acquired using a Czerny–Turner type grating spectrometer coupled to the CLSM. Figure 2.6 illustrates the layout of the spectrometer.

The PL emitted from the selected color center is directed toward the entrance slit of the spectrometer. The entrance slit defines the spectral resolution and also limits the throughput. The light is collimated by a spherical mirror and directed onto a rotatable diffraction grating, where it is angularly dispersed by wavelength. A second mirror focuses the dispersed light onto the exit plane, where an adjustable exit slit selects the desired portion of the spectrum. The transmitted light is detected by a CCD camera.

This Czerny–Turner configuration provides high optical throughput and sufficient spectral resolution to clearly identify spectral features. A representative PL spectrum obtained at room temperature is shown in Fig. 2.7. Distinct peaks at 555 nm and 561 nm correspond to the longitudinal optical (LO) and transverse optical (TO) Raman modes

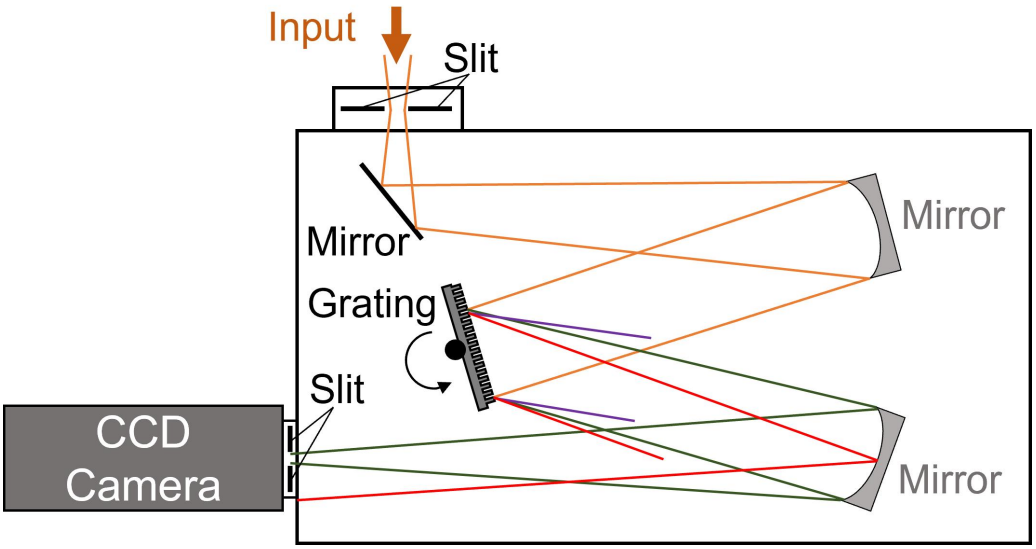

Figure 2.6. Schematic illustration of the Czerny–Turner-type spectrometer used for PL spectroscopy. The PL enters through the entrance slit, is collimated by a mirror, dispersed by a rotatable diffraction grating, and refocused by another mirror onto the exit slit before detection.

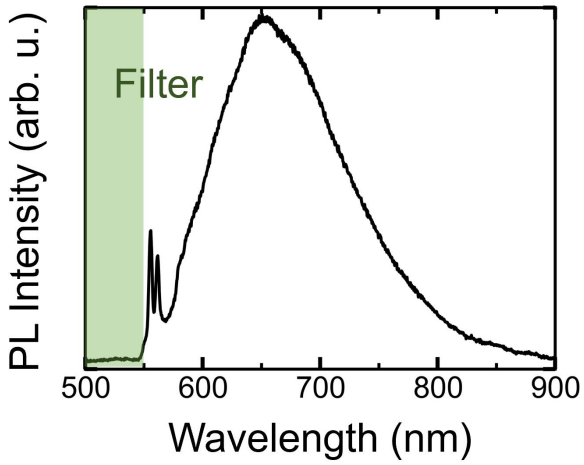

Figure 2.7. Typical PL spectrum obtained from a single color center in the SiO_2/SiC sample. The shaded region indicates the spectral range blocked by filters to suppress residual 532 nm excitation light.

of 4H-SiC, respectively. These Raman features arise from Stokes-shifted scattering of the 532-nm excitation laser, where incident photons lose energy due to lattice vibrations. The two additional features appearing around 580–600 nm originate from second-order Stokes Raman processes involving multi-phonon scattering [124, 125].

Although the measurement is performed at room temperature, and the ZPL is not clearly resolved, a broad feature around 600 nm is observed. This emission is attributed to the ZPL of the color centers, with the phonon-side bands (PSB) extending toward longer wavelengths. By analyzing these spectral features, the emission characteristics of the color centers can be evaluated.

2.2.3 HBT Measurements

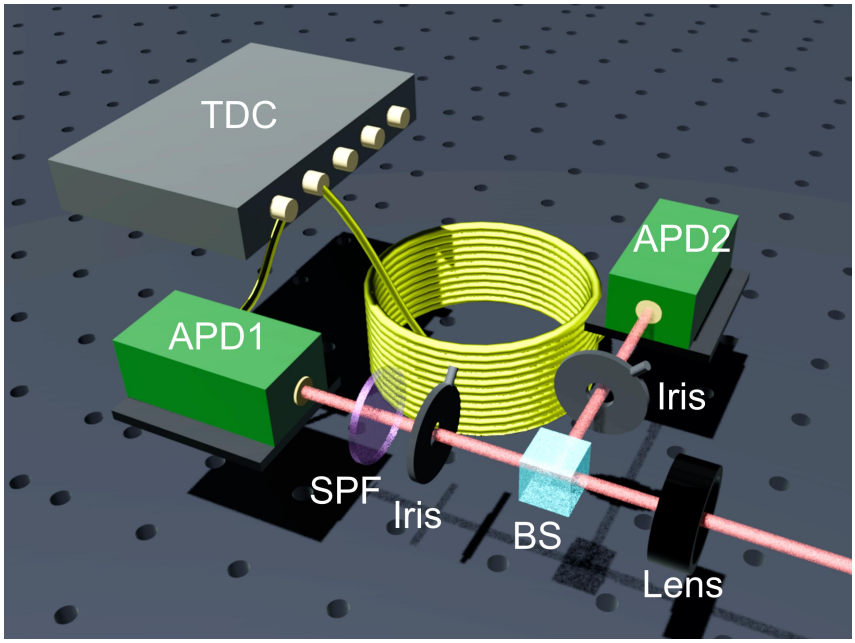

Figure 2.8. Enlarged view of the HBT setup shown in Fig. 2.1. The PL from color center is split by a half BS and detected by APD1 and APD2, while the photon arrival times are recorded using a TDC.

Figure 2.8 shows an enlarged view of the detection setup used for HBT measurements [126]. The purpose of the HBT setup is to investigate the intensity correlations of the PL from color center. The photon arrival times from the two detectors are used to construct a histogram of detection-time differences, from which the second-order autocorrelation function $g^{(2)}(\tau)$ is obtained. This quantity reveals information that cannot

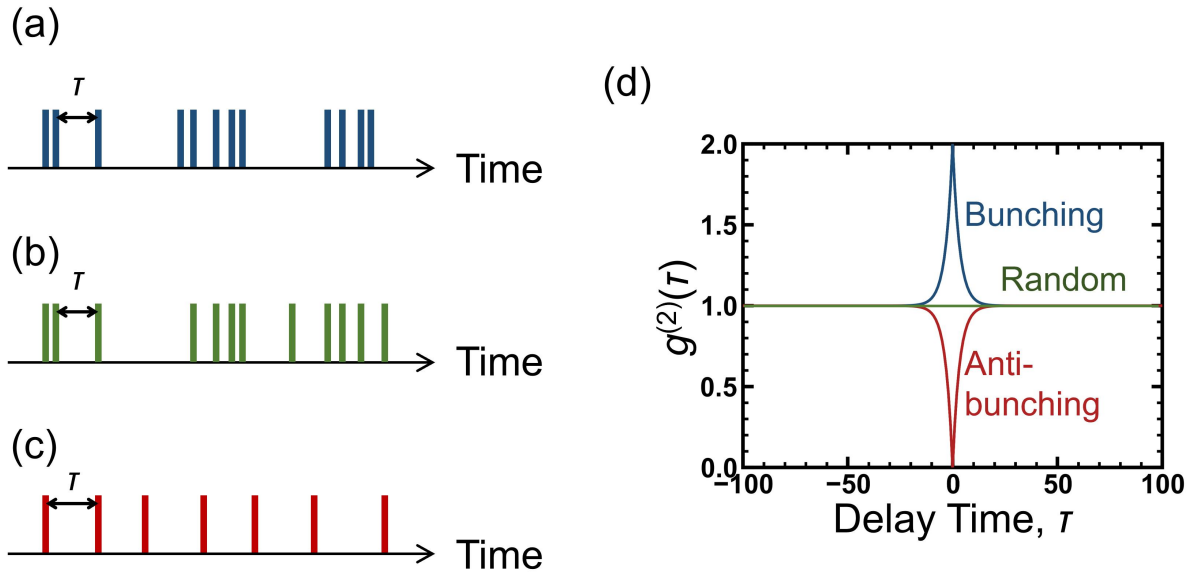

Figure 2.9. Representative photon-arrival time traces for (a) bunched, (b) random, and (c) anti-bunched light. (d) Corresponding second-order autocorrelation functions $g^{(2)}(\tau)$, showing $g^{(2)}(0) > 1$ for bunching, $g^{(2)}(0) = 1$ for Poissonian light, and $g^{(2)}(0) < 0.5$ for a SPE.

be accessed by first-order (phase) coherence measurements, which only probe wave-like interference. In contrast, the second-order autocorrelation function reflects the particle-like statistics of the emitted photons and therefore distinguishes between classical and quantum light [127].

Figure 2.9 illustrates the basic photon statistics observed in an HBT measurement. Figure 2.9 (a) shows examples of photon arrival time sequences. When photons tend to arrive in clusters, the coincidence probability at $\tau = 0$ becomes enhanced, leading to a bunching peak as shown in Figure 2.9 (d). For a Poissonian (random) source, the coincidence rate remains flat around unity. In contrast, when the emitter releases photons strictly one-by-one, simultaneous detections at APD1 and APD2 are strongly suppressed, producing a dip at $\tau = 0$ ns—the characteristic anti-bunching signature that identifies a SPE.

More quantitatively, the second-order autocorrelation function is defined as

$$g^{(2)}(\tau) = \frac{\left\langle \hat{a}^\dagger(t)\,\hat{a}^\dagger(t+\tau)\,\hat{a}(t+\tau)\,\hat{a}(t)\right\rangle}{\left\langle \hat{a}^\dagger(t)\,\hat{a}(t)\right\rangle^2}, \tag{2.1}$$

where $\hat{a}^\dagger$ and $\hat{a}$ are the photon creation and annihilation operators. Evaluating Eq. (2.1)

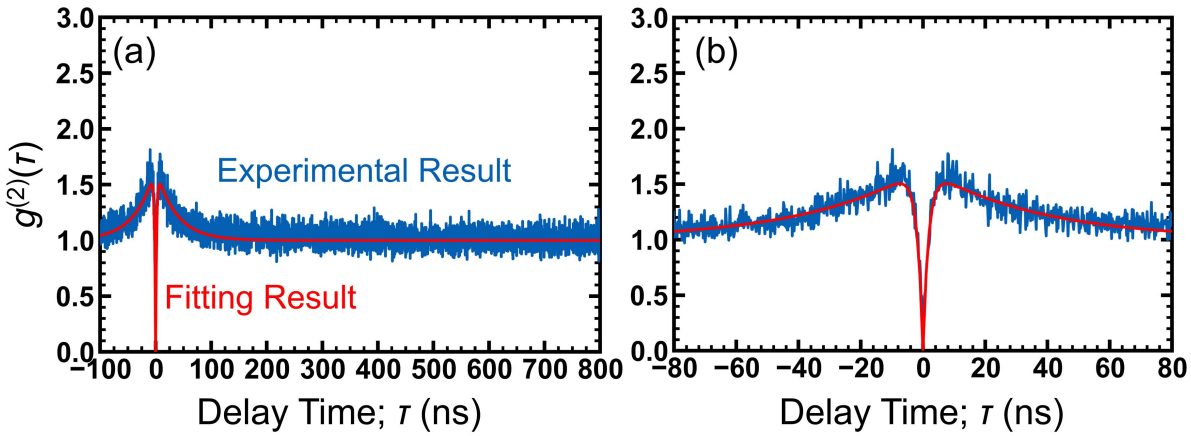

Figure 2.10. Representative second-order autocorrelation function $g^{(2)}(\tau)$ measured from a single color center at the SiO_2/SiC interface (blue). (a) Wide time range. (b) Magnified view near $\tau = 0$. The solid red curve represents the fit using the three-level model of Eq. (2.3).

for an n-photon Fock state gives

$$g^{(2)}(0) = \begin{cases} 0, & n = 1, \\ 1 - \dfrac{1}{n}, & n \geq 2, \end{cases} \tag{2.2}$$

which shows that $g^{(2)}(0)$ becomes zero for a single-photon state. In practice, a value of $g^{(2)}(0) < 0.5$ is widely accepted as the criterion confirming the presence of single-photon emission, because it cannot be achieved by any classical light field [46, 123].

Figure 2.10 shows a representative $g^{(2)}(\tau)$ measurement obtained from an individual color center. Unlike the ideal anti-bunching behavior illustrated in Fig. 2.9, the experimental result exhibits a clear bunching tail in addition to the anti-bunching dip at about $\tau = \pm 10$ µs. This feature indicates that the emitter does not behave as a simple two-level system; instead, it follows a three-level model with a metastable shelving state, as shown in Fig. 2.11.

To quantitatively analyze the photon statistics, the experimental $g^{(2)}(\tau)$ curve was fitted using the standard three-level rate-equation model. In this model, p_g, p_e, and p_m denote the occupation probabilities of the ground (g), excited (e), and metastable (m) states, respectively. The parameters γ_{ij} represent transition rates from state i to state j (e.g., γ_{ge}: optical excitation rate, γ_{eg}: radiative decay rate, γ_{em}: intersystem-crossing rate, and γ_{mg}: relaxation rate from the metastable state back to the ground state).

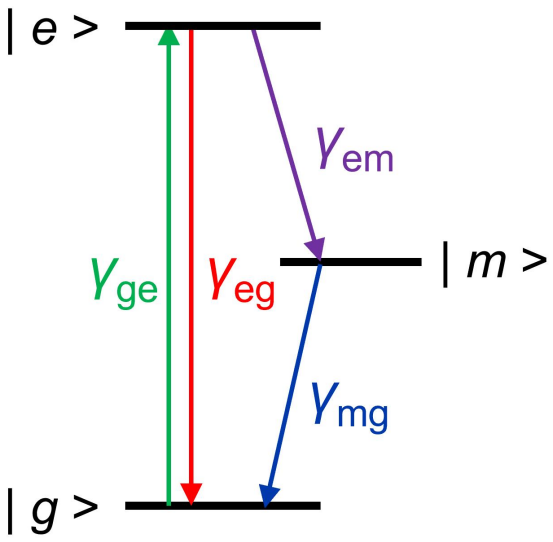

Figure 2.11. Three-level model used to describe the photon-emission dynamics of interface color centers. γ_{ge}: optical excitation rate, γ_{eg}: radiative decay rate, γ_{em}: shelving rate to the metastable state, γ_{mg}: deshelving rate back to the ground state.

The population dynamics of the three states are described by the coupled differential equations [123, 128, 129]:

$$\begin{pmatrix} \dot{p}_g \\ \dot{p}_e \\ \dot{p}_m \end{pmatrix} = \begin{pmatrix} -\gamma_{ge} & \gamma_{eg} & \gamma_{mg} \\ \gamma_{ge} & -\gamma_{eg} - \gamma_{em} & 0 \\ 0 & \gamma_{em} & -\gamma_{mg} \end{pmatrix} \begin{pmatrix} p_g \\ p_e \\ p_m \end{pmatrix}. \tag{2.3}$$

Solving the rate equations in Eq. (2.3) yields the general expression for the second-order autocorrelation function of a three-level system:

$$g^{(2)}(\tau) = 1 - (1-a)\exp\left(-\frac{|\tau|}{\tau_1}\right) + a\exp\left(-\frac{|\tau|}{\tau_2}\right). \tag{2.4}$$

The parameters τ_1 and τ_2 represent the characteristic decay times associated with fast and slow dynamical processes in the system, respectively. In particular, τ_1 is mainly determined by the excitation and radiative decay rates between the ground and excited states, whereas τ_2 is governed by shelving in the metastable state and the relaxation rate back to the ground state. The coefficient a quantifies the strength of photon bunching and reflects the relative population flow through the metastable state. When the metastable pathway is negligible ($a \approx 0$), the autocorrelation reduces to the two-level form, in which no bunching behavior is present.

As shown by the red fitting curves in Fig. 2.10, the three-level model reproduces both the anti-bunching cusp near $\tau = 0$ and the bunching behavior at longer delays, indicating the presence of a metastable state. Although the extracted transition rates can in principle provide information on quantities such as the ES lifetime and shelving-state dynamics, a comprehensive analysis requires laser-power-dependent measurements and was therefore beyond the scope of the present study, which focuses on a representative SPE. For this representative SPE, the extracted ES lifetime was 3.0 ns, which is comparable to the previously reported value of 2.4 ± 0.3 ns for SiO_2/SiC color centers [104].

The HBT measurements in this study were carried out following this procedure, and the resulting $g^{(2)}(\tau)$ functions were used to verify whether the color centers at the SiO_2/SiC interface exhibit single-photon characteristics.

Chapter 3

Density Control on Color Centers at SiO_2/SiC Interface by Oxidation and Annealing

This chapter is primarily based on the following publication:
*T. Nakanuma et al., "Control on the density and optical properties of color centers at SiO_2/SiC interfaces by oxidation and annealing," Applied Physics Letters **123**, 102102 (2023).*

3.1 Introduction

SPEs in SiC are key components for quantum information technologies and sensing applications. These SPEs in SiC can be created using conventional semiconductor fabrication processes. Among the SPEs reported, SPEs at the SiO_2/SiC interface, which is the core of MOSFETs, are particularly attractive. This is because they exhibit strong room temperature emission [104, 108], their luminescence can be switched by applying voltage or injecting current [105, 108, 109], and they can be readily formed by low-cost thermal oxidation processes. Despite these advantages, several challenges still remain. The microscopic origin of the optically active defects (i.e., color centers) has not yet been clarified, hindering precise control over their optical properties. In particular, both the mechanisms governing the PL peak wavelengths [105] and the formation pathways of these defects remain elusive. Because the defect origin is not fully understood, control-

ling their density is also difficult. Such density control is crucial, as different quantum applications require different defect densities. For instance, a single NV center used as a quantum sensor provides high spatial resolution, whereas an ensemble of NV centers offers enhanced sensitivity [21]. In quantum computing and quantum information processing, long spin-coherence times are essential; therefore, parasitic spin or charge defects acting as decoherence sources must be eliminated. High-temperature processes, while often indispensable, pose additional challenges for precise defect control, as they can lead to the formation of multiple defect configurations and modify the local environment (e.g., strain fields and charge distributions).

This chapter elucidates the controllability and formation mechanisms of interface SPEs through a systematic investigation of their optical and electrical characteristics. The density of interface SPEs is known to be partially tunable by varying the oxidation temperature [104] and by conducting post-oxidation annealing in NO [106] or Ar [130] atmospheres. In the present study, high-temperature oxidation followed by post-oxidation annealing in a CO_2 ambient was employed to form the SiO_2/SiC structures. High-temperature oxidation is effective for forming SiO_2/SiC interfaces with reduced interface-state density [131], as also supported by DFT calculations [112]. To discuss the impact of oxidation conditions, the general oxidation reactions of SiC are expressed as follows:

(i) $\mathrm{SiC\,(s) + O_2(g) \longrightarrow SiO_2(s) + C\,(s)}$

(ii) $\mathrm{2\,SiC\,(s) + 3\,O_2(g) \longrightarrow 2\,SiO_2(s) + 2\,CO\,(g)}$

(iii) $\mathrm{SiC\,(s) + O_2(g) \longrightarrow SiO\,(g) + CO\,(g)}$

Chemical reactions (i) and (ii) represent the passive oxidation of SiC at relatively low and higher temperatures, respectively, where a solid SiO_2 layer is formed at the interface. Low-temperature oxidation forms an SiO_2 film but leaves residual carbon at the interface. This residual carbon degrades the carrier mobility in MOSFETs. Residual carbon at the interface has been experimentally confirmed [119, 132] and has also been discussed based on theoretical studies [83, 112, 133]. In contrast, the reaction shifts toward reaction (ii) as the oxidation temperature increases. In this pathway, SiC is consumed and carbon is released as carbon monoxide (CO) gas. A DFT calculation predicts that high-temperature oxidation accelerates the out-diffusion of residual carbon [112]. Therefore, high-temperature oxidation leads to the formation of interfaces that contain fewer carbon-related defect states.

Chemical reaction (iii) represents the so-called active oxidation regime, which occurs under conditions of high temperature and low oxygen partial pressure. In this regime, volatile species such as SiO and CO molecules are directly generated, preventing the formation of a stable SiO_2 layer. However, in the present study, thermal oxidation was carried out in 100% O_2 at atmospheric pressure, where oxygen is sufficiently supplied to maintain passive oxidation. Under these conditions, the contribution of active oxidation is considered negligible, and the oxidation process is dominated by the formation of a stable SiO_2/SiC interface [131].

Post-oxidation CO_2 annealing is also known to reduce the interface states and improve electron mobility of SiC MOSFETs [134]. DFT calculations also suggest that annealing in a CO_2 atmosphere can compensate for the V_O in oxide film, which is one of the possible candidates of oxide traps. This prediction is consistent with the experimentally observed reduction in the hysteresis of the C–V characteristics [134]. For these reasons, high-temperature oxidation and post-oxidation CO_2 annealing are expected to enable wide-range control of the density of interface SPEs.

3.2 Experiment

3.2.1 Sample Fabrication

Figure 3.1 depicts a schematic flow of the sample preparation and measurements. N-type 4H-SiC(0001) substrates with epi-layers ([N]: 1.0×10^{16} cm^{-3}) were employed in this chapter. Firstly, the substrates were cleaned by acetone with ultrasonic, 10% diluted HF solution, piranha acid (H_2SO_4 : H_2O_2 = 4 : 1), SC1 (NH_3 : H_2O_2 : Ultrapure Water (UPW) = 1 : 1 : 4) at 70°C, SC2 (HCl : H_2O_2 : UPW = 1 : 1 : 4) at 70°C, and 10% diluted HF. After wet cleaning, oxide films were formed by two methods: (i) oxidation in 100% oxygen (O_2) ambient, with temperatures ranging from 1200–1500°C, (ii) oxidation in 100% O_2 ambient at 1200°C and subsequent CO_2 annealing at temperatures ranging from 1050–1200°C for 30 minutes. The resulting oxide thickness ranged from 18 to 34 nm. The samples were also prepared under the same conditions, followed by aluminium (Al) evaporation to form the gate electrode and back contact to evaluate electrical characteristics.

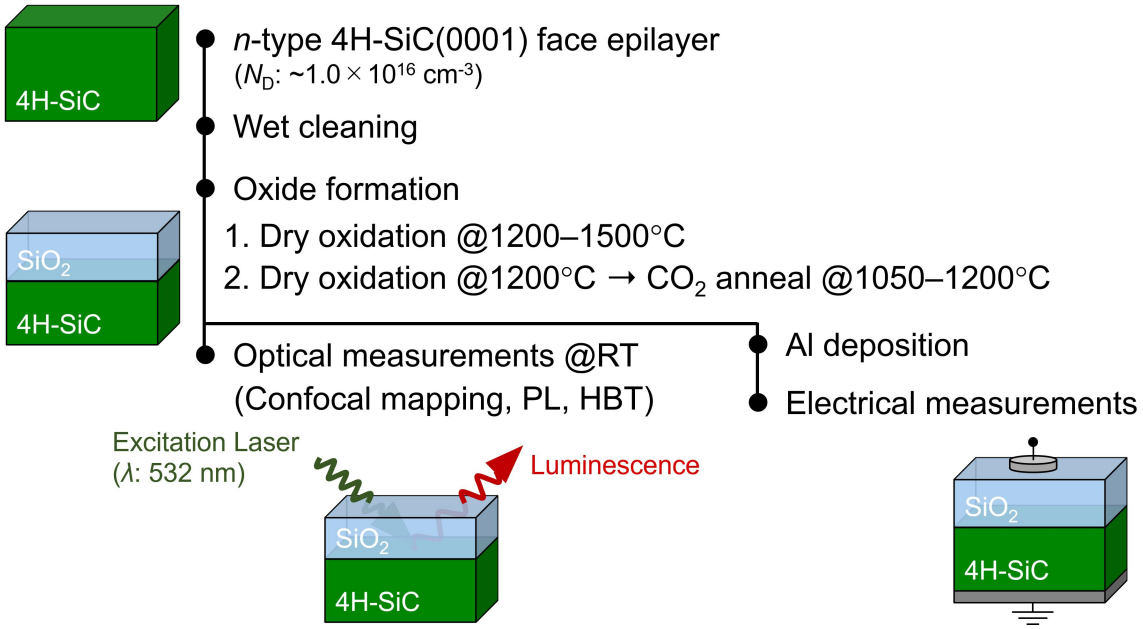

Figure 3.1. Flow of sample preparation and measurements.

3.2.2 Experimental Setup of Confocal Laser Scanning Microscopy

To evaluate the optical properties of the interface color centers, CLSM was used. The overall optical layout of the CLSM is shown in Fig. 2.1, and the following sections focus on the specific experimental components and measurement conditions used in the present chapter.

A home-built confocal optical system was used to characterize the color centers at the SiO_2/SiC interface. A 532 nm continuous-wave laser with an excitation power of 0.5 mW was reflected by a 550 nm long-pass dichroic mirror (cut-on at 45°) and focused onto the interface through a 60×, NA 0.9 objective lens (MPLAPON60X, Olympus). The objective lens was mounted on a three-axis piezo stage for raster scanning.

The PL emitted from the sample was collected by the same objective lens, transmitted through the dichroic mirror, and filtered using either a 550 nm or 600 nm long-pass filter depending on the measurement. The filtered signal was directed either to a Czerny–Turner spectrometer (HRS-300, Teledyne Princeton Instruments) equipped with a back-illuminated deep-depletion CCD (Pixis100BRX) or, after passing through a 50:50 non-polarizing beam splitter, to two avalanche photodiode single-photon counting modules (SPCM-AQRH-14, Excelitas Technologies). Photon arrival times were recorded using a

TDC (MCS8A, FAST ComTec) for HBT measurements [126]. A flip mirror allowed rapid switching between spectral acquisition and correlation measurements.

The luminescence properties were evaluated using three complementary approaches:

(i) Confocal PL mapping, performed by raster-scanning the objective lens. Emission above 600 nm was collected to suppress first- and second-order Raman scattering, with the focal plane fixed at the SiO_2/SiC interface.

(ii) PL spectroscopy, using the spectrometer to acquire emission spectra above 550 nm.

(iii) HBT measurements of the second-order autocorrelation function $g^{(2)}(\tau)$, where τ is the detection time delay between the two APDs.

Instrument control and data acquisition were performed using the MAHOS framework [135], and all measurements were conducted at room temperature.

3.2.3 Analysis of Electrically Active Defects

To identify the origin of the SiO_2/SiC interface defects that act as SPEs, the density of electrically active defects was evaluated using C–V measurements. A schematic of the measurement setup is illustrated in Fig. 3.2. Capacitance was measured while sweeping the gate voltage using a manual probe station (MX-1100B, Vector) and a semiconductor

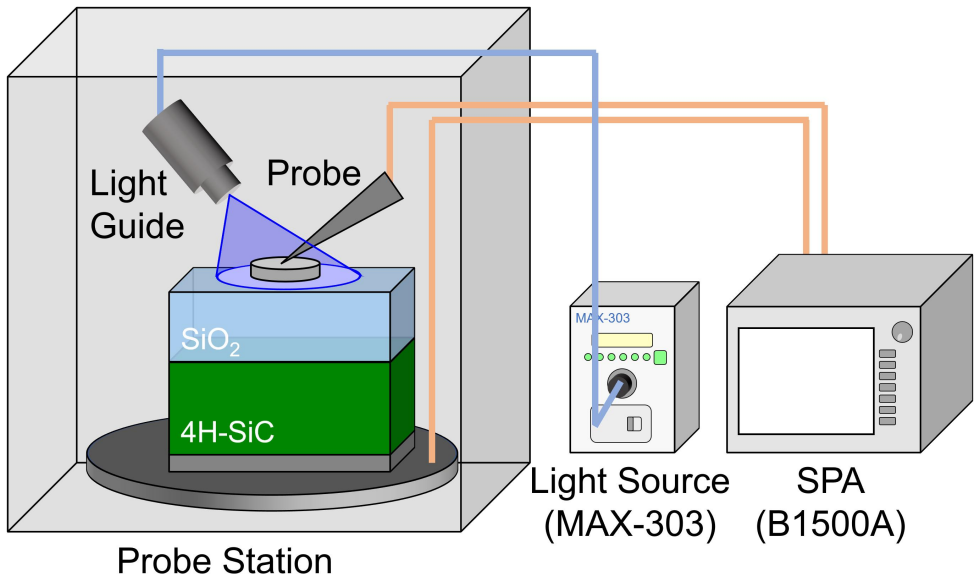

Figure 3.2. A schematic diagram of the electrical measurement setup.

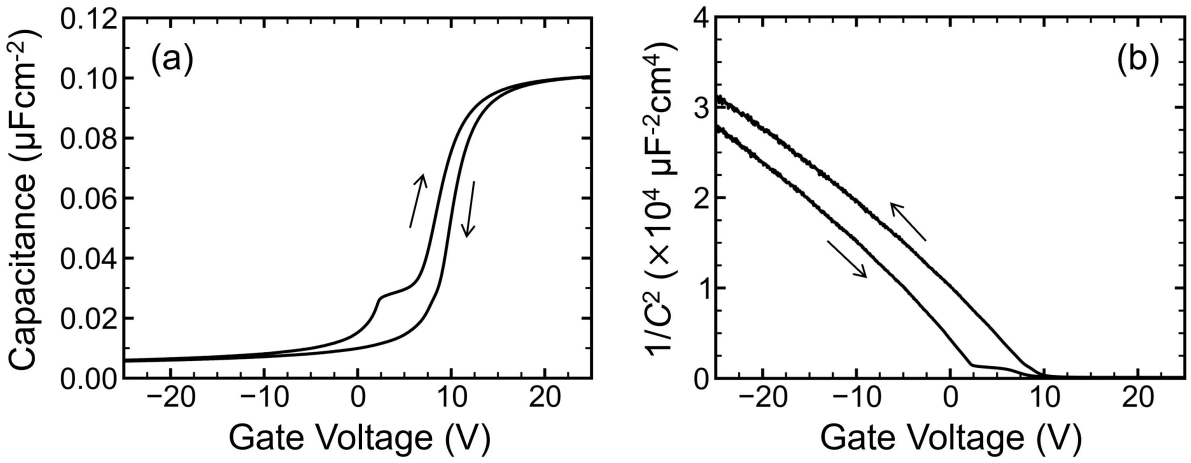

Figure 3.3. (a) Typical bidirectional C–V and (b) $1/C^2$–V characteristics of a SiC MOS capacitor measured at 1 MHz over a voltage range of −25 V to 25 V.

parameter analyzer (SPA)(B1500A, Keysight). Figures 3.3 (a) and (b) present representative bidirectional C–V and $1/C^2$–V characteristics for the as-oxidized sample measured at 1 MHz. In the absence of interface and oxide traps, the flatband voltage (V_{FB}) corresponds to the work-function difference between the Al gate and the n-type 4H-SiC substrate, i.e., $V_{\mathrm{FB,\ Ideal}} = 0.2$ V. In practice, the actual V_{FB} is shifted by electron trapping and fixed charges and the magnitude of V_{FB} shift is proportional to the density of effective fixed charges at the interface (V_{Eff}). The backward sweep generally shifts from the forward sweep, exhibiting hysteresis (V_{Hys}), which arises from charge trapping in near-interface oxide traps during the initial sweep.

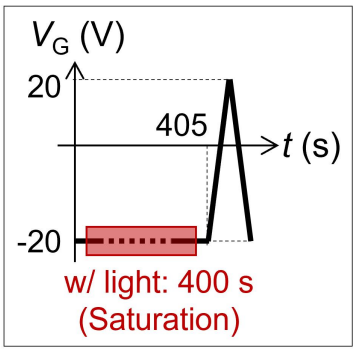

Figure 3.4. Flow of the photo-assisted C–V measurements.

As shown in Fig. 3.6, the quantity extracted as N_{Eff} corresponds to energetically deep interface states. Because the C–V measurements were performed at a high probing

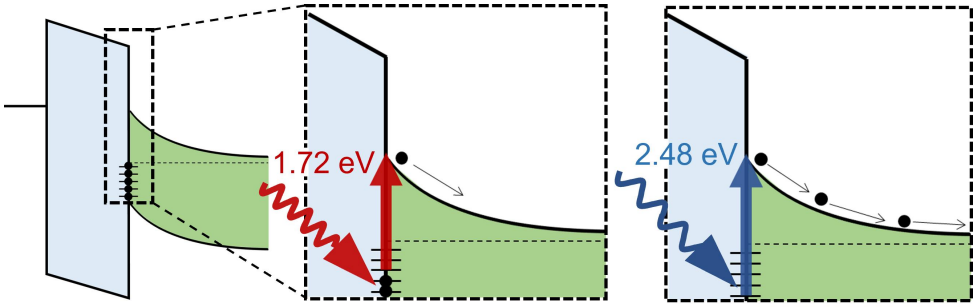

Figure 3.5. Explanation of the photo-assisted C–V measurements.

frequency of 1 MHz, fast interface states located near the conduction band edge cannot respond to the AC signal. Therefore, only the deeply located traps that manifest as a V_{FB} shift are evaluated through N_{Eff}.

A quantity N_{Hys} represents the density of near-interface oxide traps, as depicted in Fig. 3.6. These traps are initially empty, but become filled once the device is driven into accumulation, where electrons can tunnel into the oxide. Consequently, the difference between the forward and backward C–V sweeps quantifies the amount of charge stored in these oxide traps.

To evaluate the defect states located below the midgap energy level, the photo-assisted C–V measurements were also conducted using a xenon lamp (MAX-303, Asahi Spectra) equipped with a BPF. A BPF with center wavelength of either 540 nm (2.48 eV) or 720 nm (1.72 eV) was used in this study, having a bandwidth of approximately 10 nm. The flow of photo-assisted C–V measurement is summarized in Fig. 3.4. As shown in Fig. 3.4, a continuous bias of -20V was applied under light illumination in the deep depletion state until saturation of V_{FB} shift. The mechanisms of photo-assisted C–V measurements are illustrated in Fig. 3.5. During illumination, electrons are first emitted from deep-trap states. Then, excited electrons immediately drift toward the bulk along the depletion-layer electric field owing to applying negative voltage. After the light is turned off, gate voltage was swept to accumulation states, which allows the contribution of these deep-level traps to be characterized.

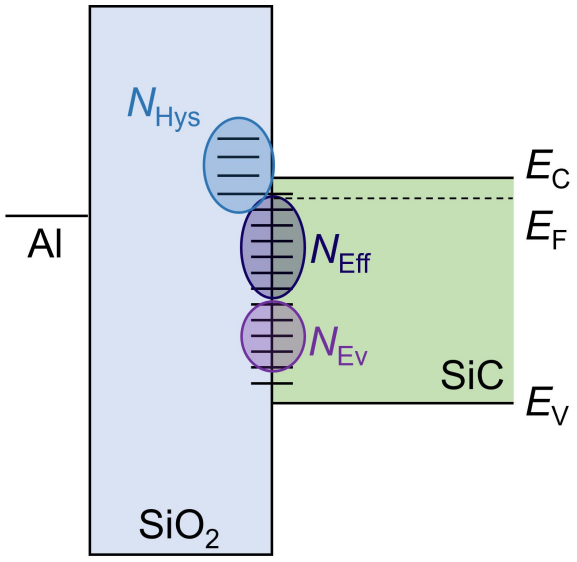

Figure 3.6. Schematic illustration of energy distribution of the defects evaluated in this study.

The following equations were used to evaluate each metric, as depicted in Fig. 3.6. Here, (C_{OX}) is the oxide capacitance.

(i) Effective fixed charge: $N_{Eff} = C_{OX}\left(V_{FB,\ Measured} - V_{FB,\ Ideal}\right)$

(ii) Oxide traps: $N_{Hys} = C_{OX}\left(V_{FB,\ Backward} - V_{FB,\ Forward}\right)$

(iii) Interface traps below midgap energy level: $N_{E_V} = C_{OX}\left(V_{FB,\ 1.72\ eV} - V_{FB,\ 2.48\ eV}\right)$

3.3 Density Control of Interface SPEs

Tuning the areal density of SPEs from ensemble-level to spatially isolated defects enables a wide variety of applications. Ensemble states are advantageous for high-sensitivity quantum sensing, whereas isolated SPEs are essential for quantum information processing. In this section, the color center density at the SiO_2/SiC interface was systematically controlled by varying the oxidation and post-oxidation CO_2 annealing conditions.

The samples investigated in this chapter were SiO_2/SiC structures fabricated by thermal oxidation at 1200–1500°C, and post-oxidation CO_2 annealing was carried out at 1050–1200°C for 30 min.

Confocal PL mapping was conducted using a 532 nm excitation laser focused through an NA = 0.9 objective. The excitation power (P = 0.5 mW), scan area (30 µm ×

30 µm), and pixel step (300 × 300) were fixed for all samples to ensure quantitative comparison of color center density. In the PL mapping images, diffraction-limited bright spots and spatially broad background luminescence were identified. Only bright spots with intensities exceeding 50 kcps were counted as individual color centers.

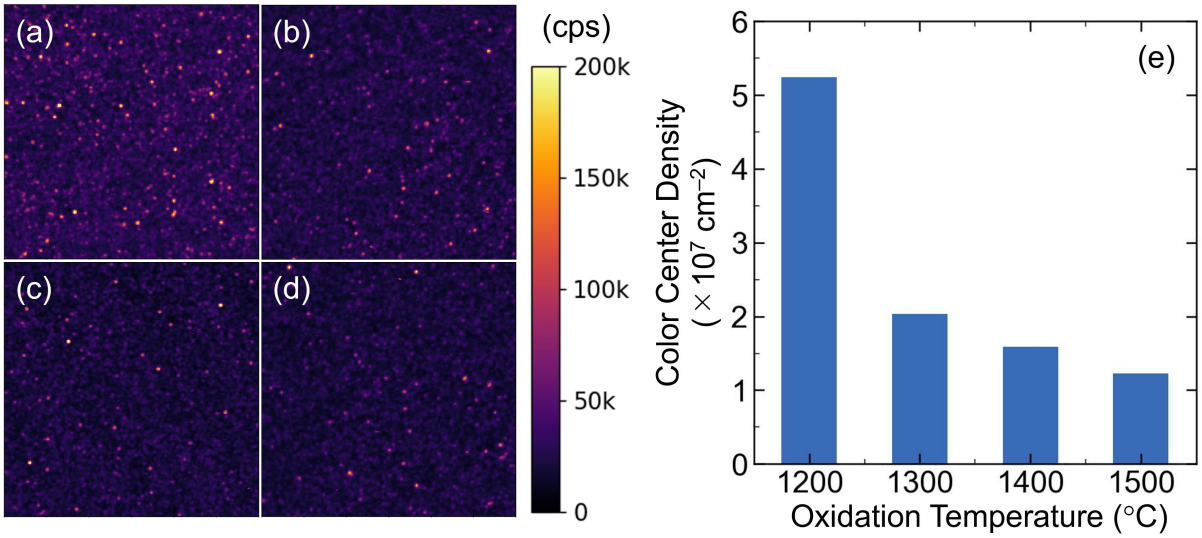

Figure 3.7. Confocal PL mapping images (30 µm × 30 µm) of samples oxidized at (a) 1200°C, (b) 1300°C, (c) 1400°C, and 1500°C, respectively. (e) Extracted bright spot density as a function of oxidation temperature.

High-temperature oxidation was first examined as a method for density reduction. Figures 3.7 (a)–(d) show typical PL mapping images of samples oxidized at temperatures from 1200 to 1500°C. The sample oxidized at 1200°C exhibits a high density of bright spots together with strong background luminescence. Both the bright spot density and background level monotonically decrease with increasing oxidation temperature. The extracted densities, normalized to a 30 µm × 30 µm area, were 5.2×10^7, 2.0×10^7, 1.6×10^7, and 1.2×10^7 cm^{-2} for oxidation at 1200, 1300, 1400, and 1500°C, respectively (Fig. 3.7 (e)). These results are consistent with previous reports that higher oxidation temperatures enhance carbon desorption from the interface, thereby suppressing carbon-related defect formation [112]. Nevertheless, even at 1500°C, the density remains on the order of 10^7 cm^{-2}.

Figures 3.8 (a)–(d) show PL mapping images of samples subjected to post-oxidation CO_2 annealing at 1050–1200°C. Compared with the as-oxidized sample (Fig. 3.7 (a)), all CO_2-annealed samples exhibit substantially fewer bright spots and a reduced back-

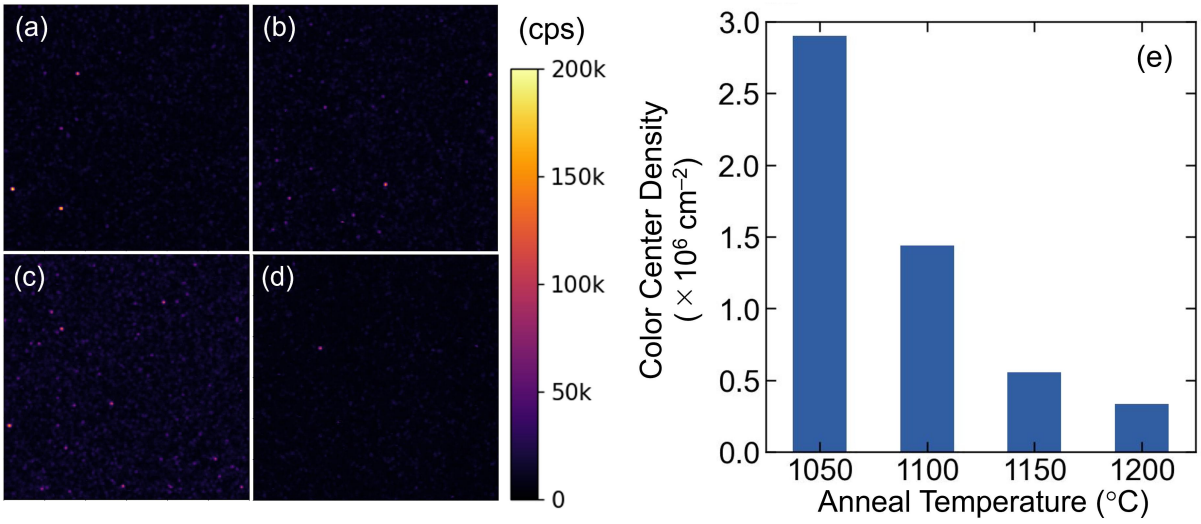

Figure 3.8. Confocal PL mapping images (30 µm × 30 µm) of samples annealed in CO_2 (a) 1050°C, (b) 1100°C, (c) 1150°C, and 1200°C, respectively. (e) Extracted bright spot density as a function of CO_2 annealing temperature.

ground. The densities extracted from the images were 2.9×10^6, 1.4×10^6, 5.6×10^5, and 3.3×10^5 cm^{-2} for annealing at 1050, 1100, 1150, and 1200°C, respectively, showing a strong monotonic decrease. This trend agrees well with earlier studies reporting that CO_2 annealing effectively reduces interface-state densities in MOS structures [134]. At the highest annealing temperature of 1200°C, the bright spot density approaches the detection limit of the confocal setup (1.1×10^5 cm^{-2}).

These results demonstrate that the color center density at the SiO_2/SiC interface can be tuned over more than two orders of magnitude, from 10^7 down to 10^5 cm^{-2}, simply by adjusting the oxidation and CO_2 annealing conditions.

3.4 Optical Properties of Interface SPEs

The optical characteristics of interface SPEs were evaluated through PL spectroscopy and HBT measurements. The PL spectral shape, intensity, and peak position reflect the local microscopic environment of the defect, including strain, charge distribution, and external fields, while the second-order autocorrelation function $g^{(2)}(\tau)$ reveals the single-photon nature. This section presents the PL and HBT measurement results for oxidized and CO_2-annealed samples, and discusses the impact of these processes on the optical properties of the interface SPEs.

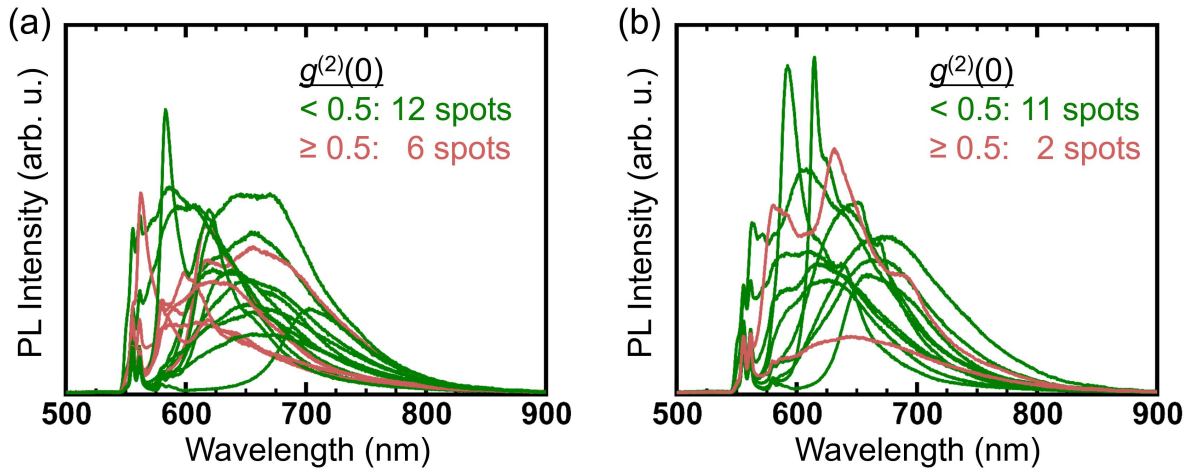

Figure 3.9. PL spectra obtained from (a) Ox. 1200°C and (b) Ox. 1500°C samples. Green and red traces correspond to color centers exhibiting $g^{(2)}(0) < 0.5$ and > 0.5, respectively.

Figures 3.9 (a) and (b) show representative PL spectra from the samples oxidized at 1200°C and 1500°C. All spectra were obtained under 0.5 mW excitation at room temperature. Considerable variation in intensity and peak wavelength is observed among individual color centers, consistent with earlier reports on interface-related color centers [105, 108].

Figures 3.10 and 3.11 summarize representative $g^{(2)}(\tau)$ from both samples. For the Ox. 1200°C sample, HBT measurements were performed on 18 diffraction-limited centers. All color centers exhibited anti-bunching behavior, yet only 12 showed $g^{(2)}(0) < 0.5$, indicating that several bright spots were affected by background contributions or multi-SPEs overlap. Similarly, in the Ox. 1500°C sample, 11 out of 13 color centers satisfied $g^{(2)}(0) < 0.5$.

Although the fraction of true SPEs improved from 66.7% at 1200°C to 84.6% at 1500°C, many bright spots still failed to satisfy the single-photon characteristic. These results demonstrate that high-temperature oxidation alone is insufficient to reliably form optically isolated SPEs, due to the presence of multiple defect species.

Figure 3.12 shows PL spectra from color centers in the + CO_2 1200°C sample. Compared with the as-oxidized samples, the spectral variation—particularly peak position and overall shape—was significantly reduced, suggesting suppression of spectral diffusion and reduction of defect species diversity. Figure 3.13 shows representative $g^{(2)}(\tau)$ measured

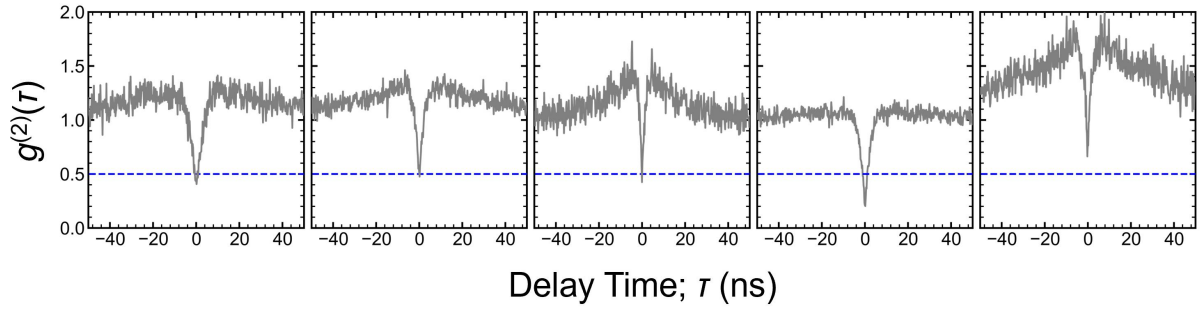

Figure 3.10. Representative second-order autocorrelation functions $g^{(2)}(\tau)$ for color centers in the Ox. 1200°C sample.

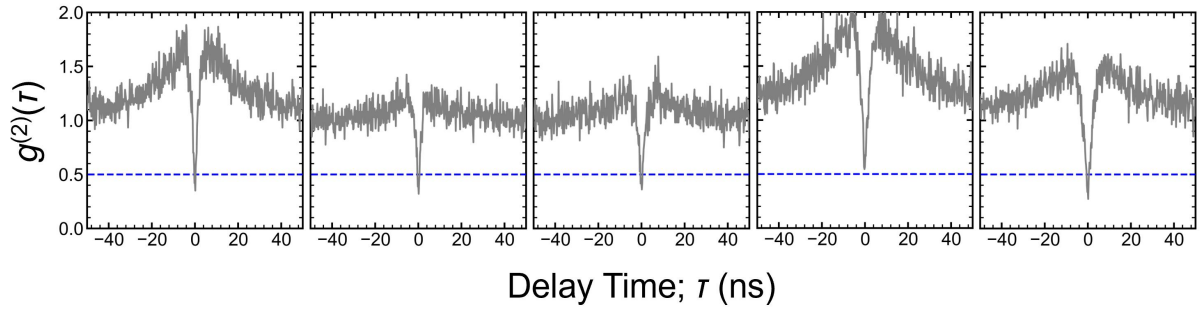

Figure 3.11. Representative second-order autocorrelation functions $g^{(2)}(\tau)$ for color centers in the Ox. 1500°C sample.

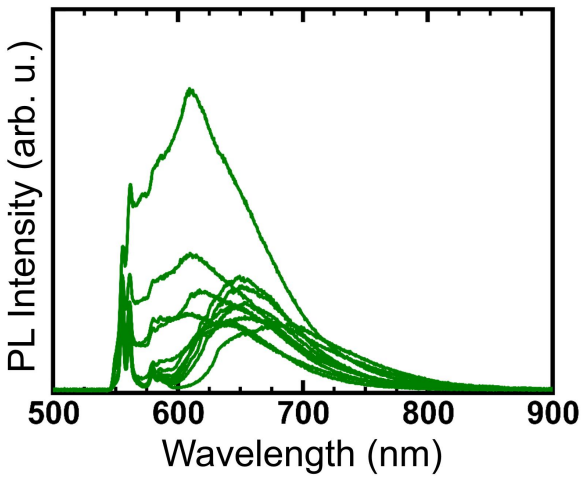

Figure 3.12. PL spectra obtained for color centers in the $+CO_2$ 1200°C sample. All measured color centers exhibited $g^{(2)}(0) < 0.5$.

from 11 diffraction-limited centers. All color centers satisfied $g^{(2)}(0) < 0.5$, demonstrating consistent single-photon emission across the sample.

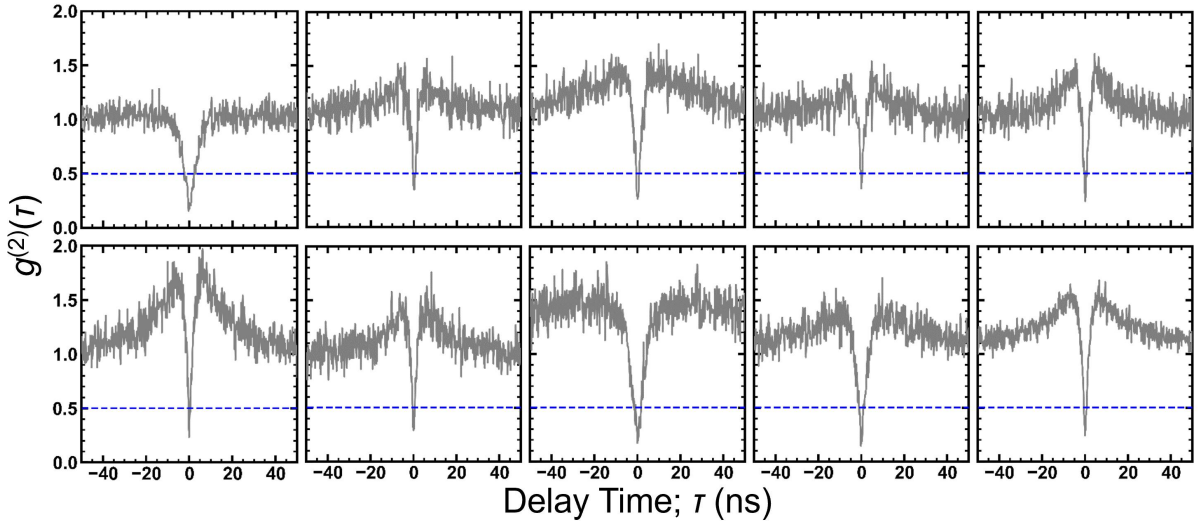

Figure 3.13. Representative $g^{(2)}(\tau)$ for color centers in the $+CO_2$ 1200°C sample. All color centers exhibit clear anti-bunching with $g^{(2)}(0) < 0.5$.

These results indicate that post-oxidation CO_2 annealing is highly effective not only in reducing the areal density of interface color centers, but also in improving the homogeneity of PL spectra and purity of the remaining color centers. This improvement is consistent with earlier reports showing that CO_2 annealing reduces electrically active interface defects and mitigates local strain and charge fluctuations [134]. Consequently, CO_2 annealing emerges as a key step in the controlled formation of spatially isolated and optically stable SPEs at the SiO_2/SiC interface.

3.5 Electrical Properties of MOS Capacitors

To give a clue to the physical origin of the SPEs, investigating the electrically active defects at the SiO_2/SiC interface is effective. For electrical measurements, MOS capacitors were fabricated under the same oxidation and annealing conditions were evaluated using both conventional and photo-assisted C–V measurements. Detailed analysis methods were described in Section 3.2.3. This section presents the electrically active defects at the interface, including the effective fixed charges, near-interface oxide traps, and interface traps located below the midgap energy level. Figure 3.14 shows representative high-frequency (1 MHz) C–V characteristics measured for MOS capacitors oxidized at 1200°C and those followed by CO_2 annealing at 1200°C. The capacitance values were normalized by the C_{OX}. For the as-oxidized sample, the C–V curves display a pronounced stretch-out

and hysteresis, indicating significant charge trapping into interface states. In the absence of interface and oxide traps (i.e., ideal interface), V_{FB} corresponds to the work-function difference between the Al gate and the n-type 4H-SiC substrate, i.e., $V_{FB,\ Ideal} = 0.2$ V (see dotted line in Fig. 3.14). However, the measured V_{FB} for the as-oxidized sample shifts positively, suggesting the presence of deep acceptor-type defects (electron traps) at the interface. Post-oxidation CO_2 annealing mitigated the offset of V_{FB}, reducing the N_{Eff}. The hysteresis observed in the bidirectional C–V sweeps of as-oxidized sample arises from electron trapping into near-interface oxide traps. However, this hysteresis disappeared after CO_2 annealing, indicating that CO_2 annealing can effectively suppress near-interface oxide traps.

Figures 3.15 (a) and (b) show the representative photo-assisted C–V characteristics, obtained from (a) Ox. 1200°C and 1500°C samples, respectively. As the photon energy was increased from 1.72 to 2.48 eV, the magnitude of the V_{FB} shift increased. This behavior arises because photo-assisted C–V measurements selectively empty trap states whose ionization energies are smaller than the incident photon energy. Photons with an energy of 1.72 eV can only excite electrons from interface traps closer to conduction-band minimum (E_C), whereas photons with an energy of 2.48 eV can additionally excite electrons from deeper traps located further below E_C. Once these electrons are photo-

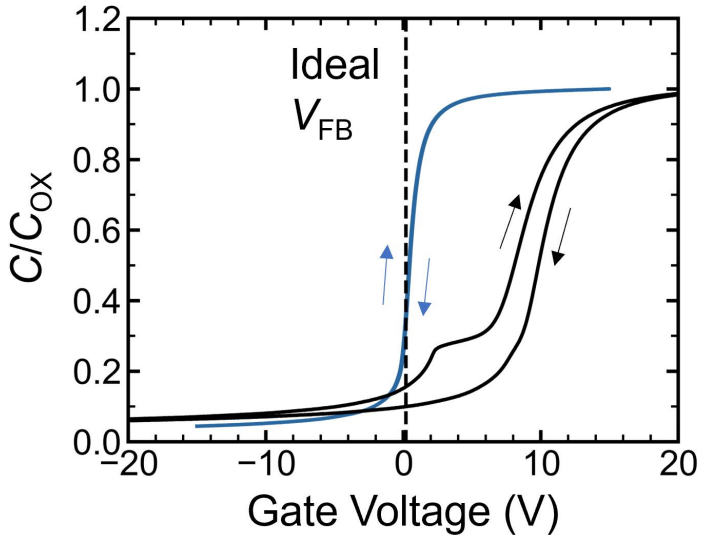

Figure 3.14. Bidirectional C–V characteristics measured at 1 MHz. The black line corresponds to the Ox. 1200°C sample, and the blue line corresponds to the +CO_2 1200°C sample.

emitted, they drift toward the SiC bulk under the negative gate bias, leaving behind positively charged empty traps. These positively charged centers shift the measured flatband voltage in the negative direction. Therefore, the increase in V_{FB} with photons directly reflects the presence of deeper interface traps at a given energy range. The amount of charge released from such deep traps is hereafter denoted as $N_{\mathrm{E_V}}$.

Figure 3.16 summarizes the temperature dependence of the three extracted charge

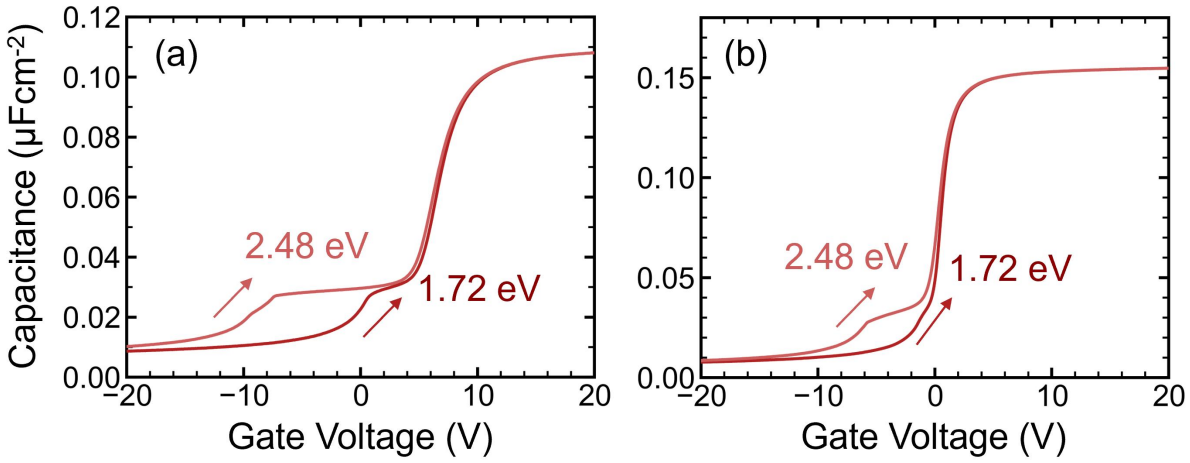

Figure 3.15. Photo-assisted C–V characteristics measured at 1 MHz for the samples of (a) Ox. 1200°C and (b) +CO_2 1200°C. The gate voltage was swept from depletion to accumulation.

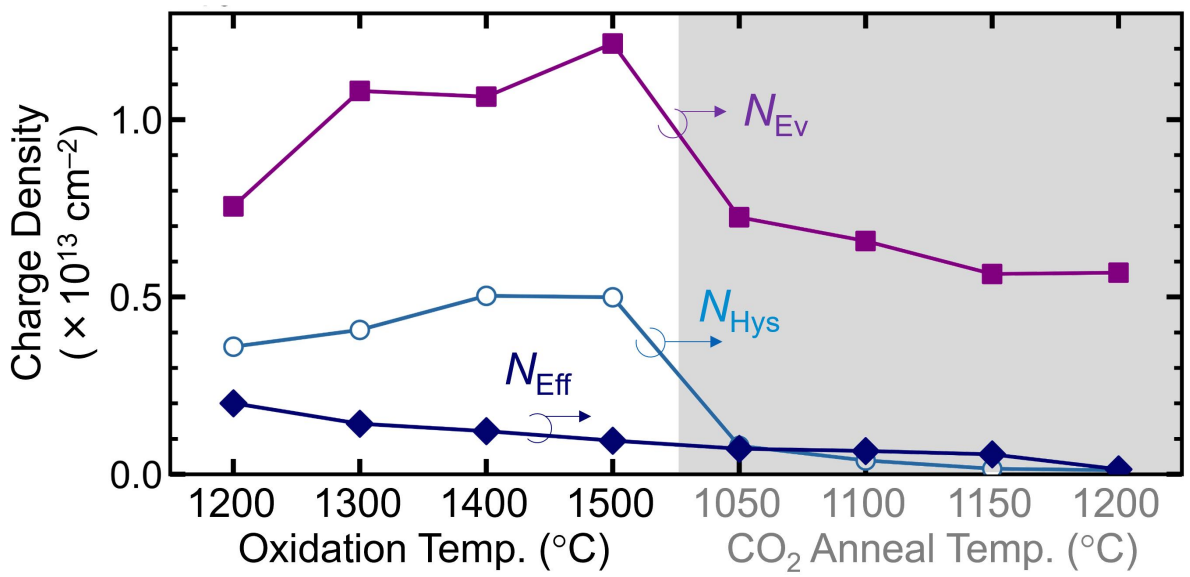

Figure 3.16. N_{Hys}, N_{Eff}, and $N_{\mathrm{E_V}}$ plotted against the sample annealing conditions.

densities, N_{Eff}, N_{Hys}, and $N_{\mathrm{E_V}}$, as a function of oxidation and CO_2 annealing temperature. The effective charge density N_{Eff} decreases monotonically with increasing oxidation temperature and further decreases after CO_2 annealing. In contrast, the density of oxide traps N_{Hys} exhibits a different trend. During oxidation, N_{Hys} slightly increases with temperature, whereas a pronounced reduction is observed after CO_2 annealing, followed by a monotonic decrease with increasing CO_2 annealing temperature. Notably, after annealing above 1150°C in CO_2 atmosphere, N_{Hys} becomes smaller than N_{Eff}, implying that most oxide-trapped charges are effectively passivated. This strong suppression of N_{Hys} is consistent with DFT based predictions that CO_2 annealing compensates V_{O} in the oxide films [136], thereby passivating oxide traps and improving the interface stability [134].

The integrated density of interface states located below the midgap energy level, i.e. $N_{\mathrm{E_V}}$, is intrinsically several times higher than the other two components. It increases with oxidation temperature, but decreases upon CO_2 annealing and continues to decrease slightly with further temperature rise. This decrease suggests that CO_2 annealing at elevated temperatures is partially effective in the removal of interface states located below the midgap energy level likely through the oxidation and desorption of residual carbon species at the interface.

Overall, the distinct temperature dependences of N_{Eff}, N_{Hys}, and $N_{\mathrm{E_V}}$ demonstrate that post-oxidation CO_2 annealing plays a critical role in both passivating oxide traps and eliminating interface states, thereby significantly improving the electrical properties of the SiO_2/SiC interface.

3.6 Correlation Between Optical and Electrical Metrics

To clarify the microscopic origin of the interface SPEs, the density of color centers was compared with the densities of electrically active defects extracted from conventional C–V and photo-assisted C–V measurements.

Figure 3.17 compares these three charge densities with the color center density obtained from confocal PL mapping for all oxidation and CO_2 annealing conditions. The bar graph (left axis) shows the areal density of color centers at the SiO_2/SiC interface, while the solid lines (right axis) represent N_{Hys}, N_{Eff}, and $\times 1/4 N_{\mathrm{E_V}}$ as functions of oxidation or annealing temperature. For the oxidation series (1200–1500°C), the color center

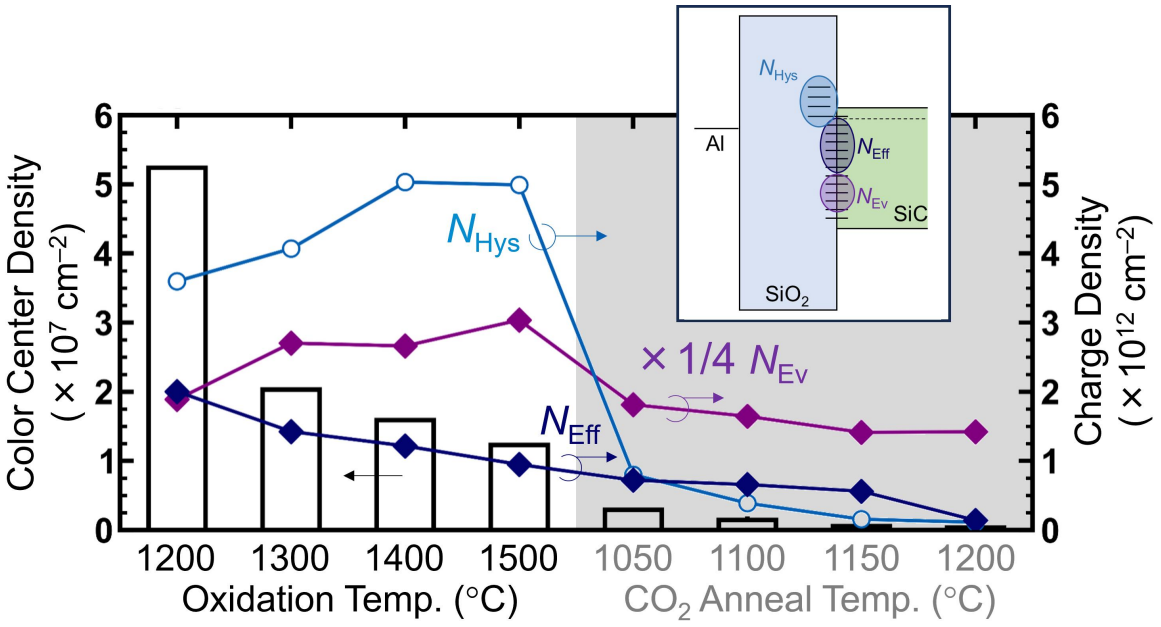

Figure 3.17. Color center density plotted against the measured sample conditions with N_{Hys}, N_{Eff}, and $N_{\mathrm{E_V}}$ at the same time. The inset figure represents a schematic illustration of the defects evaluated in this study.

density decreases monotonically with increasing temperature, and this trend closely follows the reduction of N_{Eff}. In contrast, N_{Hys} exhibits a non-monotonic behavior with a maximum around 1400°C, and $N_{\mathrm{E_V}}$ remains relatively high even when the color center density is strongly suppressed. A similar tendency is observed in the CO_2-annealed sample series: as the annealing temperature increases from 1050 to 1200°C, both the color center density and N_{Eff} decrease toward the detection limit, whereas N_{Hys} and $N_{\mathrm{E_V}}$ show weaker or different temperature dependences.

These correlations indicate that the density of interface color centers is most strongly correlated with N_{Eff}, rather than with N_{Hys} or $N_{\mathrm{E_V}}$. Since N_{Eff} reflects deep acceptor-type states at the interface, this result suggests that the dominant SPEs originate from defect configurations that introduce such deep acceptor levels. A detailed discussion of the microscopic origin of the interface SPEs is presented in Section 5.4.

3.7 Summary

The density of color centers was successfully tuned over a wide range from the order of 10^5 to 10^7 cm^{-2} and spatially well-isolated color centers—separated by more than the

diffraction-limited resolution and not influenced by nearby dim centers—were formed at the interface by high-temperature oxidation and/or CO_2 annealing. In particular, post-oxidation CO_2 annealing has a strong capability to generate such isolated SPEs by passivating dim centers and reducing background luminescence. The detailed contribution of CO_2 annealing to these improvements is further investigated in Chapter 4. Furthermore, the correlation between the densities of electrically and optically active defects was examined to clarify the physical origin of the interface SPEs. Among the three evaluated charge densities—oxide traps, effective fixed charges, and interface states below the SiC midgap energy level—the density of effective fixed charges showed the strongest correlation with the color-center density. This result suggests that the interface SPEs originate from defects that introduce deep acceptor-type states at the interface.

Chapter 4

Design of Annealing Conditions for the Formation of Spatially Separated Single Photon Emitters at SiO_2/SiC Interfaces

This chapter is primarily based on the following publication:
T. Nakanuma et al., "Design of annealing conditions for the generation of isolated single-photon emitters at SiO_2/SiC interfaces," Journal of Applied Physics ***137****, 205702 (2025).*

4.1 Introduction

While Chapter 1 provided the overall background of SPEs in SiC and their potential for quantum technologies, this chapter focuses on the role of post-oxidation processes in determining the optical and electrical properties of the SiO_2/SiC interface. Since the interface environment strongly affects the charge state and stability of the interface SPEs, understanding their behavior under thermal processing is essential for achieving reliable single-photon emission.

Despite their strong potential, interface SPEs still face challenges related to their unknown microscopic origin and the lack of a reliable formation strategy, which Chapter 3 addressed by examining a wide range of oxidation and post-oxidation annealing conditions and correlating the density of interface color centers with electrically active defects,

such as fixed charges and interface states. The former chapter demonstrated that CO_2 annealing enables control of the color center density over the range of 10^5 to 10^7 cm^{-2}. Moreover, it was found that, after CO_2 annealing at appropriate temperatures, essentially all observed color centers exhibited single-photon characteristics. Nevertheless, the microscopic mechanism responsible for this selective formation of SPEs has not yet been fully clarified.

Motivated by these findings, the present chapter shifts from the broad process survey of Chapter 3 to a refined investigation under optimized thermal conditions. The oxidation and post-oxidation annealing temperatures are fixed at 1200°C, identified in Chapter 3 as a favorable condition for forming interface SPEs, and the anneal duration is used as the primary control parameter. A systematic comparison of CO_2 annealing with Ar annealing was performed at the same temperature and durations. This evaluation makes it possible to distinguish the influence of CO_2 molecules from pure thermal effects. This enables a detailed examination of the evolution of the color center density, integrated PL intensity, and single-photon characteristics as a function of anneal time. Furthermore, because both CO_2 and Ar ambients avoid the introduction of foreign atoms other than Si, C, and O, the discussion can focus on intrinsic defect reactions at the SiO_2/SiC interface. Through this analysis, this chapter establishes a universal and process-compatible design strategy for forming interface SPEs, providing practical guidelines for integrating these emitters into future SiC-based quantum photonic and electronic devices.

4.2 Experiments

4.2.1 Flow of Sample Preparation and Measurements

Figure 4.1 illustrates the experimental procedures and measurements flow in this study. *N*-type 4H-SiC(0001) substrates with an epitaxial layer ([N]: 1.0×10^{16} cm^{-3}) were cleaned by the following wet process. The cleaning sequence consisted of acetone with ultrasonic agitation, a 10% HF solution, piranha solution, and SC1 and SC2 at 70°C, followed by a final 10% HF dip. Subsequently, thermal oxidation was carried out at 1300°C to form an approximately 30 nm SiO_2 film. Post-oxidation annealing in CO_2 or Ar was performed at 1200°C for durations ranging from 1 to 120 min. For comparison, an as-oxidized sample without post-annealing was also prepared. For these SiO_2/SiC structures, a series of optical measurements, including confocal PL mapping and HBT measurement, was

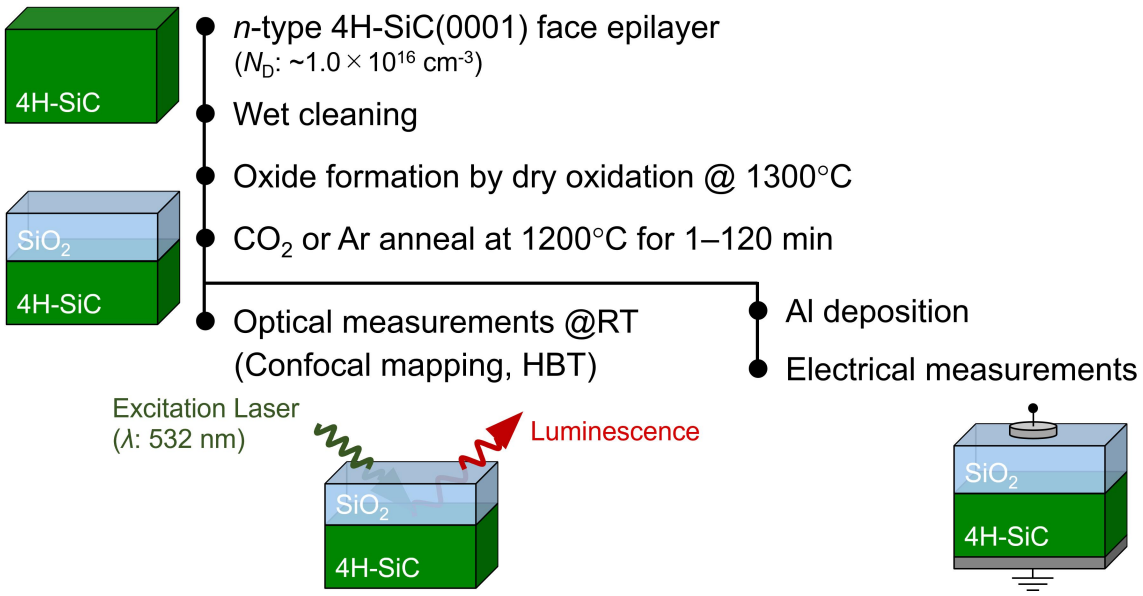

Figure 4.1. Flow of sample preparation and measurements.

conducted at room temperature. Furthermore, MOS capacitors with an Al gate electrode and a backside contact were fabricated to evaluate the electrical characteristics.

4.2.2 Experimental Setup of Confocal Laser Scanning Microscopy

Continuing from Chapter 3, this chapter also investigates SPEs at the SiO_2/SiC interfaces. The optical measurements in this chapter were performed using the CLSM shown in Fig. 2.1, which was described in Chapter 2. An excitation laser with a wavelength of 532 nm was reflected by a dichroic mirror (550 nm cut-on) and focused onto the SiO_2/SiC interface using an objective lens with NA = 0.9, 60× (MPLAPON60X, Olympus) mounted on a piezoelectric stage. The resulting PL was collected through the same objective lens, transmitted through the dichroic mirror and a 600-nm long-pass filter, and passed through a confocal pinhole before reaching the measurement instrument. The detection system can be switched between two functionalities using a movable mirror: (i) PL spectral measurement with a back-illuminated, deep-depletion CCD camera (DU920P-BR-DD, Oxford Instruments) connected to a spectrometer (SR500i, Oxford Instruments), and (ii) photon correlation measurement using two single-photon counting modules (COUNT-100T, Laser Components) connected to a time-to-digital converter (MCS8A, FAST ComTec).

In this study, the latter configuration was mainly used to count photons and evaluate the second-order correlation function $g^{(2)}(\tau)$. The excitation laser power was set to 1.0 mW for PL mapping and 0.5 mW for HBT measurements. All optical elements and signal acquisitions were controlled by the MAHOS software framework [137].

4.3 Confocal Mapping Images of Interface SPEs

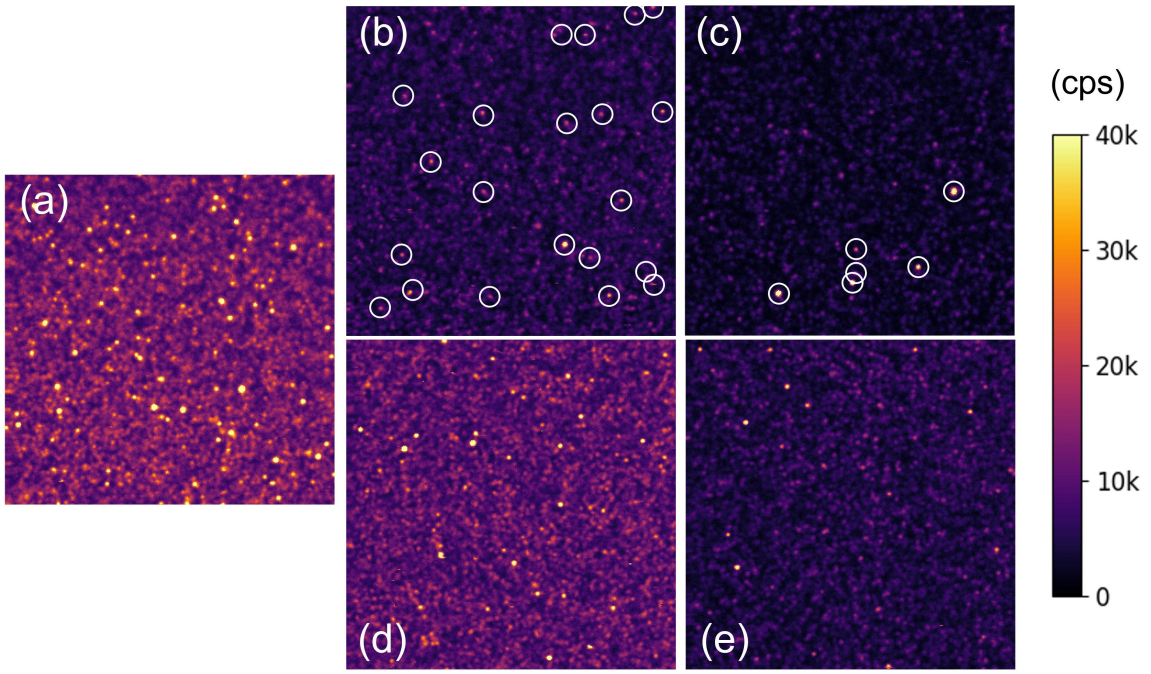

Figure 4.2. Representative PL mapping images obtained from (a) as-ox., (b) $+CO_2$ 5 min, (c) $+CO_2$ 30 min, (d) +Ar 5 min and (e) +Ar 30min. White circles in (b) and (c) indicate the bright spots whose intensities exceed 20 kcps. The mapping area was 30×30 μm^2.

This section investigates the dependence of color center densities on either CO_2 or Ar anneal duration. Confocal PL mapping images were acquired by scanning across the x–y plane of the sample interface. The number of bright spots was then counted to evaluate their areal density.

Figure 4.2 shows representative confocal mapping images obtained from (a) as-ox., (b) $+CO_2$ 5 min, (c) $+CO_2$ 30 min, (d) +Ar 5 min, and (e) +Ar 30 min samples. As shown in Fig. 4.2 (a), as-ox. sample exhibits numerous bright spots and a high background luminescence. Post-oxidation CO_2 anneal was remarkably effective in reducing both quantities,

even after only 5 min of annealing (Fig. 4.2 (b)). With prolonged CO_2 anneal of 30 min, both the number of bright spots and the background intensity further decreased (Fig. 4.2 (c)). Therefore, CO_2 annealing is highly effective for controlling both bright spot density and background luminescence, consistent with Chapter 3. Similarly, Ar anneal also reduced both quantities, albeit remained higher for Ar anneal for 5 min than for CO_2 for 5 min (Figs. 4.2 (b) and (d)). The same trend was observed at comparison between them after annealing of 30 min (Figs. 4.2 (c) and (e)). For quantitative analysis, the integrated

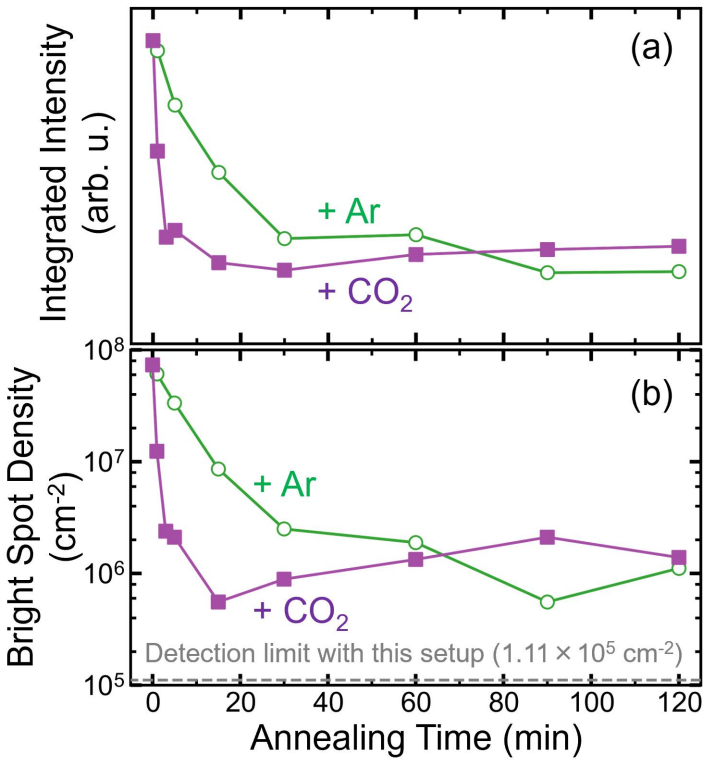

Figure 4.3. (a) The integrated intensity (linear scale) and (b) the bright spot density (log scale) as a function of anneal durations. Green or purple plot indicates the results of CO_2 or Ar anneal.

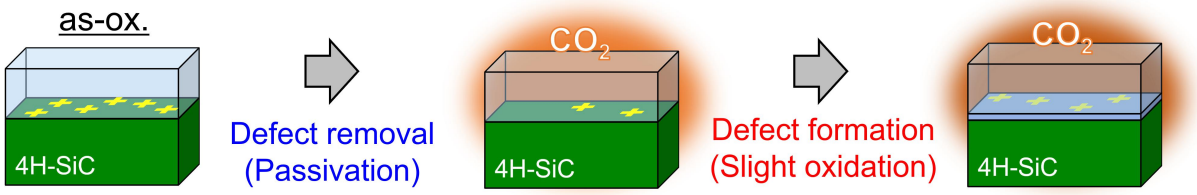

Figure 4.4. Schematic illustrations of the time evolution during CO_2 annealing of the SiO_2/SiC structure. Yellow crosses illustrate the defects at the SiO_2/SiC interfaces.

intensity and the bright spot density were evaluated. The integrated intensity was defined as the total photon counts summed over all pixels. The bright spot density was determined by thresholding the intensity of 20 kcps using the image processing technique. The results are plotted as a function of anneal duration in Figs. 4.3 (a) and (b). Annealing shorter than 30 min at either atmosphere led to a decrease in the integrated intensity. In particular, the decrease was faster for CO_2 anneal than that for Ar anneal, such that the integrated intensity after 30 min of CO_2 anneal already reached 3.29×10^5 cm^{-2}, which is approximately the same as that after 90 min of Ar anneal 3.18×10^5 cm^{-2}. However, after longer durations of CO_2 annealing, the integrated intensity showed a slight increase. This suggests that CO_2 anneal causes slight oxidation of SiC surface, which results in generation of interface defects. Figure 4.4 schematically illustrates the defect reduction and formation processes induced by CO_2 annealing. The bright spot density (Fig. 4.3 (b)) follows trend similar to that of the integrated intensity. CO_2 annealing rapidly reduced the bright spot density to 5.60×10^5 cm^{-2} within 15 min, which is more than two orders of magnitude lower than that of the as-oxidized sample (7.4×10^7 cm^{-2}) and comparable to the value achieved after 90 min of Ar annealing (5.56×10^5 cm^{-2}). However, further prolonging CO_2 anneal forms additional bright spots at the interface. Although Ar anneal yielded a monotonic decrease in their density, the reduction rate was slower than with CO_2 anneal. Consequently, CO_2 anneal is remarkably effective at simultaneously suppressing background luminescence and reducing the number of bright spots with a short term of annealing, thereby enabling the formation of spatially well-isolated SPEs at the interface.

4.4 Electrical Characteristics of MOS Capacitors

This section evaluates the densities of electrically active defects at the SiO_2/SiC interface through the C–V measurements on MOS capacitors. This study focuses on the N_{Eff}, which was previously found to correlate with the color center density in Chapter 3. The evaluation procedure for N_{Eff} was detailed in Section 3.2.3. Figure 4.5 presents the single-directional C–V characteristics of (a) CO_2-annealed and (b) Ar-annealed SiC MOS capacitors measured at 1 MHz. The capacitance values were normalized by C_{OX}. The gate voltage was swept from negative (depletion) to positive (accumulation) direction. As a reference, the result of as-oxidized sample is also shown as a grey line. As can be seen, the V_{FB} of the as-ox. sample shifted positively from the ideal V_{FB} position, and a

capacitance plateau was observed, indicating that the presence of significant amount of interface electron traps. After a few minutes of either CO_2 or Ar annealing, the C–V curves moved remarkably closer to the ideal V_{FB} value and became steeper. With prolonged anneal, the curve shifted even closer to the ideal V_{FB} position and became even steeper. Comparing the CO_2 and Ar annealed samples, the C–V curves of Ar anneal were slightly more stretched out than those of CO_2 anneal ones, indicating that CO_2 anneal is more effective in reducing interface states. For a more quantitative discussion,

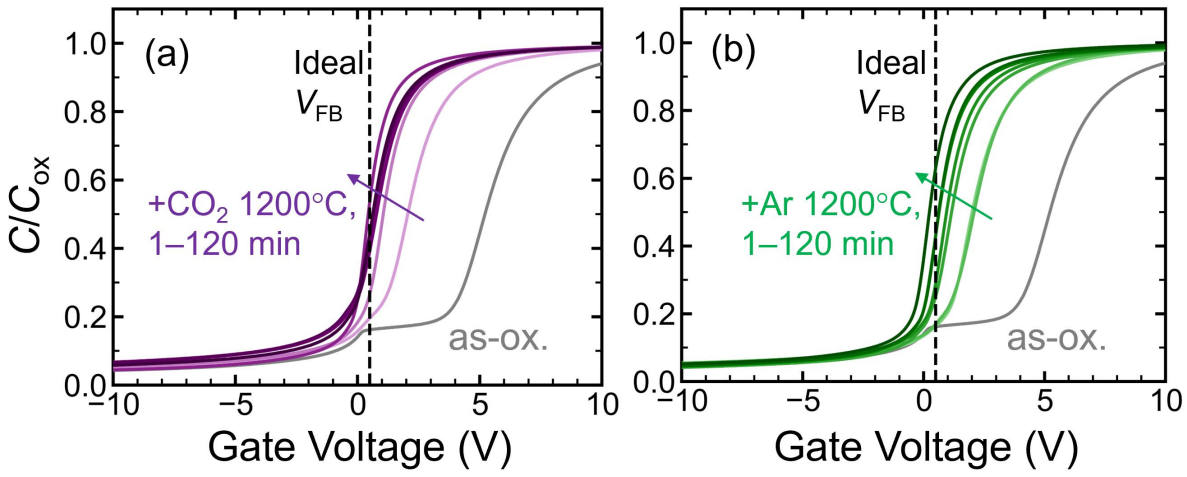

Figure 4.5. Single-directional C–V characteristics of (a) +CO_2 and (b) +Ar annealing samples. The result of as-oxidized sample is also shown in each figure as grey solid line. Black dashed line indicates position of the ideal V_{FB}.

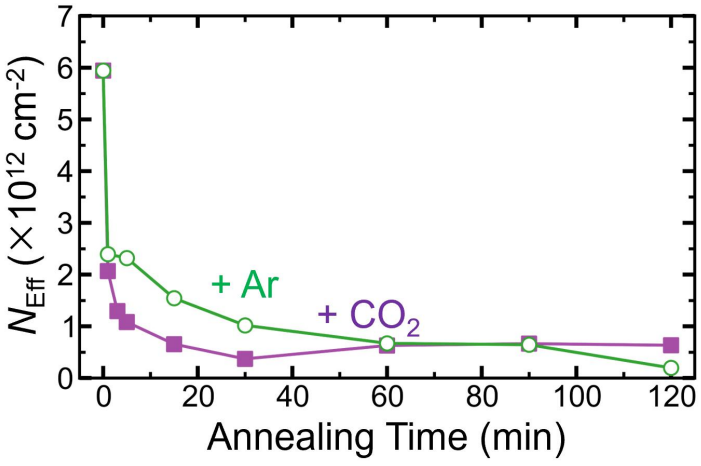

Figure 4.6. N_{Eff} as a function of anneal duration. Green and purple plots indicate the results of +CO_2 or Ar annealed samples, respectively.

Figure 4.6 shows the variation of N_{Eff} as a function of the post-oxidation anneal duration in either CO_2 or Ar atmospheres. N_{Eff} represents the density of the effective fixed charges at the interface, and the majority of these charges are attributed to deep-acceptor type defects. Turning into the results, for shorter annealing, N_{Eff} of both Ar and CO_2 annealed samples decreased monotonically with increasing anneal duration. The reduction of N_{Eff} under CO_2 anneal proceeded more rapidly than under Ar anneal, implying that the defect removal was driven not only by a pure thermal effect but also by a chemical reaction involving CO_2 molecules. Prolonged annealing in CO_2 atmosphere led to a slight increase in N_{Eff}, suggesting the formation of additional defects. This behavior is consistent with the dependence of the optical properties on the electrically active defect density, where the initial reduction of defects leads to an increase in the number of color centers and an enhancement of the integrated PL intensity, while prolonged CO_2 annealing results in a slight degradation due to the formation of additional defects. It can be concluded that the CO_2 anneal is particularly effective in reducing the electrically active defects, similar with the color centers as described in Section 4.3. Excessive annealing should be carefully controlled, as it may lead to the unwanted defect formation at the interface.

4.5 Correlation Between Color Centers and Electrically Active Defects

Figure 4.7 (b) summarizes the dependence of the bright spot density (solid lines) and the effective fixed charge density N_{Eff} (dashed lines) on the anneal duration in either CO_2 or Ar ambient. As shown in Fig. 4.7 (a), most of N_{Eff} is considered to originate from deep acceptor-type interface states, which can contribute to a positive shift in V_{FB}.

In the CO_2 annealing series, both the bright spot density and N_{Eff} rapidly decrease at short anneal durations, indicating that CO_2 annealing efficiently passivates electrically active interface defects that also serve as color centers. In contrast, Ar annealing results in a more gradual reduction in both quantities, reflecting its weaker passivation capability.

For CO_2 anneal durations longer than about 30 min, however, both the bright spot density and N_{Eff} begin to increase again, suggesting that prolonged CO_2 annealing induces the formation of additional defects. This annealing behavior is conceptually illustrated in Fig. 4.8. In the as-oxidized sample, a high density of both N_{Eff} and color centers is present at the interface. Following CO_2 annealing, both types of defects are reduced.

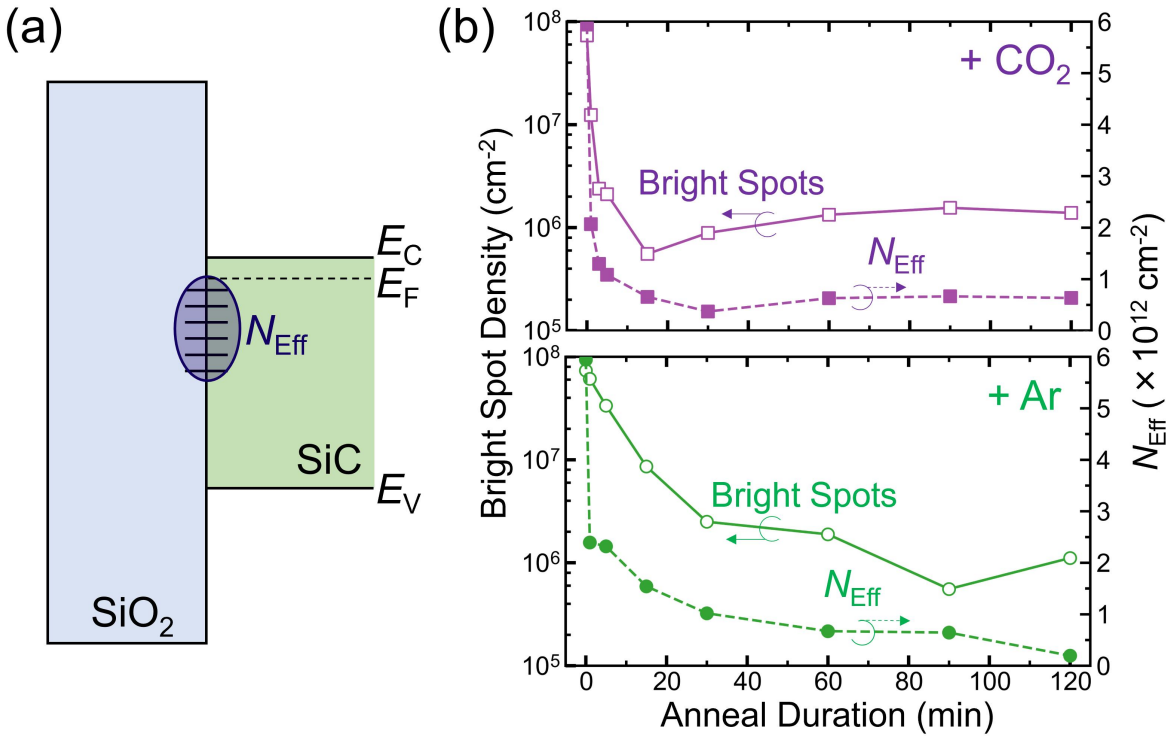

Figure 4.7. (a) Schematic illustration of the energetic position of N_{Eff} at the SiO_2/SiC interface. (b) Bright spot density (Solid lines) and N_{Eff} (dashed lines) as functions of anneal duration in either CO_2 or Ar atmosphere. Note that right axis corresponds to the linear-scale N_{Eff}, whereas the left axis corresponds to log-scale bright spot density.

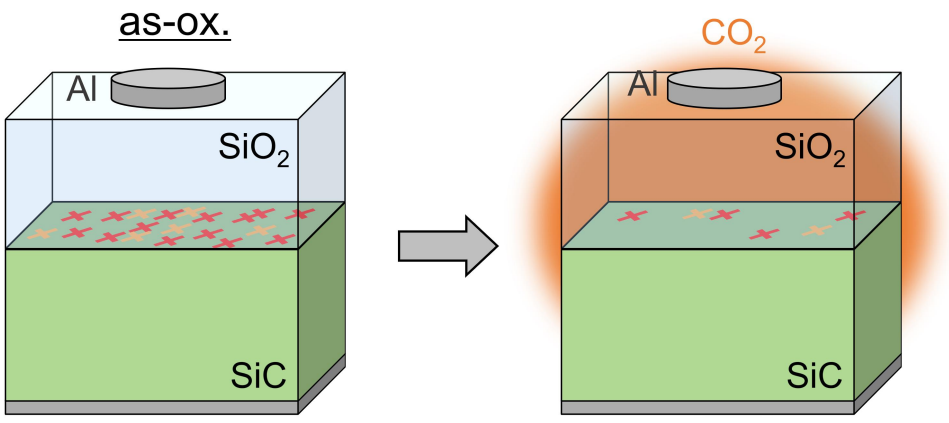

Figure 4.8. Conceptual illustrations summarizing the reduction of interface defects by CO_2 annealing, where the defect density remains lower than that of the as-oxidized sample. Red crosses represent electrically active interface defects, while orange crosses indicate color centers.

The correlation observed between the bright spot density and N_{Eff} throughout the entire annealing sequence indicates that the interface color centers originate from deep acceptor-type interface defects. This is consistent with their contribution to the positive V_{FB} shift observed in the C–V measurements. The microscopic origin of these interface SPEs is further examined in Chapter 5.

4.6 Relationship Between SPE Ratio and Background luminescence

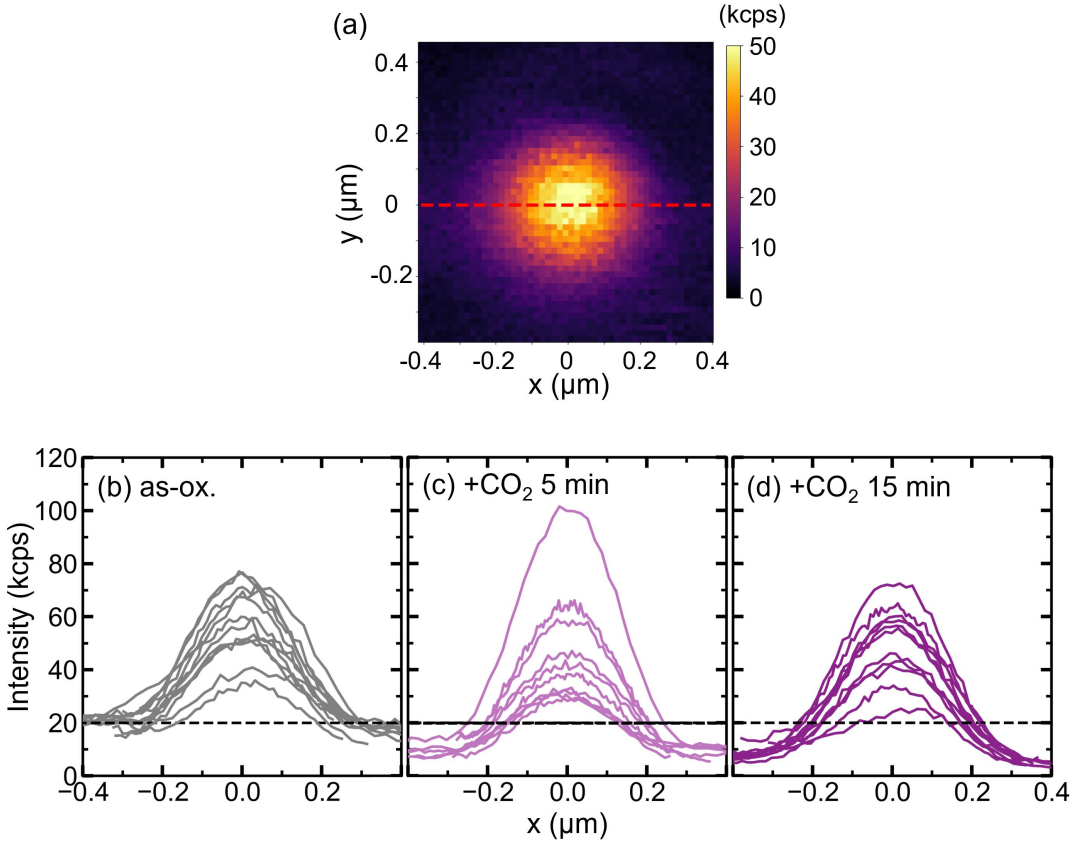

Figure 4.9. (a) Typical high resolution confocal PL mapping image. The cross-sectional intensity profiles of (b) as-ox., (c) +CO_2 5 min, and (d) +CO_2 15 min samples.

Section 4.3 analyzed the color center density and the background luminescence obtained from confocal PL mapping images. This section presents the strategy for reliable formation of SPEs. To this end, several bright spots identified in the confocal PL mapping images were analyzed by HBT measurements to evaluate their single photon character-

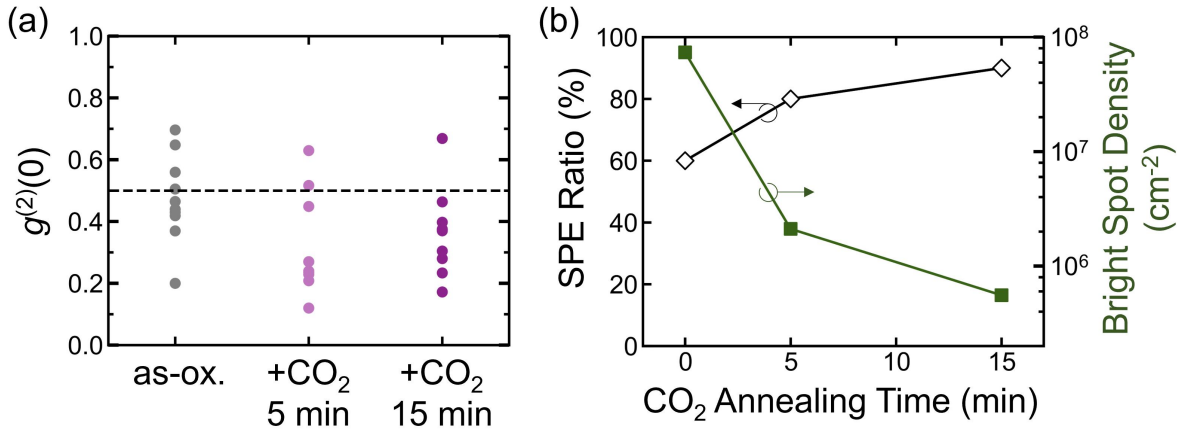

Figure 4.10. (a) The $g^{(2)}(0)$ values obtained from ten bright spots of each as-ox., $+CO_2$ 5 min, and $+CO_2$ 15 min sample. (b) SPE ratio and bright spot density as a function of CO_2 annealing time.

istics. Figure 4.9 shows cross-sectional PL intensity profiles of ten representative bright spots in (a) as-ox., (b) + CO_2 5 min, and (c) + CO_2 15 min samples. For the as-oxidized sample, the background luminescence of almost all bright spots exceeded 20 kcps, which value was adopted as the threshold intensity to classify bright spots (Fig. 4.9 (b)). In contrast, the sample annealed in CO_2 exhibited lower background luminescence (Figs. 4.9 (c) and (d)). The second-order autocorrelation functions were evaluated for the bright spots in each sample, and the resulting $g^{(2)}(0)$ values were plotted in Fig. 4.10 (a). The number of spots with $g^{(2)}(0)$ below 0.5 increased as the CO_2 anneal duration was prolonged. The SPE ratio, defined as the number of bright spots with $g^{(2)}(0)$ below 0.5 divided by the total number of investigated bright spots, was plotted as a function of CO_2 anneal time (Fig. 4.10 (b)). According to the results, the SPE ratio of the as-ox. sample was only 60%, but it increased to 80% with CO_2 anneal for 5 min, while the bright spot density decreased from 7.35×10^7 cm^{-2} to 2.11×10^6 cm^{-2}. The SPE ratio was further increased to 90% after 15 min of CO_2 annealing. At the same time, the bright spot density decreased further to 5.56×10^5 cm^{-2}. These results suggest that background luminescence, including emission from dim spots, degrades the single photon characteristics. It was also found that background luminescence correlates with bright spot density, indicating that reducing the bright spot density is necessary to suppress background luminescence. Figure 4.11 illustrates the mechanisms for reliable formation of well-isolated SPEs. When many color centers lie within the focal volume (Fig. 4.11 (a)), photons from multiple

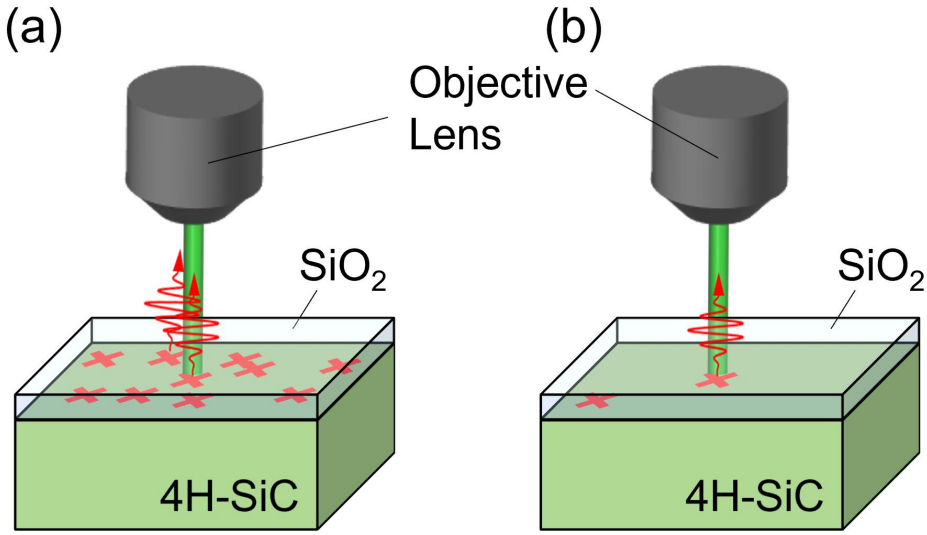

Figure 4.11. Conceptual illustrations of spatial isolation of interface SPEs. (a) High-density interface defects: multiple color centers (red crosses) lie within the collection volume of the objective lens, causing photons from different defects to be detected simultaneously and thereby degrading the measured $g^{(2)}(0)$ values. (b) Spatially isolated SPEs: only a single defect resides within the collection volume, enabling high-purity single-photon emission with $g^{(2)}(0) < 0.5$.

color centers enter the objective simultaneously. Even if each color centers individually exhibits anti-bunching behavior, the mixed photon stream results in an elevated $g^{(2)}(0)$ value. This effect has been reported in previous studies, where nearby color centers degraded the measured purity despite preserved anti-bunching [138]. In contrast, when the interface contains only one bright spot within the collection volume (Fig. 4.11 (b)), no multi-photon contribution arises from neighboring centers, and single-photon emission is consistently obtained. In conclusion, post-oxidation CO_2 annealing is an effective approach for forming spatially well-isolated SPEs at the interface.

4.7 Summary

In summary, this study systematically evaluated the impact of post-oxidation annealing in a CO2 atmosphere by quantifying the densities of color centers and electrically active defects (i.e., N_{Eff}) at the SiO_2/SiC interface. CO_2 annealing produced a more rapid and pronounced reduction in both bright spot density and integrated intensity than Ar annealing. Consequently, CO_2 annealing enables wide range tunability of the bright spot

density, from 5.6×10^5 cm^{-2} to 7.4×10^7 cm^{-2}. While controlling the color center density by tuning anneal temperature has been reported in Chapter 3, the present study demonstrates that varying only the anneal duration at a fixed temperature of 1200°C is sufficient to modulate the color center density effectively. Furthermore, the analysis of the SPE ratio as a function of CO_2 anneal duration indicated that reducing background luminescence is essential for achieving stable single photon emission. Taken together, these findings provide a practical strategy for the reliable formation of the interface SPEs.

Chapter 5

Discussions

This chapter builds upon the results presented in Chapters 3 and 4 and provides a comprehensive discussion of the mechanisms that govern the formation and annihilation of color centers at the SiO_2/SiC interface. The preceding chapters demonstrated that high-temperature oxidation and post-oxidation annealing in a CO_2 atmosphere enable wide-range controllability of the color center density at the interface. In addition, several clues for elucidating the physical nature of the interface SPEs have been obtained by investigating the relationship between color centers and electrically active defects at the interface. Furthermore, comparative analyses with Ar annealing indicated that defect reduction is not attributable solely to thermal processes, but also involves reactions with CO_2 molecules.

To elucidate the physics underlying these observations, this chapter discusses three key aspects: (1) the mechanisms responsible for the reduction of interface defects and the formation of spatially separated SPEs, (2) the origin of the discrepancy between electrically measured charge densities and color center densities, and (3) the possible microscopic origin of the interface SPEs.

Through these discussions, a unified fundamental physical picture on both the controllability and the defect origins of the interface SPEs is established, providing a foundation for their reliable and scalable implementation in SiC-based quantum photonic platforms.

5.1 Mechanisms of Defect Reduction

The formation and reduction of color centers at the SiO_2/SiC interface arise from the interplay among thermally driven reactions, carbon transport, and oxygen-assisted defect

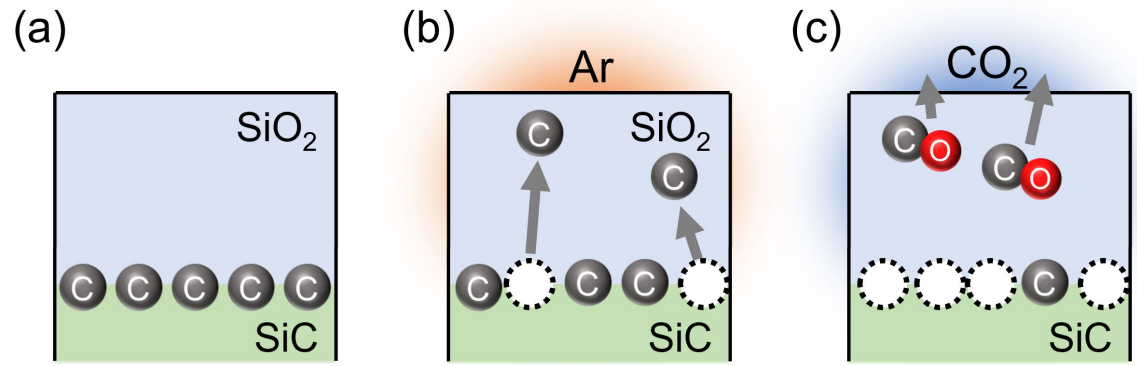

Figure 5.1. (a) Schematic of carbon-related interface defects formed during oxidation. (b) Under Ar annealing, carbon atoms gradually diffuse toward the SiO_2 side. (c) CO_2 annealing provides an oxygen source that can react with carbon-related defects, promoting their dissociation and thereby accelerating defect reduction.

chemistry occurring during oxidation and post-oxidation annealing. Chapters 3 and 4 demonstrated that both the color center density and the densities of electrically active defects can be widely tuned through oxidation temperature and CO_2 annealing. High-temperature oxidation suppresses carbon-related defects generated during SiC oxidation, whereas CO_2 annealing further accelerates their removal and enables the reliable formation of spatially isolated SPEs.

Figure 5.1 summarizes the defect-reduction mechanisms. As shown in Fig. 5.1 (a), previous studies have reported that residual carbon tends to remain at the SiO_2/SiC interface during thermal oxidation [112, 117]. This is consistent with Chapter 3, where increasing oxidation temperature led to decreases in both the bright spot density and N_{Eff} through enhanced desorption and out-diffusion of carbon-related interface defects.

During subsequent Ar annealing, carbon atoms diffuse toward the SiO_2 side, as experimentally shown in Ref. [117]. This behavior is illustrated in Fig. 5.1 (b). Such diffusion accounts for the gradual reduction in color center density and N_{Eff} observed under Ar annealing, driven predominantly by thermal processes without significant chemical modification of the interface.

In contrast, CO_2 annealing produces a more rapid decrease within a short annealing duration. As depicted in Fig. 5.1 (c), CO_2 acts as a source of active oxygen species, which may compensate oxygen vacancies in the SiO_2 film [136] and promote dissociation of carbon-related defects at the interface. These oxygen-assisted reactions are consistent

with DFT predictions [139] and experimental studies on defect suppression under low oxygen partial pressure [140]. This mechanism explains why CO_2 annealing decreases both the bright spot density and N_{Eff} more effectively than Ar annealing.

Prolonged CO_2 annealing, however, caused a slight increase in the color center density. This is attributed to slow oxidation of the SiC surface by CO_2, whose activation energy (7.5 eV) is higher than that for standard oxidation [134, 141, 142], but nevertheless becomes relevant during extended annealing, thereby introducing new defects. In contrast, Ar does not oxidize SiC and thus yields nearly monotonic defect reduction.

In summary, carbon-defect annihilation, carbon diffusion toward the oxide, oxygen-assisted dissociation under CO_2, and optimization of annealing duration collectively form a coherent framework for understanding and engineering isolated SPE formation at the SiO_2/SiC interface.

5.2 Strategy for Reliable Formation of Interface SPEs

In addition to reducing the overall defect density, annealing plays a critical role in ensuring the single-photon properties and spatial isolation of the interface SPEs. Although all measured color centers exhibited anti-bunching behavior, several centers showed $g^{(2)}(0)$ values exceeding 0.5, indicating degraded single-photon purity. Chapter 3 demonstrated that only 66.6% of the color centers formed by 1200°C oxidation were SPEs, whereas

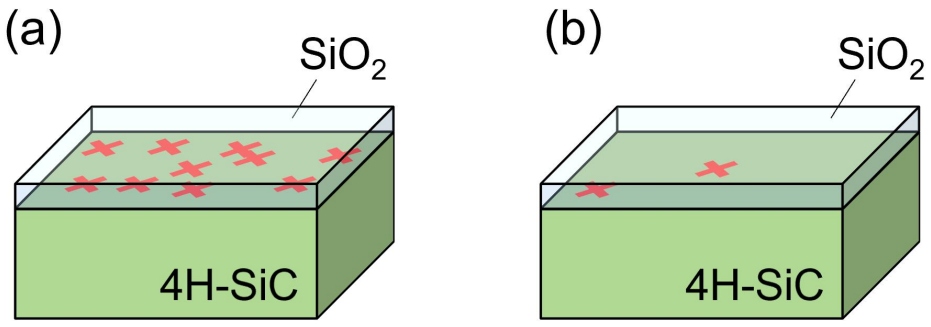

Figure 5.2. Strategy for reliable formation of spatially well-isolated SPEs. (a) High-density interface defects, where multiple color centers (red crosses) are present in proximity. (b) Spatially isolated interface SPEs, free from local strain and interference from neighboring SPEs, enabling high-purity single-photon emission.

84.6% of the centers obtained by 1500°C oxidation satisfied $g^{(2)}(0) < 0.5$. This improvement correlated with the reduced color center density at higher oxidation temperature. Moreover, post-oxidation CO_2 annealing at 1200°C drastically suppressed the color center density, and all measured centers exhibited high-purity single-photon emission with $g^{(2)}(0) < 0.5$.

The ES lifetime of the interface SPEs is on the order of several nanoseconds, consistent with earlier reports [104]. Because the timing jitter of the APDs used (350 ps in Chapter 3 and 750 ps in Chapter 4) is sufficiently smaller than the SPE lifetime, instrumental broadening does not significantly influence the measured $g^{(2)}(0)$ values. Therefore, the degradation of the SPE purity is attributed not to detector limitations but to spatial overlap of multiple SPEs.

Figure 5.2 illustrates the strategy for the reliable formation of spatially well-isolated SPEs. When multiple SPEs are located in close proximity are present (Fig. 5.2 (a)), photons emitted from different defects are collected simultaneously. In this situation, although each color center individually exhibits anti-bunching, the combined photon stream elevates the measured $g^{(2)}(0)$ value above 0.5, preventing the defect from functioning as an SPE. Such degradation of apparent single-photon purity due to neighboring color centers has also been reported in previous studies [138]. In contrast, when a SPEs is spatially isolated (Fig. 5.2 (b)), no additional photon contribution from nearby defects is present, enabling high-purity single-photon emission with reliably low $g^{(2)}(0)$ values below 0.5.

These results collectively demonstrate that CO_2 annealing is effective not only for reducing the density of color centers but also for creating spatially well-isolated SPEs that occupy the objective's collection volume individually. Such isolated configurations are essential for achieving reliable high-purity single-photon emission required for practical quantum applications.

5.3 Discrepancy Between Electrical Charge and Color Center Densities

As demonstrated in Chapters 3 and 4, the density of electrically active defects and that of optically visible color centers differ by several orders of magnitude. While the effective fixed charge density, N_{Eff}, typically lies in the range of 10^{11}–10^{12} cm^{-2}, the color center density identified via confocal PL mapping is only 10^{5}–10^{7} cm^{-2}. This large discrepancy

indicates that only a small fraction of electrically detectable defects emit photons under the optical excitation used in this work. The origins of this mismatch can be understood from four independent but complementary factors, illustrated in Figs. 5.3–**??**.

First, the optical measurements inherently select only bright and optically stable color centers. As shown in Fig. 5.3 (a), confocal PL mapping detects both bright and dim spots; however, the PL analysis in this dissertation employed intensity thresholds that were chosen to be appropriate for each optical setup (50 kcps in Chapter 3 and 20 kcps in Chapter 4). Thus, dim spots and defects exhibiting blinking or instability were excluded. As a result, the measured density reflects only radiative defects that are sufficiently bright and stable.

Second, some nearby defects create background luminescence that suppresses the detectability of individual color centers. When multiple defects lie within the focal volume (Fig. 5.3 (b)), background emission or crosstalk can obscure weaker color centers, preventing them from being identified as color centers in PL mapping.

Third, only a limited fraction of interface defects possess an energy-level structure that supports radiative recombination. A defect must exhibit an allowed optical transition with sufficient wavefunction overlap to generate a PL emission, as schematically shown in Fig. 5.4. Many electrically active defects predominantly relax via non-radiative channels or emit outside the visible spectral range. Because the detection system was sensitive

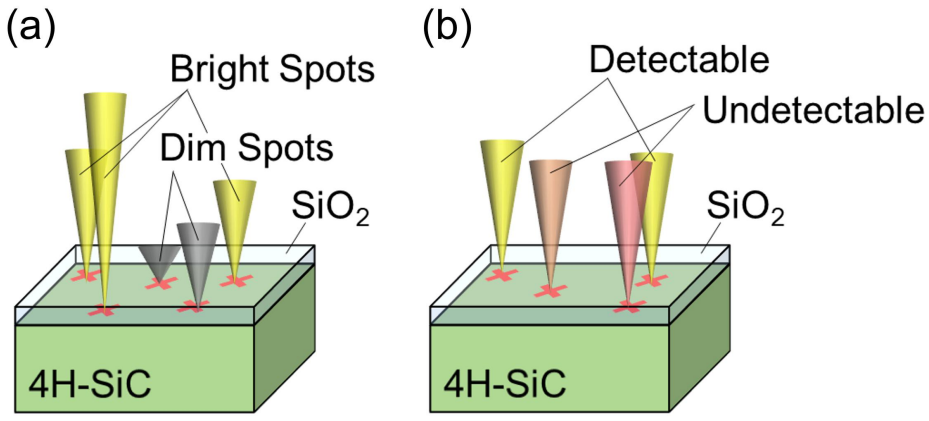

Figure 5.3. (a) Optical-selection effect: only bright and optically stable centers are detected, while dim or unstable defects are excluded from PL analysis. (b) Spatial crowding: when multiple defects lie within the focal volume, background photons from neighboring centers obscure weaker color centers, reducing the detectable color center density.

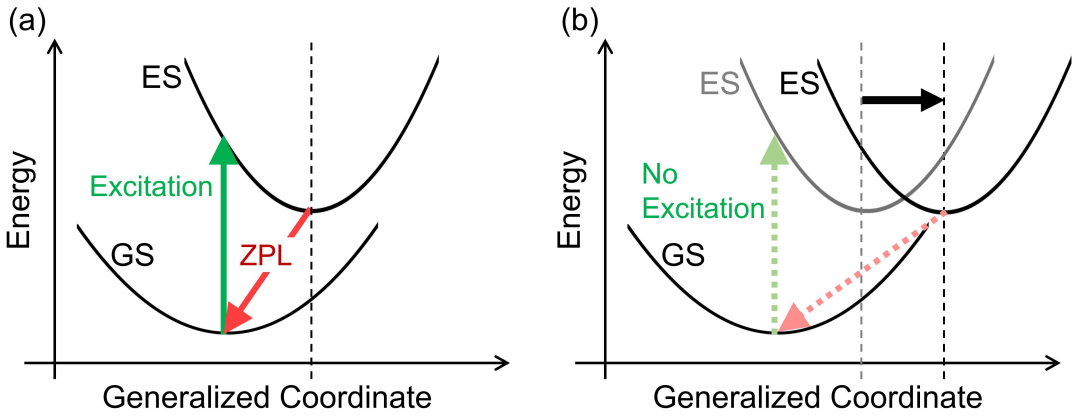

Figure 5.4. Energy-level selection effect: only defects with allowed optical transitions and sufficient radiative decay compete with non-radiative channels to produce photon emission. Defects lacking an appropriate GS-ES level scheme or emitting outside the detection bandwidth (500–800 nm) remain invisible in PL measurements.

primarily to 550–850 nm (Chapter 3) or 500–800 nm (Chapter 4), any color centers in the near-infrared range are not detected, further lowering the measured PL-visible density.

Finally, the charge-state requirement of defects determines whether emission is possible. Only some defects possess a charge state that supports optical emission under the applied bias and excitation conditions. Prior studies have shown that certain interface defects switch between radiative and non-radiative charge states, while others remain non-radiative regardless of applied voltage. Therefore, although many defects contribute to electrical measurements, only a subset achieve a radiative charge state, further reducing the number of color centers.

Taken together, these mechanisms explain why the density of color centers is several orders of magnitude smaller than the electrically measured defect density. Importantly, this discrepancy does not contradict the correlation identified in Chapter 4 between N_{Eff} and the color center density, as both quantities exhibit similar trends with respect to the annealing conditions. Rather, it indicates that the SiO_2/SiC interface contains a broad distribution of defect species, of which only a limited fraction become radiatively active within the detectable wavelength range and under charge-state conditions favorable for photon emission.

5.4 Possible Origin of Interface SPEs

This section discusses the possible microscopic origin of the interface color centers. A variety of intrinsic defects have been proposed or experimentally identified near the SiO_2/SiC interface, including (i) near-interface oxide defects such as carbon dimers and V_O, (ii) interface defects, such as carbon dimers and the P_{bC} center, and (iii) near-interface bulk defects, such as oxygen-related complexes and $(C_2)_{Si}$.

Among these possibilities, extensive DLTS- and magnetic resonance-based studies have identified several carbon-related interface defects [117, 119], consistent with DFT calculations [83, 112]. Recent theoretical work further predicts that carbon clusters located on the SiC side of the interface can act as optically active quantum defects. In particular, $(C_{i,Split})$ and $(C_2)_{Si}$ introduce acceptor-type charge-transition levels within the SiC bandgap [111, 143]. Notably, the calculated transition levels of $(C_2)_{Si}$ lie close to the experimentally observed acceptor levels of the interface SPEs, $(E_C - 0.65)$–$(E_C - 0.92)$ eV [144], supporting this defect as a strong microscopic candidate.

Although the exact depth of the interface SPEs cannot be resolved by confocal PL mapping due to its $\sim$1 μm axial resolution (described in Chapter 2), polarization-dependent emission measurements provide important insight. The transition dipole moments of the interface SPEs exhibit alignment with crystallographic directions of 4H-SiC [104, 105, 110]. Such orientation is incompatible with amorphous SiO_2 defects and instead indicates that the color centers reside at the interface boundary or within a few nanometers inside the SiC lattice. This observation further narrows the likely origin to carbon-related defects on the SiC side.

Within this framework, the observed effects of post-oxidation annealing are consistent with the mechanisms discussed in Section 5.2 and can be qualitatively understood by considering modifications of the candidate defect species.

Taken together, these observations support a model in which the interface color centers originate from carbon-related defects located on the SiC side of the interface, as depicted in Fig. 5.5. The annealing behavior—summarized by the correlated evolution of bright spot density and N_{Eff}—is naturally explained by the passivation and reconfiguration of these carbon-based defect species.

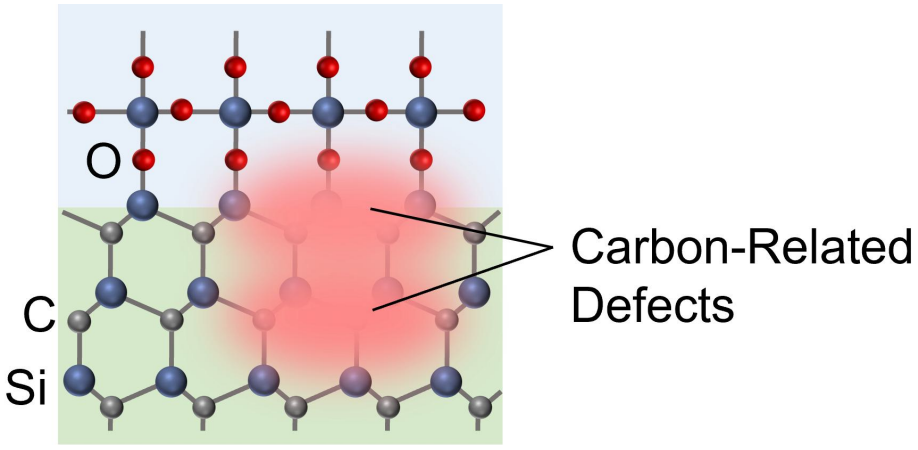

Figure 5.5. Schematic illustration of the plausible spatial location of interface SPEs.

Chapter 6

Conclusion

6.1 Summary of This Dissertation

This dissertation explored the fundamental understanding and control of SPEs located at the SiO_2/SiC interface, with a broader aim of establishing a reliable and scalable platform for quantum light sources based on SiC. By combining optical and electrical characterizations under systematically varied oxidation and annealing conditions, this work elucidated the mechanisms by which interface color centers are formed, modified, and annihilated, and clarified their relationship with electrically active interface defects. The results obtained throughout this dissertation provide essential guidelines for realizing reproducible formation of SPEs using conventional device fabrication technologies.

Chapter 1 summarized the motivation for defect-based SPEs and highlighted the advantages of SiC as a host material, including wafer-scale manufacturability, biocompatibility and thermal robustness, and compatibility with existing semiconductor technologies. Among the various defect systems in SiC, SPEs at the SiO_2/SiC interface are particularly attractive because they can be formed without ion implantation or complex microfabrication, while still exhibiting strong luminescence even at room temperature and electrically controllable photon emission. However, challenges remain in identifying their microscopic origin, reducing the variation of PL spectra, and establishing a reliable process for controlling the SPEs density.

Chapter 2 introduced the underlying mechanisms and measurement methods of CLSM, and established the optical characterization workflow used throughout this dissertation. In this system, confocal PL mapping is first employed to visualize the spatial distribution

of individual interface color centers with high spatial resolution. Once these centers are identified, PL spectroscopy is performed to determine their spectral characteristics. In addition, HBT measurements are conducted to evaluate their single-photon characteristics through the second-order autocorrelation function $g^{(2)}(\tau)$. This chapter therefore provides the principles of the experimental setup used to detect individual interface defects and to characterize their optical signatures in all subsequent chapters.

Chapter 3 addressed these issues by performing high-temperature oxidation and post-oxidation annealing in CO_2 atmosphere at various temperatures. Using confocal PL mapping, the spatial distribution, density, and single-photon characteristics of the interface color centers were quantitatively evaluated. C–V measurements further revealed the densities of electrically active defects, including the N_{Eff}, N_{Hys}, and $N_{\mathrm{E_V}}$. By comparing samples processed under different temperatures, this chapter demonstrated that high-temperature oxidation suppresses residual carbon defects at the interface, leading to reductions in both color center density and the N_{Eff}. CO_2 annealing provided controllability wide range of the color center density ranging from the order of 10^5 to 10^7 cm^{-2}. In addition, HBT measurements confirmed that oxidation alone is insufficient to yield a high fraction of SPEs, whereas CO_2 annealing significantly increases the proportion of color centers that behave as SPEs. Although not all centers exhibited ideal single-photon characteristics due to overlap with neighboring color centers and background luminescence, these findings demonstrate that CO_2 annealing is a practical and effective process for enhancing the formation yield of interface SPEs.

Building upon these results, Chapter 4 focused on elucidating the detailed role of CO_2 annealing. By varying only the anneal duration and comparing CO_2 with Ar annealing under identical temperature conditions, the study clarified the extent to which defect reduction originates from pure thermal processes and from reactions involving CO_2 molecules. CO_2 annealing produced a pronounced and rapid reduction in both the color center density and the electrically active defect density (i.e., N_{Eff}), and was more effective than Ar annealing. The correlation between bright spot density and integrated PL intensity indicated that these optical metrics arise from a common microscopic defect species. Furthermore, by analyzing the SPE ratio, the chapter demonstrated that suppression of background luminescence is essential for achieving stable and high-purity single photon emission. These insights provide a clear process-based strategy for controlling interface SPEs.

Chapter 5 integrated the findings of Chapters 3 and 4 and provided a deeper physical interpretation of the underlying mechanisms. The discussion first clarified the mechanism of defect reduction induced by CO_2 annealing, in which oxygen-assisted dissociation of carbon-related defects reduces the number of color centers. Based on this understanding, the chapter proposed a strategy for the reliable formation of interface SPEs, highlighting the importance of optimizing the annealing duration and thermal budget to form spatially isolated SPEs while suppressing defect regeneration. The discussion then addressed the apparent discrepancy between the electrically measured defect density (N_{Eff} ranging from 10^{11} to 10^{12} cm^{-2}) and the color center density (10^{5} to 10^{7} cm^{-2}), which differ by several orders of magnitude. This discrepancy was attributed to limitations in the detection wavelength range, brightness thresholds in PL imaging, the radiative efficiency of individual defect species, and the requirement of an appropriate charge state for photon emission. Finally, the discussion suggested that carbon-related defects, such as (C2)Si and carbon clusters on the SiC side of the interface, are plausible microscopic origins of the interface SPEs, supported by both DFT calculations and experimental reports on defect energetics.

Overall, this dissertation clarified the mechanisms of control the interface SPEs density by post-oxidation annealing, and spatial isolation of SPEs at the SiO_2/SiC interface. The results demonstrate that CO_2 annealing accelerates defect annihilation, and that optimized annealing enables the formation of spatially well-isolated SPEs. These findings provide practical guidelines and a robust processing strategy for the formation of interface SPEs using standard SiC MOS technologies.

6.2 Future Prospects

The findings presented in this dissertation suggest several important research directions toward the practical realization of interface SPEs in quantum technologies:

- **Microscopic identification of the defect structure.** Although certain correlations between the optically and electrically active defects have been established in this study, the precise atomic configuration of the interface SPEs remains unresolved. A combination of first-principles calculations, isotopic engineering, super-resolution PL mapping, and spin-based spectroscopies will be effective in revealing their microscopic origin.

- **Improving spectral uniformity and wavelength stability.** Interface SPEs exhibit significant spatial variations in their emission wavelengths. Understanding and controlling local strain, charge environments, and oxidation-induced structural disorder will be crucial for achieving reproducible formation of uniform interface SPEs. In this study, CO_2 annealing was found to partially suppress such spectral fluctuations by reducing background luminescence and stabilizing the local defect environment, suggesting that further optimization of oxidation and annealing conditions may enable improved wavelength uniformity.

- **Exploration of spin properties.** The spin degree of freedom of interface SPEs has not yet been identified. Demonstrating ODMR or PDMR will be essential for determining whether these emitters possess optically addressable spin states, a key requirement for quantum sensing and spin–photon interface applications. The defect-stabilizing effect of CO_2 annealing revealed in this work indicates that suitably engineered interface environments may facilitate future spin-resolved investigations.

- **Integration with electrically driven devices.** Because interface SPEs inherently reside within MOS structures, electrically driven single photon emission emerges as a realistic prospect. This enables the development of high-brightness, scalable quantum light sources that are compatible with existing platforms.

References

[1] Quantum Economic Development Consortium (QED-C). *2025 State of the Global Quantum Industry*. Testimony before the U.S. House of Representatives, Subcommittee on Research and Technology. Global quantum market projected to reach USD 1.88 billion in 2025 with an annual growth rate of 27.3%. 2025. URL: https://www.congress.gov/119/meeting/house/118196/witnesses/HHRG-119-SY00-Wstate-MerzB001291-20250507.pdf.

[2] Google Quantum AI and Collaborators, *Nature*, **646**, 825 (2025).

[3] C. Gidney, *arXiv*, 2505.15917 (2025).

[4] P. W. Shor and J. Preskill, *Phys. Rev. Lett.* **85**, 441 (2000).

[5] C. L. Degen, F. Reinhard, and P. Cappellaro, *Rev. Mod. Phys.* **89**, 035002 (2017).

[6] A. M. Kaufman and K.-K. Ni, *Nat. Phys.* **17**, 1324 (2021).

[7] M. Nielsen and I. Chuang, *Quantum Computation and Quantum Information*, Cambridge University Press, (2000).

[8] M. Kjaergaard, M. E. Schwartz, J. Braumüller, P. Krantz, J. I.-J. Wang, S. Gustavsson, and W. D. Oliver, *Annu. Rev. Condens. Matter Phys.* **11**, 369 (2020).

[9] P. Krantz, M. Kjaergaard, F. Yan, T. P. Orlando, S. Gustavsson, and W. D. Oliver, *Appl. Phys. Rev.* **6**, 021318 (2019).

[10] B. Foxen, C. Neill, A. Dunsworth, P. Roushan, B. Chiaro, A. Megrant, J. Kelly, Z. Chen, K. Satzinger, R. Barends, F. Arute, K. Arya, R. Babbush, D. Bacon, J. C. Bardin, S. Boixo, D. Buell, B. Burkett, Y. Chen, R. Collins, E. Farhi, A. Fowler, C. Gidney, M. Giustina, R. Graff, M. Harrigan, T. Huang, S. V. Isakov, E. Jeffrey, Z. Jiang, D. Kafri, K. Kechedzhi, P. Klimov, A. Korotkov, F. Kostritsa, D. Landhuis, E. Lucero, J. McClean, M. McEwen, X. Mi, M. Mohseni, J. Y. Mutus, O. Naaman, M. Neeley, M. Niu, A. Petukhov, C. Quintana, N. Rubin, D. Sank, V.

Smelyanskiy, A. Vainsencher, T. C. White, Z. Yao, P. Yeh, A. Zalcman, H. Neven, J. M. Martinis, and Google AI Quantum, *Phys. Rev. Lett.* **125**, 120504 (2020).

[11] C. D. Bruzewicz, J. Chiaverini, R. McConnell, and J. M. Sage, *Appl. Phys. Rev.* **6**, 021314 (2019).

[12] T. P. Harty, D. T. C. Allcock, C. J. Ballance, L. Guidoni, H. A. Janacek, N. M. Linke, D. N. Stacey, and D. M. Lucas, *Phys. Rev. Lett.* **113**, 220501 (2014).

[13] M. Ringbauer, M. Meth, L. Postler, R. Stricker, R. Blatt, P. Schindler, and T. Monz, *Nat. Phys.* **18**, 1053 (2022).

[14] I. S. Madjarov, J. P. Covey, A. L. Shaw, J. Choi, A. Kale, A. Cooper, H. Pichler, V. Schkolnik, J. R. Williams, and M. Endres, *Nat. Phys.* **16**, 857 (2020).

[15] L. Henriet, L. Beguin, A. Signoles, T. Lahaye, A. Browaeys, G.-O. Reymond, and C. Jurczak, *Quantum*, **4**, 327 (2020).

[16] S. Takeda and A. Furusawa, *APL Photonics*, **4**, 060902 (2019).

[17] F. Flamini, N. Spagnolo, and F. Sciarrino, *Rep. Prog. Phys.* **82**, 016001 (2019).

[18] J. L. O'Brien, A. Furusawa, and J. Vučković, *Nat. Photonics*, **3**, 687 (2009).

[19] V. Scarani, H. Bechmann-Pasquinucci, N. J. Cerf, M. Dušek, N. Lütkenhaus, and M. Peev, *Rev. Mod. Phys.* **81**, 1301 (2009).

[20] C. H. Bennett and G. Brassard, *In Proc. IEEE International Conference on Computers, Systems and Signal Processing*, 175 (1984).

[21] P. Rembold, N. Oshnik, M. M. Müller, S. Montangero, T. Calarco, and E. Neu, *AVS Quantum Sci.* **2**, 024701 (2020).

[22] J. Kitching, *Appl. Phys. Rev.* **5**, 031302 (2018).

[23] S. Cardoso, D. C. Leitao, L. Gameiro, F. Cardoso, R. Ferreira, E. Paz, and P. P. Freitas, *Microsyst. Technol.* **20**, 793 (2014).

[24] G. Shaw, R. B. G. Kramer, N. M. Dempsey, and K. Hasselbach, *Rev. Sci. Instrum.* **87**, 113702 (2016).

[25] M. W. Doherty, N. B. Manson, P. Delaney, F. Jelezko, J. Wrachtrup, and L. C. L. Hollenberg, *Phys. Rep.* **528**, 1 (2013).

[26] F. H. Cho, V. Stepanov, C. Abeywardana, and S. Takahashi, *Methods Enzymol.* **563**, 95 (2015).

[27] E. D. Herbschleb, H. Kato, Y. Maruyama, T. Danjo, T. Makino, S. Yamasaki, I. Ohki, K. Hayashi, H. Morishita, M. Fujiwara, and N. Mizuochi, *Nat. Commun.* **10**, 3766 (2019).

[28] G.-Q. Liu, X. Feng, N. Wang, Q. Li, and R.-B. Liu, *Nat. Commun.* **10**, 1344 (2019).

[29] T. Wolf, P. Neumann, K. Nakamura, H. Sumiya, T. Ohshima, J. Isoya, and J. Wrachtrup, *Phys. Rev. X*, **5**, 041001 (2015).

[30] X. Gao, C. Yu, S. Zhang, H. Lin, J. Guo, M. Ma, Z. Feng, and F.-W. Sun, *Diam. Relat. Mater.* **139**, 110348 (2023).

[31] J. F. Barry, J. M. Schloss, E. Bauch, M. J. Turner, C. A. Hart, L. M. Pham, and R. L. Walsworth, *Rev. Mod. Phys.* **92**, 015004 (2020).

[32] H. J. Kimble, M. Dagenais, and L. Mandel, *Phys. Rev. Lett.* **39**, 691 (1977).

[33] I. Aharonovich, D. Englund, and M. Toth, *Nat. Photonics*, **10**, 631 (2016).

[34] P. Senellart, G. Solomon, and A. White, *Nat. Nanotechnol.* **12**, 1026 (2017).

[35] A. Gruber, A. Dräbenstedt, C. Tietz, L. Fleury, J. Wrachtrup, and C. von Borczyskowski, *Science*, **276**, 2012 (1997).

[36] J. H. N. Loubser and J. A. van Wyk, *Rep. Prog. Phys.* **41**, 1201 (1978).

[37] F. Jelezko, T. Gaebel, I. Popa, A. Gruber, and J. Wrachtrup, *Phys. Rev. Lett.* **92**, 076401 (2004).

[38] F. Jelezko, T. Gaebel, I. Popa, M. Domhan, A. Gruber, and J. Wrachtrup, *Phys. Rev. Lett.* **93**, 130501 (2004).

[39] J. M. Taylor, P. Cappellaro, L. Childress, L. Jiang, D. Budker, P. R. Hemmer, A. Yacoby, R. Walsworth, and M. D. Lukin, *Nat. Phys.* **4**, 810 (2008).

[40] C. L. Degen, *Appl. Phys. Lett.* **92**, 243111 (2008).

[41] J. R. Maze, P. L. Stanwix, J. S. Hodges, S. Hong, J. M. Taylor, P. Cappellaro, L. Jiang, M. V. G. Dutt, E. Togan, A. S. Zibrov, A. Yacoby, R. L. Walsworth, and M. D. Lukin, *Nature*, **455**, 644 (2008).

[42] G. Balasubramanian, I. Y. Chan, R. Kolesov, M. Al-Hmoud, J. Tisler, C. Shin, C. Kim, A. Wojcik, P. R. Hemmer, A. Krueger, T. Hanke, A. Leitenstorfer, R. Bratschitsch, F. Jelezko, and J. Wrachtrup, *Nature*, **455**, 648 (2008).

[43] M. Pompili, S. L. N. Hermans, S. Baier, H. K. C. Beukers, P. C. Humphreys, R. N. Schouten, R. F. L. Vermeulen, M. J. Tiggelman, L. Dos Santos Martins, B. Dirkse, S. Wehner, and R. Hanson, *Science*, **372**, 259 (2021).

[44] S. L. N. Hermans, M. Pompili, H. K. C. Beukers, S. Baier, J. Borregaard, and R. Hanson, *Nature*, **605**, 663 (2022).

[45] K. Arai, A. Kuwahata, D. Nishitani, I. Fujisaki, R. Matsuki, Y. Nishio, Z. Xin, X. Cao, Y. Hatano, S. Onoda, C. Shinei, M. Miyakawa, T. Taniguchi, M. Yamazaki, T. Teraji, T. Ohshima, M. Hatano, M. Sekino, and T. Iwasaki, *Communications Physics*, **5**, 200 (2022).

[46] F. Jelezko and J. Wrachtrup, *Phys. Status Solidi. (a)*, **203**, 3207 (2006).

[47] A. Gali, E. Janzén, P. Deák, G. Kresse, and E. Kaxiras, *Phys. Rev. Lett.* **103**, 186404 (2009).

[48] J. R. Maze, A. Gali, E. Togan, Y. Chu, A. Trifonov, E. Kaxiras, and M. D. Lukin, *New J. Phys.* **13**, 025025 (2011).

[49] G. Thiering and A. Gali, *Phys. Rev. B Condens. Matter*, **96**, 081115 (2017).

[50] H. Roberts, H. Abudayyeh, X. Li, and X. Li, *ACS Nano*, **19**, 22528 (2025).

[51] G. Balasubramanian, P. Neumann, D. Twitchen, M. Markham, R. Kolesov, N. Mizuochi, J. Isoya, J. Achard, J. Beck, J. Tissler, V. Jacques, P. R. Hemmer, F. Jelezko, and J. Wrachtrup, *Nat. Mater.* **8**, 383 (2009).

[52] P. Siyushev, M. Nesladek, E. Bourgeois, M. Gulka, J. Hruby, T. Yamamoto, M. Trupke, T. Teraji, J. Isoya, and F. Jelezko, *Science*, **363**, 728 (2019).

[53] E. Bourgeois, A. Jarmola, P. Siyushev, M. Gulka, J. Hruby, F. Jelezko, D. Budker, and M. Nesladek, *Nat. Commun.* **6**, 8577 (2015).

[54] L. J. Rogers, K. D. Jahnke, M. W. Doherty, A. Dietrich, L. P. McGuinness, C. Müller, T. Teraji, H. Sumiya, J. Isoya, N. B. Manson, and F. Jelezko, *Phys. Rev. B*, **89**, 235101 (2014).

[55] I. Aharonovich, S. Castelletto, D. A. Simpson, C.-H. Su, A. D. Greentree, and S. Prawer, *Rep. Prog. Phys.* **74**, 076501 (2011).

[56] B. C. Rose, D. Huang, Z.-H. Zhang, P. Stevenson, A. M. Tyryshkin, S. Sangtawesin, S. Srinivasan, L. Loudin, M. L. Markham, A. M. Edmonds, D. J. Twitchen, S. A. Lyon, and N. P. de Leon, *Science*, **361**, 60 (2018).

[57] T. Iwasaki, F. Ishibashi, Y. Miyamoto, Y. Doi, S. Kobayashi, T. Miyazaki, K. Tahara, K. D. Jahnke, L. J. Rogers, B. Naydenov, F. Jelezko, S. Yamasaki, S. Nagamachi, T. Inubushi, N. Mizuochi, and M. Hatano, *Sci. Rep.* **5**, 12882 (2015).

[58] T. Iwasaki, Y. Miyamoto, T. Taniguchi, P. Siyushev, M. H. Metsch, F. Jelezko, and M. Hatano, *Phys. Rev. Lett.* **119**, 253601 (2017).

[59] M. E. Trusheim, B. Pingault, N. H. Wan, M. Gündoğan, L. De Santis, R. Debroux, D. Gangloff, C. Purser, K. C. Chen, M. Walsh, J. J. Rose, J. N. Becker, B. Lienhard, E. Bersin, I. Paradeisanos, G. Wang, D. Lyzwa, A. R.-P. Montblanch, G. Malladi, H. Bakhru, A. C. Ferrari, I. A. Walmsley, M. Atatüre, and D. Englund, *Phys. Rev. Lett.* **124**, 023602 (2020).

[60] M. Atatüre, D. Englund, N. Vamivakas, S.-Y. Lee, and J. Wrachtrup, *Nature Reviews Materials*, **3**, 38 (2018).

[61] B. Pingault, J. N. Becker, C. H. H. Schulte, C. Arend, C. Hepp, T. Godde, A. I. Tartakovskii, M. Markham, C. Becher, and M. Atatüre, *Phys. Rev. Lett.* **113**, 263601 (2014).

[62] D. D. Sukachev, A. Sipahigil, C. T. Nguyen, M. K. Bhaskar, R. E. Evans, F. Jelezko, and M. D. Lukin, *Phys. Rev. Lett.* **119**, 223602 (2017).

[63] P. Siyushev, M. H. Metsch, A. Ijaz, J. M. Binder, M. K. Bhaskar, D. D. Sukachev, A. Sipahigil, R. E. Evans, C. T. Nguyen, M. D. Lukin, P. R. Hemmer, Y. N. Palyanov, I. N. Kupriyanov, Y. M. Borzdov, L. J. Rogers, and F. Jelezko, *Phys. Rev. B*, **96**, 081201 (2017).

[64] P. Wang, T. Taniguchi, Y. Miyamoto, M. Hatano, and T. Iwasaki, *ACS Photonics*, **8**, 2947 (2021).

[65] D. D. Awschalom, R. Hanson, J. Wrachtrup, and B. B. Zhou, *Nat. Photonics*, **12**, 516 (2018).

[66] T. M. Babinec, B. J. M. Hausmann, M. Khan, Y. Zhang, J. R. Maze, P. R. Hemmer, and M. Loncar, *Nat. Nanotechnol.* **5**, 195 (2010).

[67] S. Kanai, F. J. Heremans, H. Seo, G. Wolfowicz, C. P. Anderson, S. E. Sullivan, M. Onizhuk, G. Galli, D. D. Awschalom, and H. Ohno, *Proc. Natl. Acad. Sci. U. S. A.* **119**, e2121808119 (2022).

[68] T. Kimoto and J. A. Cooper, *Fundamentals of Silicon Carbide Technology: Growth, Characterization*, John Wiley & Sons, (2014).

[69] J. Miragliotta, D. K. Wickenden, T. J. Kistenmacher, and W. A. Bryden, *J. Opt. Soc. Am. B, JOSAB*, **10**, 1447 (1993).

[70] H. R. Phillip and E. A. Taft, *Phys. Rev.* **136**, A1445 (1964).

[71] S. Singh, J. R. Potopowicz, L. G. Van Uitert, and S. H. Wemple, *Appl. Phys. Lett.* **19**, 53 (1971).

[72] D. E. Aspnes and A. A. Studna, *Phys. Rev. B*, **27**, 985 (1983).

[73] G. Bonaventura, R. Iemmolo, V. La Cognata, M. Zimbone, F. La Via, M. E. Fragalà, M. L. Barcellona, R. Pellitteri, and S. Cavallaro, *Sci. Rep.* **9**, 11540 (2019).

[74] D. Abebayehu, A. J. Spence, M. J. McClure, T. T. Haque, K. O. Rivera, and J. J. Ryan, *J. Biomed. Mater. Res. A*, **107**, 884 (2019).

[75] T. Kimoto and H. Watanabe, *Appl. Phys. Express*, **13**, 120101 (2020).

[76] Y. M. Tairov and V. F. Tsvetkov, *J. Cryst. Growth*, **43**, 209 (1978).

[77] Y. M. Tairov and V. F. Tsvetkov, *J. Cryst. Growth*, **52**, 146 (1981).

[78] N. Kuroda, K. Shibahara, W. S. Yoo, S. Nishino, and H. Matsunami, *in Extended Abstracts of the 19th Conference on Solid State Devices and Materials, Tokyo*, 227 (1987).

[79] IDTechEx. *Tesla's Innovative Power Electronics: The Silicon Carbide Inverter, Explores IDTechEx*. PR Newswire press release. Accessed 2025-11-27. Feb. 2021.

[80] T. Kimoto, *Proc. Jpn. Acad. Ser. B Phys. Biol. Sci.* **98**, 161 (2022).

[81] T. Fukushima, Extended Abstracts of the International Conference on Silicon Carbide and Related Materials (ICSCRM 2019), 2019, PL-1

[82] K. Kawahara, X. Thang Trinh, N. Tien Son, E. Janzén, J. Suda, and T. Kimoto, *J. Appl. Phys.* **115**, 143705 (2014).

[83] V. V. Afanasev, M. Bassler, G. Pensl, and M. Schulz, *Phys. Stat. Sol. (a)*, **162**, 321 (1997).

[84] Á. Gali, *Nanophotonics*, **8**, 1907 (2019).

[85] M. Widmann, S.-Y. Lee, T. Rendler, N. T. Son, H. Fedder, S. Paik, L.-P. Yang, N. Zhao, S. Yang, I. Booker, A. Denisenko, M. Jamali, S. A. Momenzadeh, I. Gerhardt, T. Ohshima, A. Gali, E. Janzén, and J. Wrachtrup, *Nat. Mater.* **14**, 164 (2015).

[86] V. Ivády, J. Davidsson, N. T. Son, T. Ohshima, I. A. Abrikosov, and A. Gali, *Phys. Rev. B*, **96**, 161114 (2017).

[87] H. Kraus, V. A. Soltamov, D. Riedel, S. Väth, F. Fuchs, A. Sperlich, P. G. Baranov, V. Dyakonov, and G. V. Astakhov, *Nat. Phys.* **10**, 157 (2014).

[88] D. J. Christle, A. L. Falk, P. Andrich, P. V. Klimov, J. U. Hassan, N. T. Son, E. Janzén, T. Ohshima, and D. D. Awschalom, *Nat. Mater.* **14**, 160 (2015).

[89] W. F. Koehl, B. B. Buckley, F. J. Heremans, G. Calusine, and D. D. Awschalom, *Nature*, **479**, 84 (2011).

[90] H. J. von Bardeleben, J. L. Cantin, E. Rauls, and U. Gerstmann, *Phys. Rev. B*, **92**, 064104 (2015).

[91] Z. Mu, S. A. Zargaleh, H. J. von Bardeleben, J. E. Fröch, M. Nonahal, H. Cai, X. Yang, J. Yang, X. Li, I. Aharonovich, and W. Gao, *Nano Lett.* **20**, 6142 (2020).

[92] G. Wolfowicz, C. P. Anderson, B. Diler, O. G. Poluektov, F. J. Heremans, and D. D. Awschalom, *Sci. Adv.* **6**, eaaz1192 (2020).

[93] P. Cilibrizzi, M. J. Arshad, B. Tissot, N. T. Son, I. G. Ivanov, T. Astner, P. Koller, M. Ghezellou, J. Ul-Hassan, D. White, C. Bekker, G. Burkard, M. Trupke, and C. Bonato, *Nat. Commun.* **14**, 8448 (2023).

[94] S.-I. Sato, T. Narahara, Y. Abe, Y. Hijikata, T. Umeda, and T. Ohshima, *J. Appl. Phys.* **126**, 083105 (2019).

[95] S. Castelletto, B. C. Johnson, V. Ivády, N. Stavrias, T. Umeda, A. Gali, and T. Ohshima, *Nat. Mater.* **13**, 151 (2014).

[96] G. Wolfowicz, C. P. Anderson, A. L. Yeats, S. J. Whiteley, J. Niklas, O. G. Poluektov, F. J. Heremans, and D. D. Awschalom, *Nat. Commun.* **8**, 1876 (2017).

[97] D. M. Lukin, M. A. Guidry, and J. Vučković, *PRX quantum*, **1**, 020102 (2020).

[98] D. O. Bracher, X. Zhang, and E. L. Hu, *Proc. Natl. Acad. Sci. U. S. A.* **114**, 4060 (2017).

[99] H. Kraus, V. A. Soltamov, F. Fuchs, D. Simin, A. Sperlich, P. G. Baranov, G. V. Astakhov, and V. Dyakonov, *Sci. Rep.* **4**, 5303 (2014).

[100] T. M. Hoang, H. Ishiwata, Y. Masuyama, Y. Yamazaki, K. Kojima, S.-Y. Lee, T. Ohshima, T. Iwasaki, D. Hisamoto, and M. Hatano, *Appl. Phys. Lett.* **118**, 044001 (2021).

[101] Y. Yamazaki, Y. Masuyama, K. Kojima, and T. Ohshima, *Phys. Rev. Appl.* **20**, L031001 (2023).

[102] M. Widmann, M. Niethammer, D. Y. Fedyanin, I. A. Khramtsov, T. Rendler, I. D. Booker, J. Ul Hassan, N. Morioka, Y.-C. Chen, I. G. Ivanov, N. T. Son, T. Ohshima, M. Bockstedte, A. Gali, C. Bonato, S.-Y. Lee, and J. Wrachtrup, *Nano Lett.* **19**, 7173 (2019).

[103] C. P. Anderson, A. Bourassa, K. C. Miao, G. Wolfowicz, P. J. Mintun, A. L. Crook, H. Abe, J. Ul Hassan, N. T. Son, T. Ohshima, and D. D. Awschalom, *Science*, **366**, 1225 (2019).

[104] A. Lohrmann, S. Castelletto, J. R. Klein, T. Ohshima, M. Bosi, M. Negri, D. W. M. Lau, B. C. Gibson, S. Prawer, J. C. McCallum, and B. C. Johnson, *Appl. Phys. Lett.* **108**, 021107 (2016).

[105] A. Lohrmann, N. Iwamoto, Z. Bodrog, S. Castelletto, T. Ohshima, T. J. Karle, A. Gali, S. Prawer, J. C. McCallum, and B. C. Johnson, *Nat. Commun.* **6**, 7783 (2015).

[106] B. C. Johnson, J. Woerle, D. Haasmann, C. T.-K. Lew, R. A. Parker, H. Knowles, B. Pingault, M. Atature, A. Gali, S. Dimitrijev, M. Camarda, and J. C. McCallum, *Phys. Rev. Appl.* **12**, 044024 (2019).

[107] Y. Hijikata, T. Horii, Y. Furukawa, Y.-I. Matsushita, and T. Ohshima, *J. Phys. Commun.* **2**, 111003 (2018).

[108] Y. Abe, T. Umeda, M. Okamoto, R. Kosugi, S. Harada, M. Haruyama, W. Kada, O. Hanaizumi, S. Onoda, and T. Ohshima, *Appl. Phys. Lett.* **112**, 031105 (2018).

[109] S.-I. Sato, T. Honda, T. Makino, Y. Hijikata, S.-Y. Lee, and T. Ohshima, *ACS Photonics*, **5**, 3159 (2018).

[110] M. Kaneko, H. Takashima, K. Shimazaki, S. Takeuchi, and T. Kimoto, *APL Mater.* **11**, 091121 (2023).

[111] P. Li, P. Udvarhelyi, S. Li, B. Huang, and A. Gali, *Phys. Rev. B*, **108**, 085201 (2023).

[112] T. Kobayashi and Y.-I. Matsushita, *J. Appl. Phys.* **126**, 145302 (2019).

[113] Y.-I. Matsushita, Y. Furukawa, Y. Hijikata, and T. Ohshima, *Appl. Surf. Sci.* **464**, 451 (2019).

[114] H. Fujii, M. Kaneko, and T. Kimoto, *Appl. Phys. Express*, **17**, 041004 (2024).

[115] J. M. Knaup, P. Deák, T. Frauenheim, A. Gali, Z. Hajnal, and W. J. Choyke, *Phys. Rev. B*, **72**, 115323 (2005).

[116] T. Umeda, T. Kobayashi, M. Sometani, H. Yano, Y. Matsushita, and S. Harada, *Appl. Phys. Lett.* **116**, 071604 (2020).

[117] T. Kobayashi and T. Kimoto, *Appl. Phys. Lett.* **111**, 062101 (2017).

[118] P. Deák, J. M. Knaup, T. Hornos, C. Thill, A. Gali, and T. Frauenheim, *J. Phys. D Appl. Phys.* **40**, 6242 (2007).

[119] T. Umeda, G.-W. Kim, T. Okuda, M. Sometani, T. Kimoto, and S. Harada, *Appl. Phys. Lett.* **113**, 061605 (2018).

[120] T. Wilson, *J. Microsc.* **244**, 113 (2011).

[121] P. D. Bloch, W. S. Brocklesby, R. T. Harley, and M. J. Henderson, *J. Phys., Colloq.* **46**, C7 (1985).

[122] E. van Oort, N. B. Manson, and M. Glasbeek, *J. Phys.* **21**, 4385 (1988).

[123] C. Kurtsiefer, S. Mayer, P. Zarda, and H. Weinfurter, *Phys. Rev. Lett.* **85**, 290 (2000).

[124] J. C. Burton, L. Sun, F. H. Long, Z. Feng, and I. Ferguson, *Phys. Rev. B*, **59**, 7282 (1999).

[125] J. C. Burton, L. Sun, M. Pophristic, S. J. Lukacs, F. H. Long, Z. C. Feng, and I. T. Ferguson, *J. Appl. Phys.* **84**, 6268 (1998).

[126] R. H. Brown and R. Q. Twiss, *Nature*, **177**, 27 (1956).

[127] R. Loudon, *The Quantum Theory of Light*, Oxford University Press, Oxford (2000).

[128] B. Lienhard, T. Schröder, S. Mouradian, F. Dolde, T. T. Tran, I. Aharonovich, and D. Englund, *Optica*, **3**, 768 (2016).

[129] S. C. Kitson, P. Jonsson, J. G. Rarity, and P. R. Tapster, *Phys. Rev. A*, **58**, 620 (1998).

[130] Y. Hijikata, S. Komori, S. Otojima, Y.-I. Matsushita, and T. Ohshima, *Appl. Phys. Lett.* **118**, 204005 (2021).

[131] T. Hosoi, Y. Katsu, K. Moges, D. Nagai, M. Sometani, H. Tsuji, T. Shimura, and H. Watanabe, *Appl. Phys. Express*, **11**, 091301 (2018).

[132] H. Watanabe, T. Hosoi, T. Kirino, Y. Kagei, Y. Uenishi, A. Chanthaphan, A. Yoshigoe, Y. Teraoka, and T. Shimura, *Appl. Phys. Lett.* **99**, 021907 (2011).

[133] F. Devynck, A. Alkauskas, P. Broqvist, and A. Pasquarello, *Phys. Rev. B*, **84**, 235320 (2011).

[134] T. Hosoi, M. Ohsako, T. Shimura, and H. Watanabe, *Appl. Phys. Express*, **14**, 101001 (2021).

[135] K. Tahara, *J. Open Source Softw.* **8**, 5938 (2023).

[136] K. Chokawa, M. Araidai, and K. Shiraishi, *J. Appl. Phys.* **124**, 135701 (2018).

[137] K. Tahara, *J. Open Source Softw.* **8**, 5938 (2023).

[138] J. G. Worboys, D. W. Drumm, and A. D. Greentree, *Phys. Rev. A*, **101**, 013810 (2020).

[139] Y.-I. Matsushita and A. Oshiyama, *arXiv*, 1612.00189 (2016).

[140] T. Kobayashi, K. Tachiki, K. Ito, and T. Kimoto, *Appl. Phys. Express*, **12**, 031001 (2019).

[141] T. Hosoi, D. Nagai, M. Sometani, Y. Katsu, H. Takeda, T. Shimura, M. Takei, and H. Watanabe, *Appl. Phys. Lett.* **109**, 182114 (2016).

[142] T. Akiyama, A. Ito, K. Nakamura, T. Ito, H. Kageshima, M. Uematsu, and K. Shiraishi, *Surf. Sci.* **641**, 174 (2015).

[143] T. Kobayashi, K. Harada, Y. Kumagai, F. Oba, and Y.-I. Matsushita, *J. Appl. Phys.* **125**, 125701 (2019).

[144] K. Onishi, T. Nakanuma, H. Toyama, K. Tahara, K. Kutsuki, H. Watanabe, and T. Kobayashi, *APL Mater.* **13**, 021119 (2025).

Acknowledgements

I would like to sincerely thank all those who supported and encouraged me throughout my Ph.D. studies. First of all, I would like to express my deepest appreciation to Associate Professor Takuma Kobayashi for his continuous support and thoughtful guidance based on his considerate encouragement. I am also deeply grateful to Professor Heiji Watanabe for his invaluable advice and constant encouragement. I am also sincerely grateful to Assistant Professor Masahiro Hara for his valuable advice, kind support, and encouragement throughout my Ph.D. research.

I am deeply indebted to Professor Yuji Kuwahara and Professor Hiromasa Ohmi for their insightful evaluations and thoughtful suggestions, which greatly contributed to improving the overall quality of this thesis.

I owe a significant debt to Professor Takayoshi Shimura at Waseda University and Dr. Takuji Hosoi at the National Institute for Materials Science (NIMS) for their invaluable advice during and after my time at The University of Osaka. I would like to express my deep appreciation to Dr. Katsuhiro Kutsuki, Dr. Kosuke Tahara, Dr. Haruko Toyama, and Dr. Taishi Kimura at Toyota Central Research & Development, who have been my joint research collaborators.

I am sincerely grateful to Professor Heiko B. Weber, Dr. Michael Krieger, and Dr. Johannes Lehmeyer at Friedrich-Alexander-Universität Erlangen-Nürnberg (FAU), who offered me the opportunity to conduct research there. Special thanks are also extended to all members of the Chair of Applied Physics at FAU for their kind support and cooperation.

I am also thankful to Mr. Hiroki Fujimoto and Mr. Kazuki Tomigahara for their warm encouragement as fellow Ph.D. students.

I am grateful to the Quantum team members—Mr. Kentaro Onishi, Mr. Sosuke Iwamoto, Mr. Yu Kaneko, and Mr. Ryota Yamada—for their encouragement and constructive discussions.

I would like to extend my gratitude to the administrative staff, Ms. Chika Usuda and Ms. Yuka Sawama, and to the specialist technical staff, Mr. Mikito Nozaki, for their dedicated assistance.

This work was partly supported by the Japan Society for the Promotion of Science (JSPS) through the Grant-in-Aid for JSPS Research Fellows (KAKENHI Grant Number 23KJ1501).

Finally, I would like to express my heartfelt thanks to my mother, uncle, and partner for their constant understanding and selfless love.

January, 2026

Takato Nakanuma

List of Publications

A-I. Original Papers (Peer Reviewed) about SPEs

1. T. Nakanuma, K. Tahara, K. Kutsuki, T. Shimura, H. Watanabe, and T. Kobayashi, "Control on the density and optical properties of color centers at SiO_2/SiC interfaces by oxidation and annealing",
   Applied Physics Letters **123**, 102102 (2023).

2. K. Onishi, T. Nakanuma, K. Tahara, K. Kutsuki, T. Shimura, H. Watanabe, and T. Kobayashi,
   "Generation of well-isolated single-photon emitters at a SiO_2/SiC interface by high-temperature oxidation and reoxidation at lower temperatures",
   Applied Physics Express **17**, 051004 (2024).

3. K. Onishi, T. Nakanuma, H. Toyama, K. Tahara, K. Kutsuki, H. Watanabe, and T. Kobayashi,
   "Insight into the energy level structure and luminescence process of color centers at SiO_2/SiC interfaces",
   APL Materials **13**, 021119 (2024).

4. T. Nakanuma, H. Toyama, K. Tahara, K. Kutsuki, H. Watanabe, and T. Kobayashi, "Design of annealing conditions for the generation of isolated single-photon emitters at SiO_2/SiC interfaces",
   Journal of Applied Physics **137**, 205702 (2025).

A-II. Original Papers (Peer Reviewed) about SiC MOS

1. T. Nakanuma, Y. Iwakata, A. Watanabe, T. Hosoi, T. Kobayashi, M. Sometani, M. Okamoto, A. Yoshigoe, T. Shimura, and H. Watanabe,
"Comprehensive physical and electrical characterizations of NO nitrided SiO_2/4H-SiC(11$\bar{2}$0) interfaces",
Japanese Journal of Applied Physics **61**, SC10651 (2022).

2. T. Nakanuma, T. Kobayashi, T. Hosoi, M. Sometani, M. Okamoto, A. Yoshigoe, T. Shimura, and H. Watanabe,
"Impact of nitridation on the reliability of 4H-SiC(11$\bar{2}$0) MOS devices",
Applied Physics Express **15**, 0410021 (2022).

3. T. Kobayashi, A. Suzuki, T. Nakanuma, M. Sometani, M. Okamoto, A. Yoshigoe, T. Shimura, and H. Watanabe,
"Characterization of nitrided SiC(1$\bar{1}$00) MOS structures by means of electrical measurements and X-ray photoelectron spectroscopy",
Materials Science in Semiconductor Processing **175**, 108251 (2024).

4. H. Watanabe, T. Kobayashi, H. Iwamoto, T. Nakanuma, H. Hirai, and M. Sometani,
"Comprehensive research on nitrided SiO_2/SiC interfaces by high-temperature nitric oxide annealing formed on basal and non-basal planes",
Japanese Journal of Applied Physics **64**, 010801 (2025).

B-I. International Conferences about SPEs

1. T. Nakanuma, T. Kobayashi, K. Tahara, T. Kimura, K. Kutsuki, T. Shimura, and H. Watanabe,
"Impact of Oxidation and Post Annealing on the Density and Optical Properties of Color Centers at SiO_2/SiC Interfaces",
19th International Conference on Silicon Carbide and Related Materials (ICSCRM 2022), We-2-A.4, Davos, Switzerland, Oral, September 2022.

2. T. Nakanuma, K. Tahara, K. Kutsuki, T. Shimura, H. Watanabe, and T. Kobayashi,
"Controlling the properties of single-photon emitters at SiO_2/SiC interfaces by oxidation and annealing",

International Conference on Silicon Carbide and Related Materials (ICSCRM 2023), Tu.15B.3, Sorrento, Italy, Oral, September 2023.

3. K. Onishi, T. Nakanuma, K. Tahara, K. Kutsuki, T. Shimura, H. Watanabe, and T. Kobayashi,
"Formation of color centers at SiO_2/SiC interfaces by thermal oxidation and its correlation with electrical properties",
International Conference on Silicon Carbide and Related Materials (ICSCRM 2023), Th.D.7, Sorrento, Italy, Poster, September 2023.

4. T. Nakanuma, K. Tahara, H. Toyama, K. Kutsuki, T. Shimura, H. Watanabe, and T. Kobayashi,
"Control over the density of single-photon emitters at SiO_2/SiC interfaces: CO_2 vs. Ar annealing",
International Conference on Silicon Carbide and Related Materials (ICSCRM 2024), Th.16A.1, Raleigh, USA, Oral, September 2024.

5. K. Onishi, T. Nakanuma, K. Tahara, H. Toyama, K. Kutsuki, T. Shimura, H. Watanabe, and T. Kobayashi,
"Suppression of luminescent spots at SiO_2/SiC interfaces by thermal oxidation at low oxygen partial pressure",
International Conference on Silicon Carbide and Related Materials (ICSCRM 2024), We.39, Raleigh, USA, Poster, September 2024.

6. Y. Kaneko, T. Nakanuma, H. Toyama, K. Tahara, K. Kutsuki, H. Watanabe, and T. Kobayashi,
"Impact of oxidation temperature on the formation and annihilation of color centers at SiO_2/SiC interfaces",
International Conference on Silicon Carbide and Related Materials (ICSCRM 2025), TU_P87, Busan, Korea, Poster, September 2025.

7. K. Onishi, T. Nakanuma, H. Toyama, K. Tahara, K. Kutsuki, T. Shimura, H. Watanabe, and T. Kobayashi,
"Characterization of color centers at SiO_2/SiC interfaces: Energy level identification and discussion of their origins",

International Conference on Silicon Carbide and Related Materials (ICSCRM 2025), WE_P88, Busan, Korea, Poster, September 2025.

B-II. International Conferences about SiC MOS

1. T. Nakanuma, Y. Iwakata, T. Hosoi, T. Kobayashi, M. Sometani, M. Okamoto, T. Shimura, and H. Watanabe,
"Comprehensive Physical and Electrical Characterizations of NO Nitrided SiO_2/4H-SiC(11$\bar{2}$0) Interfaces",
International Conference on Solid State Devices and Materials (SSDM 2021), D-4-03, online, September 2021.

2. T. Nakanuma, A. Suzuki, Y. Iwakata, T. Kobayashi, M. Sometani, M. Okamoto, T. Hosoi, T. Shimura, and H. Watanabe,
"Investigation of Reliability of NO Nitrided SiC(1$\bar{1}$00) MOS Devices",
IEEE International Reliability Physics Symposium (IRPS), 3B.2, online, Oral, March 2022.

3. T. Kobayashi, T. Nakanuma, A. Suzuki, M. Sometani, M. Okamoto, A. Yoshigoe, T. Shimura, and H. Watanabe,
"Reliability Issues in Nitrided SiC MOS Devices",
9th International Symposium on Control of Semiconductor Interfaces (ISCSI-IX), WA2-1, Nagoya, Japan, Oral, September 2022.
[Invited talk]

4. T. Kobayashi, T. Nakanuma, A. Suzuki, M. Sometani, M. Okamoto, A. Yoshigoe, T. Shimura, and H. Watanabe,
"Nitridation-induced degradation of SiC (1$\bar{1}$00) MOS devices",
19th International Conference on Silicon Carbide and Related Materials (ICSCRM 2022), Tu-2-A.4, Davos, Switzerland, Oral, September 2022.

5. A. Suzuki, T. Nakanuma, T. Kobayashi, M. Sometani, M. Okamoto, A. Yoshigoe, T. Shimura, and H. Watanabe,
"Analysis of leakage current mechanisms in NO-nitrided SiC(1$\bar{1}$00) MOS devices",
International Conference on Solid State Devices and Materials (SSDM 2022), J-6-05, Chiba, Japan, Oral, September 2022.

6. H. Iwamoto, T. Nakanuma, H. Hirai, M. Sometani, M. Okamoto, T. Kobayashi, T. Shimura, and H. Watanabe,
   "Characterizations of nitrogen profiles and interface properties in NO-nitrided $SiO_2/SiC(0\bar{3}3\bar{8})$ structures",
   International Workshop on Dielectric Thin Films for Future Electron Devices, S6-4, Kanazawa, Japan, Oral, October 2023.